

## ABSTRACT

JUNG WON CHO, Pulsed DC Reactive Magnetron Sputtering of Aluminum Nitride Thin Films (Under the direction of Dr. J. J. Cuomo)

Aluminum nitride thin films have been deposited by pulsed DC reactive magnetron sputtering. The pulsed DC power provides arc-free deposition of insulating films. Two types of pulsed DC (unipolar and asymmetric bipolar) were studied with respect to characteristics and properties of resultant films. The unipolar power supply generates a series of 75 kHz DC pulses modulated with 2.5 kHz frequency. The frequency of asymmetric power supply can be varied from 50 kHz to 250 kHz. The duty cycle, which is a ratio of negative pulse time to total time, can be varied from 60% to 98%. Very fast oscillation and overshoot were observed when the polarity of the target voltage was changed.

The control of crystal orientation of deposited film is important since the properties of AlN film is related with the orientation. For example, the acoustic velocity is high along the c-axis. The electromechanical coupling coefficient is large in a-axis direction. The crystal orientation and microstructure of the AlN films were strongly affected by the deposition conditions such as sputtering power, growth temperature, sputtering gas pressure and frequency/duty cycle. The crystal orientation of AlN films was closely related with the energy of sputtered atoms and mobility of adatoms on substrate. The c-axis oriented films were obtained when the target power and growth temperature were high. This provided higher energy of sputtered atoms and mobility of adatoms. The deposited AlN films have a columnar structure.

The crystal orientation of the AlN films was changed from (101) to (002) by applying an RF bias was applied to the substrate in unipolar pulsed DC sputtering. The columnar structure disappeared when the RF bias was applied to the substrate. Applying bias was thought to increase mobility of adatoms by ion bombardment.

MIM (aluminum-AlN-aluminum or molybdenum) structure was fabricated to measure electric properties of AlN films. Dielectric constants of 8.5 to 11.5 were obtained at 100 kHz. The relation of the current density and electric field of the AlN film

followed ohmic conduction. The broad photoluminescence spectrum in the range of 300 nm and 650 nm was observed for the aluminum nitride thin films regardless of the deposition conditions. This spectrum might be due to the defects related with oxygen. The thermal conductivity of AlN films was evaluated by the  $3\omega$  method. The values in the range of 12 and 30 W/mK was obtained. Those values are very low compared to those of bulk. The reason might be attributed to the oxygen incorporation as well as the unique microstructure of the sputtered films.

The plasma parameters such as electron temperature and charge density were obtained by the Langmuir probe. The electron temperature in argon and nitrogen plasma increased from 2.7 to 5.3 eV when the frequency increased from 75 kHz to 250 kHz in asymmetric bipolar pulsed DC sputtering. The electron and ion densities were found to increase with frequency. The stochastic heating due to the fast oscillation in the target voltage waveform may be attributed to the increased electron temperature and electron/ion densities. The measured plasma characteristics were correlated with properties of the AlN film. The ion and energy flux were believed to increase as the frequency increased. The intensity of the (002) peaks was found to increase with the increase in the ion flux and energy flux.

**PULSED DC REACTIVE MAGNETRON SPUTTERING OF ALUMINUM  
NITRIDE THIN FILMS**

**by  
JUNG WON CHO**

A dissertation submitted to the Graduate Faculty of  
North Carolina State University  
in partial fulfillment of the  
requirements for the  
Degree of Doctor of Philosophy

**DEPARTMENT OF MATERIALS SCIENCE AND ENGINEERING**

Raleigh  
2002

**APPROVED BY:**



Chair of Advisory Committee      Minor Representative

## BIOGRAPHY

JUNG WON CHO (LEE) was born on April 9, 1970 in Seoul, Korea. She received her B.S. degree from the Department of Ceramic Engineering of Yonsei University, Seoul, Korea in 1992 and M.S. degree with a dissertation concerning the photo-electrochemical effects of tungsten oxide thin films from the same university in 1995. After her marriage with Yong Soo in 1994, she spent two years (1997-1999) at New York State College of Ceramics at Alfred University, New York, as a Ph.D candidate with a research project regarding the chemical processing and magnetic properties of ferrite materials. She transferred to the Department of Materials Science and Engineering of North Carolina State University in 1999 as a result of her husband's job transfer to North Carolina. Since then, her research project was related to the aluminum nitride thin films deposited by novel sputtering techniques. She has been an active member of American Ceramic Society and Materials Research Society. She is the author of several scientific and technical papers, which dealing with electronic and magnetic materials and related applications. She is a mother of two wonderful boys, Albert and Bryan, who were born in 1996 and 2000, respectively.

## ACKNOWLEDGEMENTS

I would like to sincerely thank my advisor Dr. Jerome J. Cuomo for his great guidance and encouragement during my Ph.D work. I have special thanks to other faculties in my thesis committee, Dr. M. Bourham who guided me with valuable discussion on plasma physics, Dr. D. Maher for his support and guidance in my TEM study, and Dr. Narayan who helped me with his enormous experience.

I would like to express my appreciation to Drs. J. Pierce, R. Keusseyan and Yong S. Cho at DuPont especially for their financial support on the project of the LTCC-thin film work. I can not miss Sandra Kessler and Dr. Bo Wang at PPG for their support and interest in related glass fiber project. I really like to thank all the people at CAMP-M, Dr. Minseo Park, Dr. Roger Sanwald, Pete Yancey, Dave McGreger, Scott Dillon and Brent Thomas for their help and support. Without them, my lab life would be very dry. My special thanks go to my friends who helped me for various measurements and characterization, including Jeff Chang, Taeyun Kim, Brian Rodriguez, Brian Lee Bures, Sharon Kiesel, Baxter Moody and Terry Stark at MAS. I will not forget people who help me to establish my fundamental experience and knowledge on materials science, such as Prof. Ki Hyun Yoon at Yonsei University, Korea and Dr. Vasantha, R. W. Amarakoon at Alfred University, New York.

I would like to express my very sincere thanks to my family, husband Yong Soo and two sons, Albert and Bryan as well as my parents and relatives in Korea.

## TABLE OF CONTENTS

<b>LIST OF TABLES</b> .....	viii
<b>LIST OF FIGURES</b> .....	xi
<b>1. Introduction</b> .....	1
1.1. Aluminium nitride: crystal structure, properties, applications.....	2
1.1.1. Crystal structure of aluminum nitride.....	2
1.1.2. Properties of aluminum nitride.....	3
1.1.3. Applications of aluminum nitride.....	5
1.2. Pulsed DC reactive magnetron sputtering.....	5
1.2.1. Sputtering.....	5
1.2.2. Magnetron sputtering.....	6
1.2.3. Reactive sputtering.....	9
1.2.4. Pulsed DC sputtering.....	10
1.2.5. Types of pulsed DC power.....	13
1.2.5. Structure zone model.....	15
1.3. Plasma physics.....	18
1.3.1. Plasma oscillation.....	19
1.3.2. Effects of electric fields and magnetic fields.....	20
1.3.3. Potentials in glow discharge.....	27
1.4. Thermal conduction mechanism.....	28
1.4.1. Thermal conductivity and thermal diffusivity.....	29
1.4.2. Thermal conduction processes.....	31
1.4.2.1. Phonon conductivity.....	31
1.4.2.2. High thermal conductivity materials.....	35
<b>2. Experimental Procedure</b> .....	37
2.1. Sputtering set up.....	37
2.2. Sputtering experimental parameters and condition.....	37

2.3. Characterization of plasma and thin films.....	40
2.3.1. Target voltage waveform.....	40
2.3.2. Film thickness.....	41
2.3.3. X-ray phase analysis.....	43
2.3.4. Microstructural analysis - SEM, AFM and TEM.....	43
2.3.5. Electrical properties.....	44
2.3.6. Stress analysis by x-ray patterns.....	44
2.3.7. Photoluminescence spectrum.....	44
2.3.8. Thermal conductivity.....	45
2.3.9. Langmuir probe measurement.....	45
<b>3. Bipolar Asymmetric Pulsed DC Sputtering of AlN Thin Films .....</b>	<b>48</b>
3.1. Wave Form of Pulsed DC Power.....	48
3.2. Dependence of sputtering parameters on crystal orientation and microstructures.....	52
3.2.1. Sputtering power.....	52
3.2.2. Growth temperature.....	58
3.2.3. Gas pressure.....	63
3.2.4. Nitrogen concentration.....	72
3.2.5. Negative pulse time.....	78
3.2.6. Pulsing frequency/Duty cycle .....	83
3.2.7. Discussion on preferential orientation.....	84
3.3. Electrical analysis.....	90
3.3.1. Dielectric characteristics of MIM capacitor.....	90
3.3.2. Current density-voltage measurement.....	92
3.4. Residual stress analysis.....	100
3.5. Photoluminescence .....	104
3.6. Thermal conductivity.....	106
<b>4. Unipolar Pulsed DC Sputtering of AlN Thin Films .....</b>	<b>111</b>

4.1. Wave Form of Pulsed DC Power.....	111
4.2. Dependence of sputtering parameters on crystal orientation and microstructures.....	111
4.2.1. Bias effect.....	111
4.2.2. Long deposition processing stability.....	115
4.2.3. Deposition on LTCC (low temperature co-fired ceramics) substrate .....	119
4.3. TEM study.....	126
4.4. Photoluminescence .....	132
4.5. Thermal conductivity.....	134
4.6.	
<b>5. AlN Thin Film Analysis via Plasma Diagnostics using Langmuir Probe ...</b>	<b>138</b>
5.1. Langmuir probe method.....	138
5.1.1. Probe construction.....	138
5.1.2. Assumptions.....	139
5.1.3. Double Probe.....	140
5.1.4. Single probe.....	143
5.1.5. Practical complications .....	147
5.2. Double probe measurement.....	147
5.3. Single probe measurement.....	154
5.3.1. Frequency effect on plasma properties.....	154
5.3.2. Negative voltage period effect on plasma parameters.....	158
5.3.3. Correlation with properties of AlN thin films.....	162
<b>6. Summary and Conclusions.....</b>	<b>167</b>
6.1. Asymmetric bipolar pulsed DC sputtering.....	167
6.2. Unipolar pulsed DC sputtering.....	169
6.3. Plasma diagnostics.....	170
<b>Future Work.....</b>	<b>172</b>

<b>Reference.....</b>	<b>173</b>
<b>Appendix 1. AlN Thin Films on Glass Fiber.....</b>	<b>189</b>
<b>Appendix 2. Zirconia Thin Films Prepared by Pulsed DC Reactive Magnetron Sputtering.....</b>	<b>205</b>

## LIST OF TABLES

Table 1-1. Physical properties of wurtzite aluminum nitride.....	5
Table 1-2. Thermal conductivity at room temperature for several adamantine crystals .....	36
Table 2-1. Frequency and duty cycle of bipolar asymmetric pulsed DC power supply .....	39
Table 2-2. Experimental conditions for unipolar pulsed DC sputtering.....	42
Table 2-3. Experimental conditions for bipolar pulsed DC sputtering.....	42
Table 3-1. Dielectric properties of the aluminum nitride films on Al and Mo at 100 kHz (Deposition condition: temperature 500°C, sputtering gas pressure 28 mT, 70% N <sub>2</sub> , target current 2A. The number in parenthesis is standard deviation).....	94
Table 3-2. Summary of the curve fitting results of lnJ vs. lnE.....	99
Table 3-3. Diffraction planes and related parameters. (Cu K $\alpha$ = 1.540598Å).....	101
Table 3-4. Residual stress of the aluminum nitride films on Si at different sputtering pressure (250 kHz, 60% duty cycle).....	103
Table 3-5. Residual stress of the aluminum nitride thin films on Si with duty cycle change at 75 kHz frequency.....	103
Table 3-6. Photoluminescence of the aluminum nitride thin films on Si (100).....	104

Table 3-7. Thermal conductivity of the aluminum nitride films on Si (100) and Mo measured by $3\omega$ method.....	109
Table 4-1. Typical properties of fired 951 LTCC tape.....	120
Table 4-2. Deposition rates of the sputtered aluminum nitride films.....	126
Table 4-3 Photoluminescence of the aluminum nitride thin films on Si (100) grown at different growth temperatures (sputtering pressure 5 mT, 60% N <sub>2</sub> , target current 3A).....	132
Table 4-4. Thermal conductivity of the aluminum nitride thin films.....	136
Table 4-5. Thermal diffusivity and thermal conductivity values of tape 951 and aluminum nitride on tape 951.....	137
Table 5-1. Some properties of important probe materials.....	139
Table 5-2. Double probe measurement results.....	151
Table 5-3. Results of ohmic heating.....	153
Table 5-4. Results of the Langmuir probe measurement with a variation of a pulsing frequency at constant duty cycle 80%.....	157
Table 5-5 Summary of single probe measurement results with a variation of a negative pulse time, $\tau_{on}$ at constant reverse pulse time, $\tau_{rev}=496\text{nsec}$ .....	161

Table 5-6. Flux to the substrate at various frequencies.....164

Table 5-7. Flux to the substrate with negative pulse time change.....166

## LIST OF FIGURES

<i>Figure 1-1.</i> Wurtzite structure of the aluminum nitride.....	3
<i>Figure 1-2.</i> Temperature dependence of thermal conductivity of aluminum nitride.....	4
<i>Figure 1-3.</i> (a) Circular planar magnetron, (b) rectangular planar magnetron, (c) cylindrical posy magnetron and (d) conical magnetron.....	8
<i>Figure 1-4.</i> Schematic of the target surface during reactive DC sputtering of an insulating material. The dielectric layer is charged by positive ions causing a voltage build up, $V_D$ , across the insulating layer with thickness $d$ .....	12
<i>Figure 1-5.</i> Three types of pulsed DC power wave form (a) unipolar, (b) symmetric bipolar and (c) asymmetric bipolar.....	14
<i>Figure 1-6.</i> Characteristics of the four basic structural zones. The ratio of substrate $T_s$ to film melting ( $T_s/T_m$ ) increases in the direction $Z1 \rightarrow ZT \rightarrow Z2 \rightarrow Z3$ .....	16
<i>Figure 1-7.</i> Basic structure zone with various thickness.....	18
<i>Figure 1-8.</i> Orbits of ions and electrons in a homogeneous static magnetic field $B$ . A particle follows a helical orbit, with a gyro frequency $\omega$ that is independent of the particle energy.....	22
<i>Figure 1-9.</i> Particle drifts in crossed electric and magnetic field.....	23

<i>Figure 1-10.</i> The drift of a gyrating particle in a nonuniform magnetic field.....	24
<i>Figure 1-11.</i> A curved magnetic field.....	25
<i>Figure 1-12.</i> The polarization drift.....	27
<i>Figure 2-1.</i> Schematic of magnetron sputtering system.....	38
<i>Figure 2-2.</i> Magnetic field at the target and substrate position.....	40
<i>Figure 2-3.</i> Target voltage measurement set-up.....	41
<i>Figure 2-4.</i> Pattern for the heater/thermometer line and contact pads. The width of the heater/thermometer line $w$ is typically 8 $\mu\text{m}$ and the length $l$ is 1.0 mm.....	45
<i>Figure 2-5.</i> Double probe head (a) side view and (b) cross section view.....	46
<i>Figure 2-6.</i> Langmuir probe measurement set-up (a) double probe and (b) single probe.....	47
<i>Figure 3-1.</i> Target voltage waveforms at 75 kHz with (a) 60%, (b) 80% and (c) 96% of duty cycle (28 mT of sputtering pressure, 70% of $\text{N}_2$ , 2 A of target current).....	49
<i>Figure 3-2.</i> Target voltage waveforms at 100 kHz with of (a) 60%, (b) 80% and (c) 95% of duty cycle (28 mT of sputtering pressure, 70% of $\text{N}_2$ , 2 A of target current).....	50

- Figure 3-3.* Target voltage waveforms at 250 kHz with (a) 60%, (b) 80% and (c) 88% of duty cycle (28 mT of sputtering pressure, 70% of N<sub>2</sub>, 2 A of target current).....51
- Figure 3-4.* XRD results of the aluminum nitride thin films on Si (100) prepared at (a) 1.0 A, (b) 1.25 A, (c) 1.5 A, (d) 2.0 A and (e) 2.5 A of target current (500°C of growth temperature, 28 mT of sputtering pressure, 70% of nitrogen, 100 kHz of frequency, 80% of duty cycle).....53,54
- Figure 3-5.* Deposition rates of the aluminum nitride thin films on Si (100) with target current variations (500°C of growth temperature, 28 mT of sputtering pressure, 70% of nitrogen, 100 kHz of frequency, 80% of duty cycle).....56
- Figure 3-6.* Cross section views of the aluminum nitride thin films on Si (100) grown at (a) 1.0A, (b) 1.25A, (c) 1.5A, (d) 2.0A and (e) 2.5A of target current (500°C of growth temperature, 28 mT of sputtering pressure, 70% of nitrogen, 100 kHz of frequency, 80% of duty cycle).....57
- Figure 3-7.* AFM images of the aluminum nitride thin films on Si (100) grown at (a) 1.0 A, (b) 1.5 A, (c) 2.0 A and (d) 2.5 A of target current (500°C of growth temperature, 28 mT of sputtering pressure, 70% of nitrogen, 100 kHz of frequency, 80% of duty cycle). Scan area is 5 μm × 5 μm.....59
- Figure 3-8.* Rms surface roughness of the AlN films grown on Si (100) with variations of target currents (500°C of growth temperature, 28 mT of sputtering pressure, 70% of nitrogen, 100 kHz of frequency, 80% of duty cycle).....60

- Figure 3-9.* XRD results of the aluminum nitride thin films on Si (100) grown at (a) 300°C, (b) 500°C and (c) 700°C (28 mT of sputtering pressure, 70% of nitrogen, 2 A of target current, 100 kHz of frequency, 80% of duty cycle).....61
- Figure 3-10.* Deposition rates of the aluminum nitride thin films on Si (100) with growth temperature change (28 mT of sputtering pressure, 70% of nitrogen, 2 A of target current, 100 kHz of frequency, 80% of duty cycle).....62
- Figure 3-11.* Cross section views and surface morphologies of the aluminum nitride thin films on Si (100) grown at (a) and (b) 300°C, (c) and (d) 500°C, (e) and (f) 700°C (28 mT of sputtering pressure, 70% of nitrogen, 2 A of target current, 100 kHz of frequency, 80% of duty cycle).....64
- Figure 3-12.* Rms surface roughness of the aluminum nitride thin films on Si (100) with growth temperature change (28 mT of sputtering pressure, 70% of nitrogen, 2 A of target current, 100 kHz of frequency, 80% of duty cycle).....65
- Figure 3-13.* XRD results of the aluminum nitride thin films on Si (100) prepared with (a) 5 mT, (b) 10 mT, (c) 28 mT of sputtering pressures at 100 kHz of frequency and 80% of duty cycle (500°C of growth temperature, 2 A of target current, 70% of nitrogen).....66
- Figure 3-14.* XRD results of the aluminum nitride thin films on Si (100) prepared with (a) 5 mT, (b) 10 mT, (c) 28 mT of sputtering pressures at 250 kHz of frequency and 60% of duty cycle (500°C of growth temperature, 2 A of target current, 70% of nitrogen).....68

- Figure 3-15.* Deposition rates of the aluminum nitride thin films on Si(100) with change in sputtering pressure (500°C of growth temperature, 2 A of target current, 70% of nitrogen).....69
- Figure 3-16.* Surface morphologies and cross section of the aluminum nitride thin films grown with (a) and (b) 5 mT, (c) and (d) 10 mT, (e) and (f) 28 mT of sputtering pressure at 100 kHz and 80% of duty cycle (500°C of growth temperature, 2 A of target current, 70% of nitrogen).....70
- Figure 3-17.* Surface morphologies and cross section of the aluminum nitride thin films grown with (a) and (b) 5 mT, (c) and (d) 10 mT, (e) and (f) 28 mT of sputtering pressure at 250 kHz and 60% of duty cycle (500°C of growth temperature, 2 A of target current, 70% of nitrogen).....71
- Figure 3-18.* Surface roughness (rms) of the AlN films grown on Si (100) with variations of sputtering gas pressure (500°C of growth temperature, 70% of N<sub>2</sub>, 2 A of target current).....73
- Figure 3-19.* XRD results of the aluminum nitride thin films on Si (100) prepared by (a) 50%, (b) 70% and (c) 90% of N<sub>2</sub> (500°C of growth temperature, 2 A of target current, 10 mT sputtering pressure, 100 kHz of frequency, 80% of duty cycle).....74
- Figure 3-20.* Deposition rates of the aluminum nitride thin films on Si (100) with N<sub>2</sub> contents (500°C of growth temperature, 2 A of target current, 10 mT sputtering pressure, 100 kHz of frequency, 80% of duty cycle).....75
- Figure 3-21.* Cross section views and surface morphologies of the aluminum nitride films on Si (100) grown with (a) and (b) 50%, (c) and (d) 70%, (e) and (f) 90% of N<sub>2</sub> at 10 mT of sputtering pressure. (500°C of growth

- temperature, 2 A of target current, 100 kHz of frequency, 80% of duty cycle).....76
- Figure 3-22.* Surface roughness (rms) of the AlN films grown on Si (100) with variations of N<sub>2</sub> content (500°C of growth temperature, 2 A of target current, 100 kHz of frequency, 80% of duty cycle).....77
- Figure 3-23.* Target voltage vs. time at 496 nsec of constant reverse pulse time.....79
- Figure 3-24.* XRD results of the aluminum nitride thin films on Si (100) prepared at (a) 12.834 μsec, (b) 9.504 μsec and (c) 3.504 μsec of negative pulsed time (500°C of growth temperature, 28 mT of sputtering pressure, 70% of N<sub>2</sub>, 2 A of target current, 496 nsec of reverse pulse time).....80
- Figure 3-25.* Deposition rates of the aluminum nitride thin films on Si(100) with negative period variations (500°C of growth temperature, 28 mT of sputtering pressure, 70% of N<sub>2</sub>, 2 A of target current, 496 nsec of reverse pulse time).....81
- Figure 3-26.* Cross sections and surface morphologies of the aluminum nitride thin films on Si (100) prepared with (a), (b) 12.834 μsec, (c), (d) 9.504 μsec and (e), (f) 3.504 μsec of negative pulse time (500°C of growth temperature, 28 mT of sputtering pressure, 70% of N<sub>2</sub>, 2 A of target current, 496 nsec of reverse pulse time).....82
- Figure 3-27.* Surface roughness (rms) of the AlN films grown on Si (100) with variations of negative pulsed time. (500°C of growth temperature, 28 mT of sputtering pressure, 70% of N<sub>2</sub>, 2 A of target current, 496 nsec of reverse pulse time).....83

- Figure 3-28.* XRD results of the aluminum nitride thin films grown at (a) 60%, (b) 80% and (c) 96% of duty cycle at 75 kHz (500°C of growth temperature, 28 mT of sputtering pressure, 70% of N<sub>2</sub>, 2 A of target current).....85
- Figure 3-29.* XRD results of the aluminum nitride thin films grown at (a) 60%, (b) 80% and (c) 95% of duty cycle at 100 kHz (500°C of growth temperature, 28 mT of sputtering pressure, 70% of N<sub>2</sub>, 2 A of target current).....86
- Figure 3-30.* XRD results of the aluminum nitride thin films grown at (a) 60%, (b) 80% and (c) 88% of duty cycle at 250 kHz (500°C of growth temperature, 28 mT of sputtering pressure, 70% of N<sub>2</sub>, 2 A of target current).....87
- Figure 3-31.* XRD results of the aluminum nitride films on Si (100) as a function of frequency and duty cycle (500°C of growth temperature, 28 mT of sputtering pressure, 70% of N<sub>2</sub>, 2 A of target current).....88
- Figure 3-32.* Deposition rates of the aluminum nitride thin films on Si (100) versus negative pulse time (500°C of growth temperature, 28 mT of sputtering pressure, 70% of N<sub>2</sub>, 2 A of target current).....88
- Figure 3-33.* Geometry of the crystallographic planes for (002), (102) and (101) in the hexagonal AlN lattices.....89
- Figure 3.34.* Capacitance versus voltage of the aluminum nitride films grown on (a) Al bottom electrode (100 kHz, 80% duty cycle) and (b) molybdenum

bottom electrode (250 kHz, 80% duty cycle) with different top electrode areas. The measurement was performed at 100 kHz.....92

*Figure 3-35.* Capacitance versus electrode area of the aluminum nitride thin films measured at 100 kHz (Deposition condition; 28 mT of sputtering pressure, 70% of N<sub>2</sub>, 2 A of target current, 80% of duty cycle).....93

*Figure 3-36.* Current density-electric field curve of the aluminum nitride thin films on molybdenum bottom electrode grown at different frequencies (Deposition condition: 500°C of growth temperature, 28 mT of sputtering pressure, 70% of N<sub>2</sub>, 2 A of target current).....97

*Figure 3-37.* lnJ vs. ln E curves of the aluminum nitride thin films (500°C of growth temperature, 28 mT of sputtering pressure, 70% of N<sub>2</sub>, 2 A of target current, 80% of duty cycle).....98

*Figure 3-38.* Plot of  $\sin^2 \psi$  and lattice strain obtained from XRD pattern of the AlN films grown at (a) 100 kHz/80% duty cycle and (b) 250 kHz/60% duty cycle (500°C of growth temperature, 70% of N<sub>2</sub>, 2 A of target current).....102

*Figure 3-39.* Photoluminescence spectrums of the aluminum nitride (a) 75 kHz/60% duty cycle and (b) 100 kHz/80% duty cycle (500°C of growth temperature, 28 mT of sputtering pressure, 70% of N<sub>2</sub>, 2 A of target current).....105

*Figure 3-40.* Measured amplitude of the temperature oscillation,  $\Delta T$  as a function of frequency of the AlN film grown on Si and Mo (500°C of growth

- temperature, 75 kHz of frequency, 60% of duty cycle, 28 mT of sputtering pressure, 70% of N<sub>2</sub>, 2 A of target current).....108
- Figure 4-1.* (a) Measured unipolar waveform [128] and (b) illustration for the measured waveform.....112
- Figure 4-2.* XRD results of the aluminum nitride thin films on Si (100) prepared with (a) without substrate bias and (b) with RF 100 W bias (growth temperature, 950°C, sputtering pressure 50 mT, 60% nitrogen, target current 2 A).....113
- Figure 4-3.* (002) peak of AlN film. The dotted line indicates the (002) peak position of 36.04° for an AlN powder sample. The red solid line is Gauss fitting.....114
- Figure 4-4.* Microstructures of the aluminum nitride thin films on Si (100) prepared (a) and (b) without bias, (c) and (d) with RF 25 W bias (950°C of growth temperature, 50 mT of sputtering pressure, 60% of nitrogen, 2 A of target current).....116
- Figure 4-5.* XRD of the aluminum nitride film on Si (100) (1100°C of growth temperature, 28 mT of sputtering pressure, 60% of N<sub>2</sub>, 25W of RF bias, 2 A of target current).....117
- Figure 4-6.* Microstructures of the aluminum nitride thin films on Si (100) (1100°C of growth temperature, 28 mT of sputtering pressure, 60% of N<sub>2</sub>, 25W of RF bias, 2.0 A of target current).....118
- Figure 4-7.* An example of aluminum nitride thin film used as a heat sink in multilayer LTCC structure.....120

- Figure 4-8.* Surface morphologies of the as-received (a) tape 951 and (b) tape 951 having screen-printed gold.....121
- Figure 4-9.* XRD results of the aluminum nitride thin films on tape 951 grown at 500°C (a) without bias and (b) 25 W RF bias to the substrate.....122
- Figure 4-10.* XRD results of the aluminum nitride thin films on tape 951 grown at 700°C (a) without bias and (b) 25 W RF bias to the substrate.....123
- Figure 4-11.* Surface morphologies of the (a) AlN films on tape 951, (b) AlN on tape 951 (high magnification) and (c) AlN on screen-printed gold (700°C of growth temperature, without bias, 5 mT of sputtering pressure, 60% of N<sub>2</sub>, 2 A of target current).....124
- Figure 4-12.* Cross-sections of the (a) and (b) AlN on tape 951, (c) and (d) AlN on screen-printed gold on tape 951 (500°C of growth temperature, 25 W of RF bias, 5 mT of sputtering pressure, 60% of N<sub>2</sub>, 2 A of target current).....125
- Figure 4-13.* Cross section view (a) interface, (b) middle and (c) top of the film on Tape 951.....128
- Figure 4-14.* TEM image of the interface at aluminum nitride and Tape 951.....129
- Figure 4-15.* (a) and (b) plane view of the aluminum nitride thin film on tape 951, (c) void at triple point and (d) SADP.....130

- Figure 4-16.* Grain size dependence of the aluminum nitride film on Tape 951 analyzed by TEM observation.....131
- Figure 4-17.* Photoluminescence spectrums of the AlN thin films grown at (a) 300°C (thickness=10.7  $\mu\text{m}$ ) and (b) 500°C (thickness=9.15  $\mu\text{m}$ ) (5 mT of sputtering pressure, 60% of N<sub>2</sub>, 3 A of target current).....132
- Figure 4-18.* Photoluminescence spectrum of the aluminum nitride thin film on Si (100) (700°C of growth temperature, 5 mT of sputtering pressure, 60% of N<sub>2</sub>, 25 W of RF substrate bias, 2 A of target current).....134
- Figure 4-19.* Measured amplitude of the temperature oscillation,  $\Delta T$ , of the heater/thermometer line as a function of the frequency: (a) 300°C of growth temperature, 5 mT of sputtering pressure, 60% of N<sub>2</sub>, 3 A of target current and (b) 500°C of growth temperature, 5 mT of sputtering pressure, 60% of N<sub>2</sub>, 3 A of target current.....135
- Figure 5-1.* Typical current-voltage characteristics of a double probe.....141
- Figure 5-2.* Typical current-voltage characteristics of a single probe.....144
- Figure 5-3.* Double probe measurement for 10mT Ar plasma.....149
- Figure 5-4.* Double probe measurement of the 28mT of Ar/N<sub>2</sub> plasma.....150
- Figure 5-5.* Single probe measurement with frequency changes at 80% duty cycle (28 mT of sputtering pressure, 70% of N<sub>2</sub>, 2 A of target current).....155

- Figure 5-6.* Plasma densities with frequency change at 80% duty cycle cycle (28 mT of sputtering pressure, 70% of N<sub>2</sub>, 2 A of target current).....156
- Figure 5-7.* Current-voltage curve of single probe with change in negative pulse time (28 mT of sputtering pressure, 70% of N<sub>2</sub>, 2A of target current, 0.496 μsec of reverse pulse time).....159
- Figure 5-8.* ln I versus voltage plot with changing negative pulse time.....160
- Figure 5-9.* Plasma density versus negative pulse time at 0.496 μsec of constant reverse pulse time.....162
- Figure 5-10.* Relative intensity of the (002), (101) and (102) lattice planes of the aluminum nitride thin films with frequency change.....165
- Figure 5-11.* Relative intensity of the (002), (101) and (102) lattice planes of the aluminum nitride thin films with negative pulse time.....166

## 1. INTRODUCTION

Aluminum nitride (AlN) has several promising properties in technical and scientific points of view, such as chemical stability, hardness, high thermal conductivity (320 W/mK), high electrical resistivity, a wide band gap (6.2 eV), a low thermal expansion coefficient (4 ppm/K) and high acoustic velocity (5.67 km/sec).

The useful thermal, mechanical and electronic properties make aluminum nitride an attractive choice in many electronic and optoelectronic applications including electronic packaging fields. Aluminum nitride is known non-toxic and exhibits good thermal expansion match with that of Si at moderate temperatures. And the dielectric constant of AlN is slightly smaller (8.8 at 1 MHz) than that of Al<sub>2</sub>O<sub>3</sub> and nearly independent of frequency [1].

Aluminum nitride thin films have been extensively studied by using the most of common deposition techniques including such as metalorganic chemical vapor deposition (MOCVD) [2,3], plasma-enhanced chemical vapor deposition (PECVD) [4,5], molecular beam epitaxy (MBE) [6], ion beam sputtering [7,8], pulsed laser ablation [9, 10], DC magnetron sputtering [11-13] and RF magnetron sputtering [14-18].

The CVD technique has been used most commonly for the growth of III-V compounds including aluminum nitride because of its excellent processing controllability and suitability for mass production. However, substrate temperature in conventional CVDs is very high (>1000°C) and a smooth surface morphology of AlN thin films cannot be obtained by this method due to its high grain growth rate [2]. Reactive magnetron sputtering may be a more desirable process for the deposition of dielectric materials due to its processing simplicity and scalability in the semiconductor industry. The advantages of reactive magnetron sputtering include inexpensive equipment, low temperature growth conditions and ease of deposition.

In this section, some base information regarding aluminum nitride and reactive magnetron sputtering will be given.

## 1.1. Aluminum nitride: Crystal structure, properties, applications

### 1.1.1. Crystal structure of aluminum nitride

Aluminum nitride has the wurtzite structure, 6-mm point group and  $P6_{3mc}$  space group. Reported lattice parameters range from 3.110 to 3.113 Å for the a lattice and from 4.978 to 4.982 Å for the c lattice. The c/a ratio thus varies between 1.600 and 1.602. The variation in c/a ratio, deviating from that of the ideal wurtzite crystal, is probably due to lattice instability and ionicity [19]. *Figure 1-1* shows the crystalline lattice structure of AlN. In this structure, each Al atom is surrounded by four N atoms, forming a distorted tetrahedron with three Al-N<sub>(i)</sub> (I=1,2,3) bonds named B<sub>1</sub> and one Al-N<sub>0</sub> bond in the direction of the c-axis, named B<sub>2</sub>. The stacking sequence of the (0001) plane is ABABAB in the <0001> direction as shown in *Figure 1-1*. The bond lengths of B<sub>1</sub> and B<sub>2</sub> are 0.1885 and 0.1917 nm, respectively. The bond angle for N<sub>0</sub>-Al-N<sub>1</sub> is 107.7° and that for N<sub>1</sub>-Al-N<sub>2</sub> is 110.5°. Similarly, a tetrahedron is formed with the N atoms as the corner. Two tetrahedrons form a triangular prism with the C<sub>3v</sub> symmetry. In the AlN cell, the atoms of Al and N form four sp<sup>3</sup>-hybridized orbitals. The Al atom has three semi-full orbitals and one empty orbital; the N atom has three semi-full orbitals and one full orbital. The bond B<sub>2</sub> is formed by the coupling of the Al empty orbital and the N full orbital. Consequently, the ionic character of the B<sub>2</sub> bond is greater. The bond energy of B<sub>2</sub> is relatively smaller than that of the three equivalent B<sub>1</sub> bonds and is easy to break, so that the energy required for sputtering particles to be deposited in the direction of the c-axis must be exceeded. The plane (100) is composed of the bond B<sub>1</sub>, while planes (002) and (101) consist of the bonds B<sub>1</sub> and B<sub>2</sub> together.

AlN is generally reported to be non-polymorphous. However, several reports suggested the occurrence of a metastable zincblende polytype of AlN, with a lattice parameter a=4.83 Å. A pressure induced rocksalt (space group O<sub>h</sub><sup>5</sup>) phase has been observed experimentally. The equilibrium transformation pressure was reported to be less than 14 GPa. The rocksalt structure has an a-axis value of 4.043~4.045 Å at room temperature.

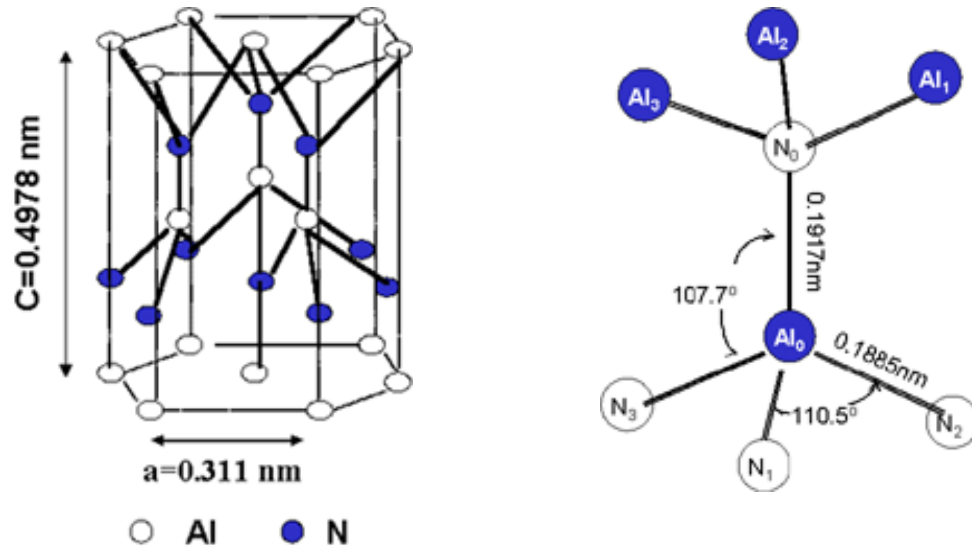


Figure 1-1. Wurtzite structure of the aluminum nitride.

### 1.1.2. Properties of aluminum nitride

AlN exhibits many useful mechanical, thermal and optical properties. Much interest in AlN has been generated after Borom et al. [19] pointed out that AlN should be a good phonon heat conductor. Slack [20] examined thermal conductivities of many nonmetallic crystallites materials including AlN. Thermal conductivity of pure AlN at room temperature has been assumed to be  $\sim 320 \text{ W/mK}$ . The temperature dependence of thermal conductivity in aluminum nitride is shown in *Figure 1-2*. The dependence of the thermal expansion coefficient in the c plane and in the c-direction is [1]

$$\Delta a/a_0 = -8.679 \times 10^{-2} + 1.929 \times 10^{-4} T + 3.400 \times 10^{-7} T^2 - 7.969 \times 10^{-11} T^3 \quad (1-1)$$

and

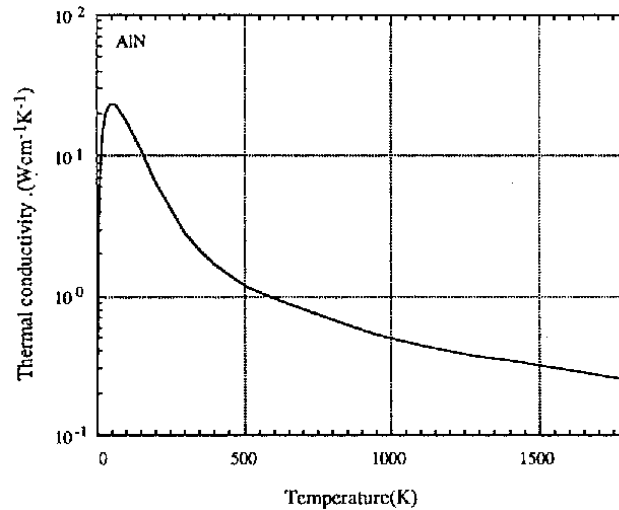


Figure 1-2. Temperature dependence of thermal conductivity of aluminum nitride.

---

$$\Delta c/c_o = -7.006 \times 10^{-2} + 1.583 \times 10^{-4} T + 2.719 \times 10^{-7} T^2 - 5.834 \times 10^{-11} T^3 \quad (1-2)$$

Due to the low intrinsic carrier concentration and the deep native defects and impurity energy level, the electrical characterization of AlN has usually been limited only to resistivity measurement.

The phonon dispersion spectrum of AlN has 12 branches; 3 acoustic and 9 optical. Raman active optical phonon modes correspond to the  $A_1$ ,  $E_1$  and  $E_2$  group.

Aluminum nitride is an extremely hard material (~9 at Mohs' scale) having a high melting temperature over 2000°C. Besides, AlN has a high surface acoustic wave speed (5.67 km/sec) and shows piezoelectric effect and negative electron affinity [21].

The properties of aluminum nitride are shown in Table 1-1.

---

Table 1-1. Physical properties of wurtzite aluminum nitride.

Energy gap	$E_g(300\text{K})=6.2\text{ eV}$ , $E_g(5\text{K})=6.28\text{ eV}$
Lattice constant	$A=3.112\text{ \AA}$ , $c=4.982\text{ \AA}$
Thermal expansion	$\Delta a/a=4.2\times 10^{-6}/\text{K}$ , $\Delta c/c=5.3\times 10^{-6}/\text{K}$
Thermal conductivity	$k=3.2\text{ W/cmK}$
Index of refraction	$n(3\text{eV})=2.15\pm 0.05$ , $n(3.42\text{eV})=2.85$
Dielectric constant	$\epsilon_r=8.5\pm 0.2$ , $\epsilon_\infty=4.68\div 4.84$

---

### 1.1.3. Applications of aluminum nitride

Besides high thermal conductivity, other attractive properties of AlN which make it an ideal candidate for substrate in electronic packaging are (1) low coefficient of thermal expansion, (2) high resistivity, (3) low dielectric constant and low dielectric loss at high frequencies and (4) high dielectric breakdown strength [22,23].

Some applications of AlN thin films include surface passivation of semiconductor and insulators for high temperature [24]. AlN thin films are used for surface acoustic wave (SAW) devices because of their low acoustic loss and high ultrasonic velocity [25]. Aluminum nitride can be used as a tribological coating where there is a need for oxidation and corrosion protection and for improving wear resistance.

## 1.2. Pulsed dc reactive magnetron sputtering

### 1.2.1. Sputtering

Sputtering is one of the most commonly used methods for the deposition of thin films. Sputtering is the ejection of a material due to the transfer of energy from an

energetic particle to a surface. The energetic particles, in the mixture form of ions, neutral atoms, molecules, electrons, neutrons and/or energetic photons, impact the surface at a high energy level greater than bonding energy. The energy transfer creates a collision cascade in the target material leading to the ejection of atoms, ions, molecules, secondary electrons and photons. This process has been utilized to more conveniently deposit a wide range of materials since the momentum exchange is a physical process as opposed to a chemical or thermal process. Films of almost every element in the periodic table have been tried for the sputtering deposition. Usually, sputtering has less contamination effect compared to other chemically-driven deposition techniques and often results in more reproducible characteristics of thin films.

### **Sputter yield**

One measure of success in the sputtering process lies in the yield of deposited films. This is defined as the number of atoms sputtered from the surface per incident particle. It is dependent on many parameters, including the atomic mass, crystallinity and bond strength of target materials and mass and incidence angle of bombarding species. In an elastic collision, momentum transfer between two particles is most efficient if the particles have equal to that of the target atoms. Argon is the most commonly used gas for non-reactive sputtering since its mass is somewhat close to that of many desirable elements and also argon is inexpensive compared to other inert gases. The sputter yield increases as the kinetic energy of the incident particle increases.

### **1.2.2. Magnetron sputtering [26-29]**

Magnetrons sputtering devices have become popular from easiness in technical adjustment and film quality. Magnetrons have been more routinely used to rapidly deposit thin metal films for a broad range of applications from architectural glass and food packaging to thin films microelectronics.

Magnetrons are a class of cold cathode discharge devices used generally in a diode mode. The plasma is initiated between the cathode and the anode at pressures in the mTorr range by the application of a high voltage that can be either DC or RF. The

plasma is sustained by the ionization caused by secondary electrons emitted from the cathode due to ion bombardment which are accelerated into the plasma across the cathode sheath. What differentiates a magnetron cathode from a conventional diode cathode is the presence of a magnetic field. The magnetic field in the magnetron is oriented parallel to the cathode surface. The local polarity of magnetic field is oriented such that  $\mathbf{E} \times \mathbf{B}$  drift of the emitted secondary electrons forms a closed loop. Due to the increased confinement of the secondary electrons in this  $\mathbf{E} \times \mathbf{B}$  drift loop compared to a DC or RF diode device, the plasma density will be much higher, often by an order of magnitude or more, than a conventional RF or DC diode system. The result of the high plasma density and its proximity to the cathode is a high current, relatively low voltage discharge. Typical discharge parameters for a magnetron might be a voltage of 500 V and a current of 5 A, whereas a non-magnetized diode might operate at 2500 V and 0.5 A.

Due to the effective trapping of the energetic secondaries close to the cathode, a high plasma density can be sustained at significantly lower chamber pressures than similar power RF or DC diode plasma. A magnetron operates at a pressure ranging from about 1-2 mTorr to 30-40 mTorr, whereas a typical RF diode might operate at 15-200 mTorr. The low operating pressure results in a significant reduction in gas scattering between the sputtered atoms and the background gas. The result of this reduction is an effective increase in the average kinetic energy of the sputtered atom (less thermalization) and an increase in the probability of atom transport from the cathode to the substrate.

The result of the high discharge currents is the ability to sputter the cathode at a high rate. Deposition rate on surfaces within 5-10 cm from the cathode may be as high as several microns/minute for high sputter yield materials. Usually the typical limiting factor to the maximum deposition rate in a magnetron device is the ability to cool the cathode.

Magnetrons have been developed in a wide range of geometries: each of which satisfies the requirement that the  $\mathbf{E} \times \mathbf{B}$  drift path forms a closed loop.

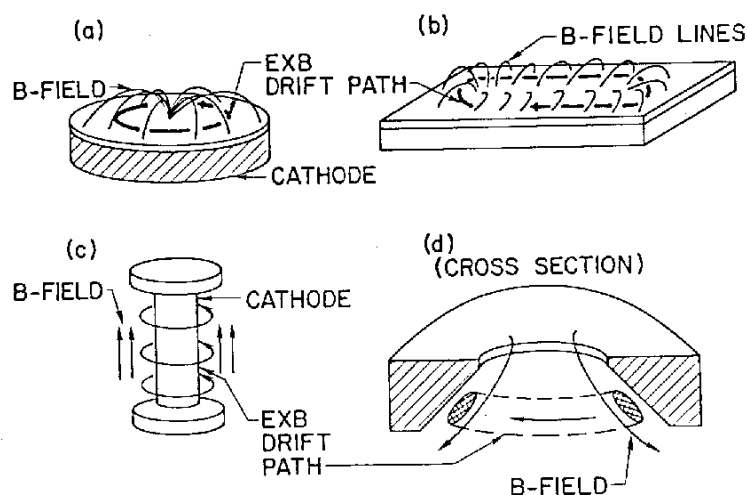


Figure 1-3. (a) Circular planar magnetron, (b) rectangular planar magnetron, (c) cylindrical posy magnetron and (d) conical magnetron.

Three basic classes of geometries exist: the planar, the cylindrical and the conical designs. The planar design (Figure 1-3 (a)) is available in a circular geometry at diameters of from 5 to a few 10's of cm. The rectangular or "racetrack" magnetron (Figure 1-3 (b)) has been developed at lengths exceeding the meter range.

The cylindrical geometry is characterized by a central, cylindrical cathode with an axial magnetic field (Figure 1-3 (c)). The magnetic field in this case is radial and the resultant  $\mathbf{E} \times \mathbf{B}$  drift path forms a band around the cathode. The third geometry is the conical design (Figure 1-3 (d)), which is somewhat similar to the circular planar device. These devices have a cathode surface, which is tilted slightly and typically have an opening on the central axis. Electron motion in electric and magnetic field will be discussed in detail in Chapter 1-4, Plasma physics.

### 1.2.3. Reactive sputtering [26]

Reactive sputter deposition involves the sputtering of a metal, alloy or compound in a reactive gas mixture in order to effectively deposit a compound thin film composed of the sputtered material and the reactive species. A wide variety of compounds have been formed in this way, with a wide range of properties. In some cases, these compounds are difficult or impossible to form by other means, particularly at low substrate temperature. The process of reactive sputter deposition can be very complex and involves the sputtering process, the physics of the plasma discharge, transport of the sputtered and gas species, the kinetic of film growth and chemical interactions at the target and film surfaces. These all interact in a certain way and therefore can affect the properties of the film.

There are many applications for reactively sputter deposited films. Examples of reactive sputtering include the deposition of aluminum nitride or aluminum oxide using an aluminum target and the deposition of titanium oxide using a titanium target with assistance of nitrogen or oxygen gas.

Without introduction of a reactive species, e.g., oxygen or nitrogen, the film deposited by the sputtering process would be metallic. Upon introduction of a reactive gas species, it will combine with the sputtered atoms from the target to form a compound thin film. At low levels of the reactive species, the films will be only partially reacted. This is known as the metallic mode of reactive sputter deposition since the formation rate of the insulating compound is slower than the sputter rate. The target will remain metallic and the deposited films are usually metal rich. As the concentration of reactive gas in the gas mixture increases, the films will be fully reacted and deviated from the metallic state. However, even higher levels of the reactive species often cause the formation of identical compounds on the surface of target or cathode. This is known as the non-metallic or poisoned mode of reactive sputter deposition in which the rate of formation of compound is greater than the sputter rate. This buildup of an insulating material on the target surface decreases the deposition rate due to low sputter yield of the insulating layer compared to the pure metal.

The technique is not quite as simple as it sounds. The reaction could take place at any following locations:

- (a) At the target
- (b) In the gas phase
- (c) On the substrate surface

If the reaction takes place at the target, it produces an insulating film that terminates the deposition process with accompanying DC or RF discharge. Reactions in the gas phase often lead to further agglomeration or nucleation of the resulting molecules so that the material arrives at the substrate in the form of large particles or “powder”. It introduces friable coating of limited utility.

It is better to have the reaction only on the substrate surface. In order to achieve this goal, the deposition process and experimental parameters must be well controlled.

#### **1.2.4. Pulsed DC Sputtering**

Pulsed plasma processing has found increasing acceptance over last decades, particularly for the surface treatment of materials used in data storage, flat panel, semiconductor and other industrial applications. Pulsed DC processing is a sputtering technique combining the advantages of DC and RF sputtering. RF sputtering may produce better quality insulating films, but deposition rates are very low. The RF systems are usually complex and difficult to be used for the scale up of commercial products. The main problem in the DC reactive sputter deposition of insulating materials from an elemental metal target in a mixture of argon and reactive gas is that an insulating film may be formed on the target surface. This insulating layer is charged by the positive ions that are accelerated in the plasma and collected on this surface. If the insulating layer can sustain an infinite electric field strength this layer is ultimately charged to the applied power supply voltage  $V_a$ . As a consequence, there will be no potential difference left to accelerate ions and electrons in the plasma and the plasma will therefore disappear and the sputtering process will stop. Normally the insulating film at the target can withstand an electric field strength of up to 1-10 MV/cm before electrical breakdown in the layer occurs. During such a breakdown (micro-arc) small particles may be ejected

from arcing tracks. These micro particles may reach the substrate and become imbedded in the growing film. This will be detrimental to the intended film properties.

It has been shown that many existing restrictions, which is related to charging effects occurring during a dielectric deposition such as alumina and aluminum nitride, can be overcome by using pulsed DC sputtering in the range of 10-250 kHz [30-45]. These power supplies are known to provide higher ionization rates without target poisoning and can improve the film quality by decreasing the amount of macroparticles caused by microarcs.

A pulsed DC power supply can create conditions that eliminate the arcing at the target by interrupting the negative voltage and applying a short positive pulse to the target. This positive pulse will attract electrons to the target. This flux of negative particles will discharge fully or partially the insulating layer on the target. In this way arcing can be avoided. The duration of the reverse pulses,  $\tau_{rev}$  is determined by the need fully to discharge the dielectric surface. Experiments have shown that the time required to accomplish this can be as short as one microsecond to as long as tens of microseconds [35].

The followings are simple calculations for selecting a suitable pulse frequency when operating the reactive sputtering process with a pulsed DC power supply [35]. For the first order approximation the dielectric layer on the target may be described as a parallel plate capacitor where dielectric layer represents the thickness (d) between the parallel plates as shown in *Figure 1-4*. The voltage build up ( $V_D$ ) on this capacitor will follow the simple relation

$$Q = V_D C \quad (1-3)$$

where Q is the charge on the capacitor C formed by the dielectric. The capacitor C can be expressed as

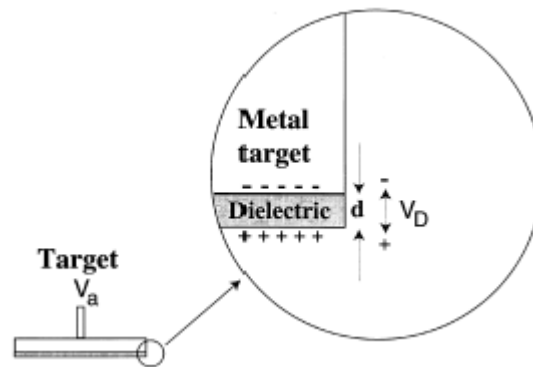


*Figure 1-4.* Schematic of the target surface during reactive DC sputtering of an insulating material. The dielectric layer is charged by positive ions causing a voltage build up,  $V_D$ , across the insulating layer with thickness  $d$ .

---

$$C = \epsilon\epsilon_0 \frac{A}{d} \quad (1-4)$$

and the voltage  $V_D$  can be written as

$$V_D = Fd \quad (1-5)$$

where  $F$  is the electric field strength in the dielectric layer.

Due to the ion current density  $J$  (during the negative part of a duty cycle) charge will be collected in the capacitor. The charge build up can be written

$$Q = JAt \quad (1-6)$$

where  $t$  is the time that the constant current density  $J$  has passed through the applied current to the dielectric layer.

Combining Eqs (1-3) ~ (1-6) will result in an expression for  $F$

$$F = \left( \frac{J}{\epsilon\epsilon_0} \right) t \quad (1-7)$$

A maximum charging time  $t$  of  $2 \times 10^{-4}$  sec is obtained by assuming that a relative dielectric constant  $\epsilon$  is close to 8, an average ion current density  $J$  is 20 mA/cm<sup>2</sup> and arcing will occur when the dielectric has been charged to a critical field strength  $F$  of 5 MV/cm. This corresponds to a minimum pulse repetition frequency of approximately 10 kHz to avoid arcing. Operating DC pulse frequencies needs practically to be in the region of 50-100 kHz to assure absolute arc-free operation.

The mobility of the electrons is much higher than that of the ions due to the lower mass of electrons compared to ions. The discharge current (positive period) is typically much higher than the charging current (negative period). Therefore, the discharge may take place in a much shorter time than the charging. From this difference in mobilities it is reasonably assumed that the discharge occurs within the 10% of the charging time.

#### 1.2.5. Types of pulsed DC power

There are two modes of operation; (1) unipolar pulsed sputtering (*Figure 1-5 (a)*) where target voltage is pulsed between the normal operating voltage and ground [30]; and (2) bipolar pulsed sputtering where target voltage is actually reversed and become positive during the pulsed-off period [30-39].

The bipolar pulsed DC power supplies produces either a bipolar symmetric or asymmetric pulse as are shown in *Figure 1-5 (b) and (c)*. With the symmetric pulsed DC power [35,36], the pulse height is of equal magnitude for both the positive and negative pulses. In between the pulses there is an off time, and the width of positive pulse is usually smaller than the width of the negative pulses. The idea is to spend just enough

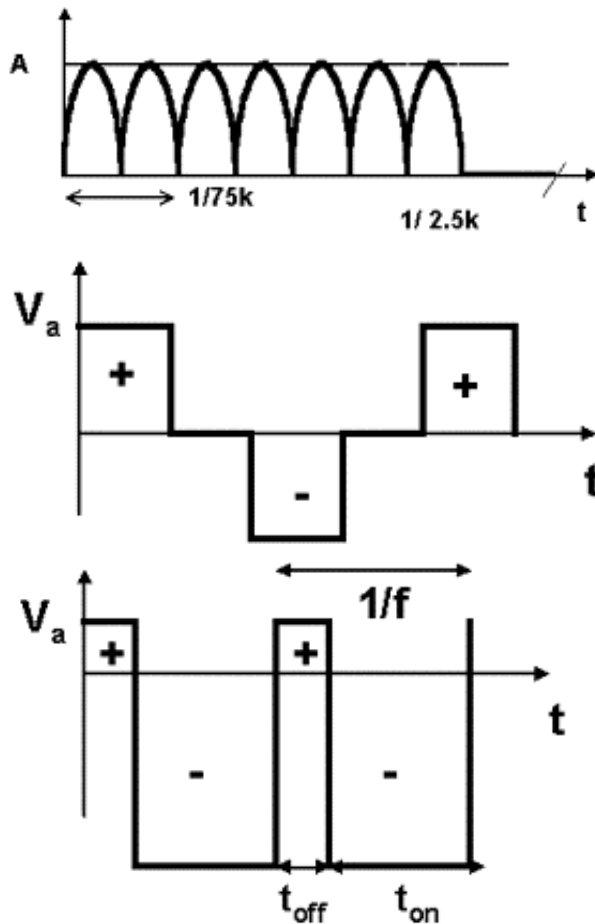


*Figure 1-5.* Three types of pulsed DC power wave form (a) unipolar, (b) symmetric bipolar and (c) asymmetric bipolar.

---

time to discharge the target surface with the positive pulse. Since no sputtering takes place during the positive pulse, the width of positive pulse should be as small as possible. Dual cathodes are used for symmetric pulsed power. These two cathodes, which are located side by side, are both connected to the same symmetric bipolar pulsed DC power

supplies. One power lead goes to one cathode and the other lead is connected to the second cathode. With this electrical hookup, one is the anode for the system, while the other is the cathode. When the polarity of the voltage on the target changes, the anode and cathode switch each other as well. By operating in this manner, very long term process stability is achieved even after 300 hours. Industrial applications of this process may include the deposition of high quality optical coating on materials such as architectural or automotive glass and polymer web.

For the asymmetric pulsed DC power supplies [33-39], the positive pulse voltage is only a fraction of the negative pulse voltage. The pulse changes from positive to negative without off time. Similar to symmetric bipolar pulsed DC power, the width of the positive pulse is usually smaller than the negative pulse. With both bipolar symmetric and asymmetric pulsed DC power supplies, sputtering takes place from the target during the negative pulse whereas discharging of the target surface takes place during the positive pulse. The reverse voltage is set to 10% of the normal operating voltage. It is known [38] that reverse voltage did not appear to influence the number of arc events detected. However, it has a significant effect on the deposition rate of the coating. This effect has been attributed to enhanced target cleaning during the voltage reversal at the end of the pulse-off periods.

#### **1.2.6. Structure Zone model [46-52]**

Polycrystalline thin films prepared by various techniques exhibit the large variety of structures considering size, morphology, and orientation of crystals as well as microchemistry of the films. Structural inhomogeneity along the film thickness can also be present. The structure zone model (SZM), constructed by the compilation of experimental results, presents an important guide for systematizing both the experimental results and the dependence of structures on the deposition temperature (considering homologous temperature,  $T_s/T_m$  (in K), where  $T_s$  is the substrate temperature and  $T_m$  is the melting point of the film material). Thornton [47,48] constructed the structure zone model with regard to sputtering pressure and homologous temperature changes.

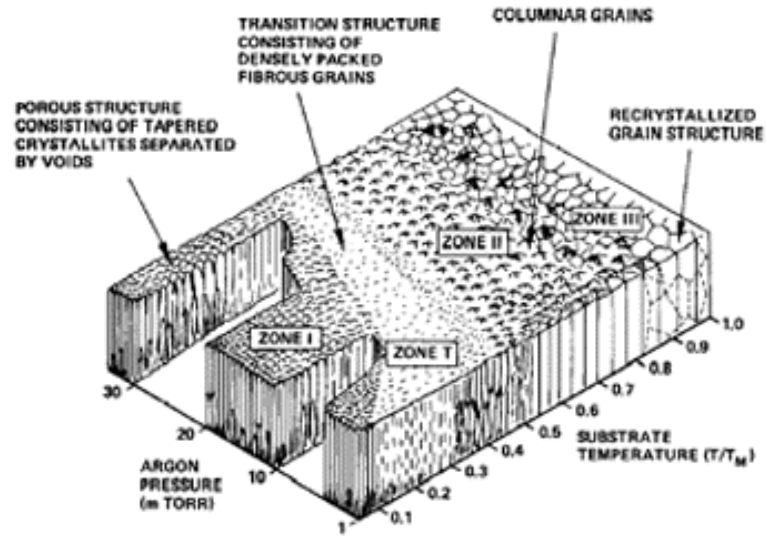


*Figure 1-6.* Characteristics of the four basic structural zones. The ratio of substrate  $T_s$  to film melting ( $T_s/T_m$ ) increases in the direction  $Z1 \rightarrow ZT \rightarrow Z2 \rightarrow Z3$ .

Messier [49] revised the zone model by adding the effect of ion bombardment- and thermal-induced mobility when a bias to the substrate is applied. Later Kelly et al. [50,51] developed a structure zone model relating to the closed field unbalanced magnetron sputtering system, where coating structures are described in terms of homologous temperatures, bias voltage and ion-to-atom incident at the substrate. Barna and Adamik [52] modified further the structure zone model constructed in conjunction with the concentration of impurities. By analyzing the structure zone models published in the literature, the various structure zones can be characterized by the following way. (*Figure 1-6*).

In zone I, the film is composed of fibers of small diameters (1-10 nm) determined by the nucleation density and statistical fluctuation. The crystalline fibers grow out of the primary nuclei and proceed to the top of the film.

The fibers are often collected into bundles. This is a rather homogeneous structure along the thickness of the film with increasing diameter of fibers by increasing  $T_s/T_m$ . The crystals contain probably high density of defects and the grain boundaries are porous. This structure belongs to the temperature interval  $0 < T_s/T_m < 0.2$  where neither the bulk diffusion nor the self surface diffusion has a remarkable value.

In zone T, the structure is inhomogeneous along the film thickness. There are fine crystalline phases at the substrate, composed of V-shape grains in the next thickness range. The grains may become columnar in the upper part of thick films. This zone belongs generally to the temperature interval  $0.2 < T_s/T_m < 0.4$  in which self-surface diffusion is remarkable but the grain boundary migration is strongly limited.

Zone 2 represents a homogeneous structure along the film thickness composed of columns penetrating from the bottom to the top of the film. The grain boundaries are nearly perpendicular to the film plane. This zone corresponds to the area of high substrate temperatures ( $T_s/T_m > 0.4$ ).

In zone 3, the structure is characterized by equiaxed (globular) three dimension grains. This kind of structure is generally attributed to the high substrate temperature range.

*Figure 1-7* illustrates the structures at the various temperatures with increasing film thickness. Nucleation density determines lateral sizes of the fibers in the temperature interval corresponding to Zone 1. The orientation of fibers follows the random orientation of the nuclei. The competitive growth of differently oriented neighboring crystals is developed in Zone T. The texture changes with the thickness in this zone. The substrate-near part shows random orientation while the competitive growth texture is increasing as film grows. As the temperature increases, the effect of grain boundary migration increases. Randomly oriented small grains are dissolved gradually by coalescence and grain coarsening.

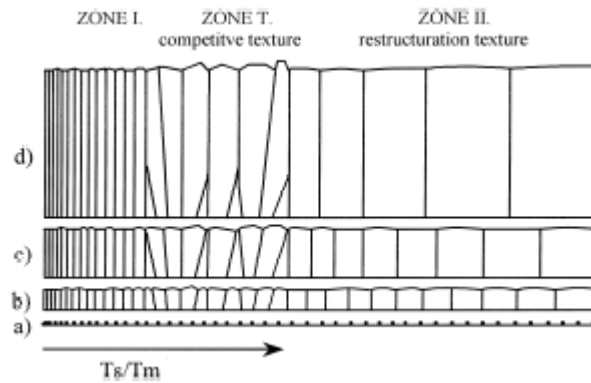


Figure 1-7. Basic structure zone with various thickness.

This strong reconstruction is controlled by the minimization of the interface and surface energy and develops the reconstructive growth texture.

### 1.3. Plasma Physics

Plasma is a gas containing charged and neutral species, including some or all of the following: electrons, positive ions, negative ions, atoms and molecules. On average plasma is electrically neutral, because any charge imbalance would result in electric fields that would tend to move the charges in such a way as to eliminate the imbalance. As a result, the density of electrons plus the density of negative ions will be equal to the density of positively charged ions. An important parameter of plasma is the degree of ionization, which is the fraction of the original neutral species (atoms and/or molecules) which have become ionized. Plasma with a degree of ionization much less than unity is referred to as weakly ionized. The presence of a relatively large population of neutral species will dominate the behavior of this type of plasma. In fully ionized plasmas, the degree of ionization approaches unity and neutral particles play little or no role [53].

To form and sustain plasma requires some energy source to produce the required ionization. In steady state, the rate of ionization must balance the losses of ions and electrons from the plasma volume by recombination and diffusion or convection to the boundary.

A convenient unit for the electron temperature is the electron volt (eV) which is equivalent to a temperature of 11604 K. For plasma process, the electron densities are in the range of  $1 \times 10^9$  to  $1 \times 10^{12} \text{ cm}^{-3}$ , and average electron energies between 1 and 10 eV. The degree of ionization for these plasmas varies about  $10^{-6}$  to as high as 0.3 [53].

### 1.3.1. Plasma oscillations

If a charge imbalance occurs in plasma, the electrons will move to shield out its effects. This does not happen instantaneously, however. A reasonable estimate of the time it takes for the shielding occurrence would be the time required for an electron to move a Debye length  $\lambda_D$ . This time  $t_p$  is

$$t_p = \frac{\lambda_D}{v} = \left( \frac{\epsilon_0 m_e}{ne^2} \right)^{1/2} \quad (1-8)$$

where  $v$  is the velocity of an electron,  $\epsilon_0$  is the permittivity of vacuum,  $m_e$  is the electron mass,  $e$  is the charge and  $n$  is the electron density.

Furthermore, we might imagine that the electrons, moving under the force of the electric field from the charge imbalance, may “overshoot” and execute an oscillatory motion. The electrons will oscillate at a frequency which is just the inverse of  $t_p$  called the plasma frequency

$$\omega_{pe} = t_p^{-1} = 5.64 \times 10^4 \sqrt{n_e (\text{cm}^{-3})} \quad (1-9)$$

For ions,

$$\omega_{pi} = \left( \frac{Z^2 e^2}{m_i \epsilon_0} \right)^{1/2} (n_i)^{1/2} \quad (1-10)$$

The plasma will screen out an oscillatory field with a frequency below  $\omega_p$ , but above this frequency, the electrons cannot respond fast enough to accomplish the shielding.

### 1.3.2. Effects of electric fields and magnetic fields

In the presence of an electric field  $\mathbf{E}$  and magnetic field  $\mathbf{B}$ , a particle of charge  $q$  and velocity  $\mathbf{v}$  will experience a force  $\mathbf{F}$  given by:

$$\mathbf{F} = q\mathbf{E} + q\mathbf{v} \times \mathbf{B} \quad (1-11)$$

The quantities,  $\mathbf{F}$ ,  $\mathbf{E}$ ,  $\mathbf{v}$  and  $\mathbf{B}$  are all vectors. Particle orbit are calculated by using Newton's second law to relate the particle acceleration  $\mathbf{a}$  to the force:

$$\mathbf{F} = m\mathbf{a} \quad (1-12)$$

where  $m$  is the particle mass. Several cases will be considered to illustrate typical particle motions.

#### Case 1; E=constant, B=0

In this case, a particle will experience a constant acceleration in the direction of  $\mathbf{F}$  which is given by

$$\mathbf{a} = q\mathbf{E}/m \quad (1-13)$$

#### Case 2; E=0, B=constant

The magnetic force acts in a direction to the velocity of the charged particle. If a particle is at rest ( $\mathbf{v}=0$ ), then there is no force and the particle at rest. For a non-zero

velocity, let us define the component of velocity of the particle parallel to B to be  $v_{\parallel}$  and the velocity component perpendicular to B to be  $v_{\perp}$ . For the case of  $v_{\parallel}=0$ , the particle will move in a circular orbit perpendicular to the direction of B. The radius of the orbit is gyro radius R and is given by

$$R = \frac{mv_{\perp}}{q|B|} \quad (1-14)$$

$$R = \frac{(2mE)^{1/2}}{q|B|} \quad (1-15)$$

where E is the kinetic energy of the particle given by  $E=mv_{\perp}^2/2$ . For particles having the same energy, the heavier species will have larger circular orbits.

The frequency of rotation of a particle in a magnetic field is called the gyro frequency or cyclotron frequency  $\omega$  and is given by

For electrons,

$$\omega_{ce} = \frac{qB}{m_e} = 1.756 \times 10^{11} B \text{ B in Tesla} \quad (1-16)$$

For ions,

$$\omega_{ci} = \frac{ZqB}{m_i} \quad (1-17)$$

where Z is charge number of the ion. The gyro frequency  $\omega$  is given in units of radians/sec and is related to the frequency f in Hz by

$$\omega = 2\pi f \quad (1-18)$$

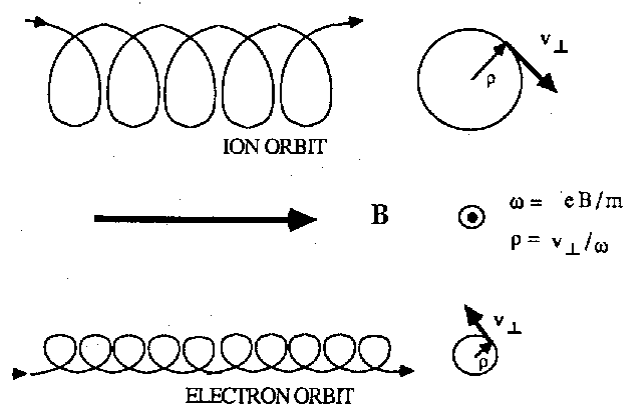


Figure 1-8. Orbits of ions and electrons in a homogeneous static magnetic field  $\mathbf{B}$ .

A particle follows a helical orbit, with a gyro frequency  $\omega$  that is independent of the particle energy. It should be noted that  $\omega$  is independent of the particle energy while the gyro radius will increase with particle energy,

The component of the particle velocity to the magnetic field,  $v_{\parallel}$ , is not affected by  $\mathbf{B}$ . Thus the general orbit of a charged particle in a magnetic field is a helix as shown in Figure 1-8. The sign of the charge will determine the sense of the helix; electrons and ions will have opposite directions of rotation.

### Case 3; $\mathbf{E}=\text{constant}$ , $\mathbf{B}=\text{constant}$

If  $\mathbf{E}$  is parallel to  $\mathbf{B}$ , then it acts on the particle just as in Eq. (1-13), i.e.,  $\mathbf{B}$  has no effect on the component of velocity parallel to itself.

If  $\mathbf{E}$  is perpendicular to  $\mathbf{B}$ , then the particles will undergo a drift motion which is perpendicular to both  $\mathbf{E}$  and  $\mathbf{B}$  and has a magnitude given by  $v_{\mathbf{E} \times \mathbf{B}}$  (Figure 1-9). The  $v_{\mathbf{E} \times \mathbf{B}}$  is expressed by

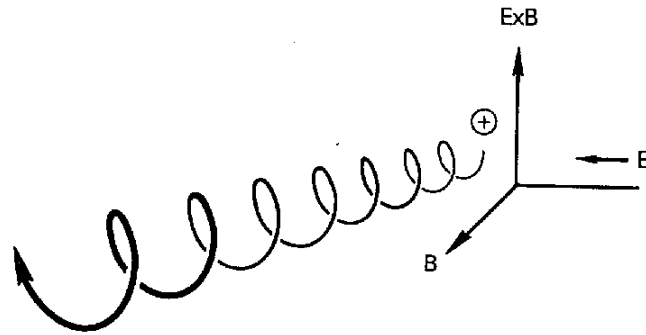


Figure 1-9. Particle drifts in crossed electric and magnetic field.

---

$$v_{E \times B} = \frac{E}{B} \quad (1-19)$$

The drift velocity is independent of the particle charge and mass. It is assumed in Eq. (1-19) that the particles are free to undergo gyro motion. Collisions may interrupt the gyro motion, in which Eq. (1-19) will not be valid. This drift will operate on electrons in the cathode region of a magnetron where the electric field has a component perpendicular to the magnetic field.

#### Case 4; Nonuniform field

There are two cases in the non-uniform field: non-uniform magnetic field and non-uniform electric field.

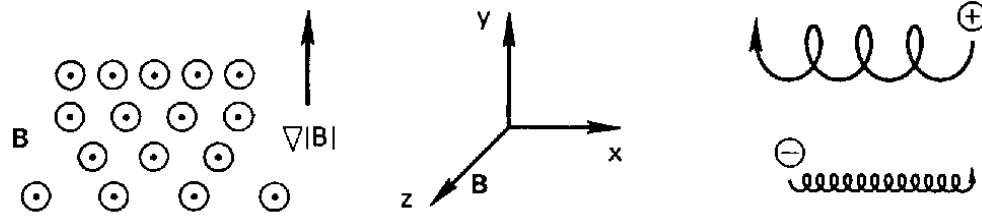


Figure 1-10. The drift of a gyrating particle in a nonuniform magnetic field.

#### Case 4-1. Nonuniform magnetic field

A nonuniform magnetic field results in additional drift motion (*Figure 1-10*). In particular, a field gradient will produce a drift velocity,  $v_g$ , which is perpendicular to both the field and the gradient, given by

$$\mathbf{v}_g = \left( \frac{v_{\perp}^2}{\omega} \right) \left( \frac{\mathbf{B} \times \nabla \mathbf{B}}{2B^2} \right) \quad (1-20)$$

Unlike the  $\mathbf{E} \times \mathbf{B}$  drift, a gradient will depend on the particle mass, charge and velocity. If the magnetic field is curved as shown in *Figure 1-11*, the particle will experience a drift velocity  $v_c$ , which is perpendicular to both the field and its direction of curvature, given by

$$\mathbf{v}_c = \left( \frac{v_{\parallel}^2}{\omega} \right) \left( \frac{\mathbf{R}_c \times \mathbf{B}}{BR_c^2} \right) \quad (1-21)$$

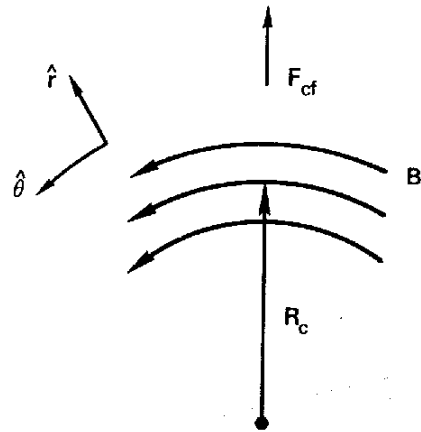


Figure 1-11. A curved magnetic field.

---

Here  $R_c$  is the radius of curvature of field. As in the gradient drift,  $v_c$  depends on the particle mass, charge and velocity. As in the case of  $\mathbf{E} \times \mathbf{B}$  drift, it is implicit in the above two formulae that the particles undergo full gyro radii.

In a magnetron discharge, the magnetic field will usually have both curved and a gradient, so that the drifts in Eqs (1-20) and (1-21) will affect the electrons in the discharge, providing the rate of collisions is low enough to permit the electrons to execute their gyro motion. For the case having both curved and gradient magnetic field like in a usual magnetron discharge,  $v_{g,c}$  is given by

$$v_{g,c} = \frac{m}{q} \left( v_{//}^2 + \frac{1}{2} v_{\perp}^2 \right) \frac{\mathbf{B} \times \mathbf{R}_c}{B^2 R_c^2} \quad (1-22)$$

*Case 4-2. Nonuniform electric field [29]*

If the magnetic field is uniform and the electric field is nonuniform (ex. different electrode area or a charge separation due to density distribution in the plasma during a wave motion), the drift,  $v_E$  due to this is given by

$$v_E = \left(1 + \frac{1}{4} R^2 \nabla^2\right) \frac{\mathbf{E} \times \mathbf{B}}{B^2} \quad (1-23)$$

The second term is called the finite-larmor (gyro)-radius effect. Since  $R$  is much larger than for electrons,  $v_E$  is no longer independent of species. If a density distribution occurs in plasma, an electric field can cause the ions and electrons to separate, generating another electric field.

Another case is time varying electric field with uniform  $\mathbf{E}$  and  $\mathbf{B}$  in space. The drift has two components. The component, perpendicular to  $\mathbf{E}$  and  $\mathbf{B}$ , is usual  $\mathbf{E} \times \mathbf{B}$  drift, except that  $v_E$  oscillates at a frequency  $\omega$ , electric field oscillation. The component along the  $\mathbf{E}$  direction is a new drift, called the polarization drift. The polarization drift is defined as

$$v_p = \pm \frac{1}{\omega_c B} \frac{dE}{dt} \quad (1-24)$$

Since  $v_p$  is in opposite direction for ions and electrons, there is a polarization current; for  $Z=1$

$$J_p = ne(v_{ip} - v_{ep}) = \frac{ne}{eB^2} (M + m) \frac{dE}{dt} = \frac{\rho}{B^2} \frac{dE}{dt} \quad (1-25)$$

where  $\rho$  is the mass density.

The physical meaning for the polarization is as follows (*Figure 1-12*). Consider an ion at rest in a magnetic field.

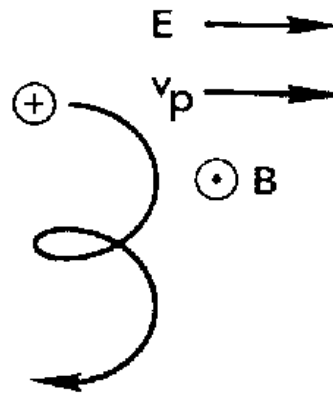


Figure 1-12. The polarization drift.

---

If an  $E$  field is suddenly applied, the first thing the ion does is move in the direction of  $E$ . Only after picking up a velocity does the ion feel a Lorentz force  $e\mathbf{v} \times \mathbf{B}$  and begin to move downward. If  $E$  is kept constant, there is no further  $v_p$  drift and only  $v_E$  drift. However, if  $E$  is reversed, there is again momentary drift.

### 1.3.3. Potentials in glow discharge

Several potentials are important in the plasma processing; the plasma potential  $V_p$ , the floating potential  $V_f$ .

The plasma potential  $V_p$  is the potential at the glow region of the plasma, which is normally considered nearly equipotential. It is the most positive potential in the chamber and the reference potential for the glow discharge.

The floating potential ( $V_f$ ) is the potential at which equal fluxes of negative and positive species arrive at an electrically floating surface in contact with plasma. The criterion for net zero current becomes:

$$\left( n_e \exp - \frac{e(V_p - V_f)}{kT_e} \right) \frac{v_e}{4} = n_i 0.6 \left( \frac{kT_e}{m_i} \right)^{1/2} : \quad (1-26)$$

$$\therefore V_p - V_f = \frac{kT_e}{2e} \ln \left( \frac{m_i}{2.3m_e} \right) \quad (1-27)$$

where  $n$  is the charge density,  $m$  is the mass,  $T_e$  is the electron temperature and  $v_e$  is the thermal velocity of electron ( $e$  for electron and  $I$  for ion). In argon plasma ( $m_{Ar}=6.63 \times 10^{-26}$  kg,  $m_e=9.11 \times 10^{-31}$  kg), for example,  $V_p-V_f$  becomes

$$V_p - V_f \approx 5kT_e \quad (1-28)$$

The above equation can be used to estimate the maximum energy when positive ions bombard electrically insulated chamber walls. The logarithmic dependence minimizes the change in potential due to the increased ion flux. Most threshold energies of sputtering range between 20 and 30eV. The  $V_p-V_f$  value less than 20 to 30V is beneficial in avoiding sputtering off the walls, which may lead to film contamination.

#### 1.4. Thermal Conduction Mechanism

Characterization of thermal properties in solids is important in the scientific and practical points of view. Especially, thermal management in electronic applications becomes even more important with increasing power generations. Therefore, high thermal conductivity materials such as diamond and aluminum nitride films have been studied with a lot of attention in electronic packaging and cutting tools applications. Aluminum nitride is being considered as a candidate for filler in printed circuit board (PCB) to improve heat dissipations [58]. Diamond films have been coated on the surface of cutting tools to enhance thermal conductivity and protect them [59]. This section describes some known basic theory about thermal properties and conduction mechanisms in solids.

### 1.4.1. Thermal conductivity and thermal diffusivity

Thermal conductivity and thermal diffusivity are two basic parameters when describing thermal properties of a material. They both describe the capability of a material to transmit heat, but from different viewpoints.

Thermal conductivity  $k$  relates how much heat passes through a given sample of unit area and unit thickness for a given temperature gradient. It is defined as

$$\frac{dQ}{dt} = -kA \frac{dT}{dx} \quad (1-29)$$

where,  $dQ$  is the amount of heat flowing normal to the area  $A$  in time of  $dt$ . The heat flow is proportional to the temperature gradient  $-dT/dx$ , thermal conductivity  $k$ . The unit for  $k$  is W/mK. The inverse of the thermal conductivity is defined as thermal resistivity  $w$ .

Under steady state conditions in which the heat flux,  $q=dQ/dt$  and temperature at each point are independent of time, Eq. (1-29) needs to be integrated for the particular shape of interest. For heat flux through a flat slab, this becomes

$$q = -kA \frac{T_2 - T_1}{x_2 - x_1} \quad (1-30)$$

For radial heat flow in a cylindrical shape of length  $l$ , inner diameter  $D_1$  and outer diameter  $D_2$ , the heat flux is expressed as

$$q = -k(2\pi l) \frac{T_2 - T_1}{\ln D_2 - \ln D_1} \quad (1-31)$$

Similar relationships can be derived for many other simple shapes. Complex shapes often require approximation methods.

The rate of temperature  $dT/dt$  depends on the ratio of thermal conductivity to heat capacity per unit volume  $\rho c_p$  under non-steady state condition. This ratio is called

thermal diffusivity  $k/\rho c_p$  and has the same units as for material diffusivity,  $\text{cm}^2/\text{sec}$ . The rate change of temperature  $dT/dt$  is given by [60]

$$\frac{dT}{dt} = \frac{d\left(\frac{k}{\rho c_p} \frac{dT}{dx}\right)}{dx} \quad (1-32)$$

Experimentally, a temperature change resulting from a known flow of heat through the sample needs to be measured to obtain thermal conductivity. The accuracy of the measurement is limited because of the uncertainty in the quantity of the heat flow through the sample, which is often affected by losses from infrared radiation.

Therefore, only the time difference for temperature disturbance over a distance is measured to obtain diffusivity. This is the favored mode of operation in many methods for diffusivity measurement because calorimetry can be avoided. Once the thermal diffusivity is measured, thermal conductivity can be computed by using the value of  $\rho c_p$  from bulk samples. The thermal diffusivity represents the ability of the material to disperse heat and is a relevant property when the material is used as a heat sink or heat spreader.

There is an extra thermal resistance due to the interface between two materials, called Kapitza resistance  $R_k$ . When heat flows across the boundary of the two materials,  $R_k$  can be expressed by temperature jump  $\Delta T$  and heat flux  $Q$  as following

$$R_k = \frac{\Delta T}{Q} \quad (1-33)$$

where  $R_k$  is Kapitza resistance and  $Q$  is heat flux. This is determined by the mismatch of the elastic properties between the two materials, namely the probability that each phonon is transmitted across the interface. The contribution of  $R_k$  becomes dominant when a multilayered structure has fairly large mismatch in elastic properties between materials.

The measurement of  $R_k$  or its inverse, the Kapitza conductance  $\sigma_k$ , can be carried out by using several optical or thermal techniques. In thermal conductivity or thermal diffusivity measurements, this quantity is often ignored although it may potentially cause problems with the accuracy of the measurements.

#### **1.4.2. Thermal conduction processes**

The conduction process for heat-energy transfer under the influence of a temperature gradient depends on energy concentration per unit volume, velocity of movement and its rate of dissipation with the surroundings. Each of these factors must be understood in order to predict the resulting thermal conductivity. It is known that thermal conduction in solids is a result of heat transfer by three carrier types: charged particles like free electrons, phonons, and photons. Since aluminum nitride is an insulating material, the effects of free electrons can be ignored. Also contribution of photon can be ignored at room temperature. Therefore, only dominant phonon thermal conductivity will be discussed in this section.

##### **1.4.2.1. Phonon conductivity**

Phonons, quanta of atomic vibrational modes, are the main heat carrier in nonmetallic solids [60-62]. While phonons travel with a near speed of sound through solids, they are scattered. There are several sources that can contribute to the scattering of phonons, which results in decreasing their mean free paths and in turn the thermal conductivity of the material. The phonon scattering is affected by phonons, lattice defects and free electrons, if present.

The scattering with other phonons is generally divided by two categories. N- (or normal) process is momentum conserving and therefore does not actually provide a source of thermal resistance. The major contribution responsible for a finite thermal conductivity and energy dissipation from thermal elastic waves is the U- (Umklapp) process. For a dielectric material, U process is the only intrinsic source of thermal resistance. Because the atomic vibration and number of phonon modes increase with

increasing temperature, the Umklapp scattering becomes very pronounced at high temperatures, particularly above the Debye temperature. It is convenient to express the reverse time between Umklapp scattering events as:

$$\tau_u^{-1} = A \frac{\hbar^2 \omega^2}{k^2} T^3 e^{-\frac{B}{T}} \quad (1-34)$$

where  $k$  is Boltzmann's constant and  $\hbar$  is Planck's constant divided by  $2\pi$ ,  $\omega$  is the phonon frequency and  $A$  and  $B$  are constants, usually obtained empirically from  $k$  data collected across a wide temperature range. The power of  $T$  in the pre-exponential factor is partially uncertain, with various groups using values from 1 to 4. This does not strongly affect results because of the overriding variation with  $T$  present in exponential term.

In addition to phonon interaction, point defects provide a large source of phonon scattering. The size, mass and modulus differences of the impurity atom with respect to the host material play a role in disturbing the periodic lattice enough to cause phonon to scatter. The largest effect is from the mass differential and the scattering relaxation time for point defects may be written:

$$\tau_{imp}^{-1} = A_{imp} \omega^4 \quad (1-35)$$

where the term  $A_{imp}$  is given by:

$$A_{imp} = \frac{\Omega_o}{4\pi v_s^3} c_i (1 - c_i) \left( \frac{\Delta M}{M} \right)^2 \quad (1-36)$$

where  $\Omega_o$  unit cell volume,  $v_s$  the velocity of sound,  $c_i$  volume concentration of the impurities which produce a fractional mass change of  $\Delta M/M$ . For vacancies,  $\Delta M/M=1$ .

Dislocations scatter phonons as well, due to the strain field associated in the material by their presence. This is not a very strong source of scattering, however, unless

the dislocation density is particularly high and the dislocation lines run perpendicular to the temperature gradient. For an array of screw dislocations oriented perpendicular to the temperature gradient,

$$\tau_{dis}^{-1} = 0.033N_d b^2 \gamma^2 \omega \quad (1-37)$$

where  $N_d$  is the dislocation density,  $b$  is the Burgers vector of the dislocation and  $\gamma$  the Grüneisen parameter for the material.

Stacking faults and other planar defects have a minor influence on phonon scattering, estimated to be:

$$\tau_{sf}^{-1} = A_s \omega^2 \quad (1-38)$$

where  $A_{sf}$  is a term including fault size and material properties.

Finally, there is phonon-grain boundary interaction. Low angle grain boundaries are expected to scatter much like an array of dislocations while more distinct grain boundaries act as internal interruptions to phonon motion. In general,

$$\tau_{bund}^{-1} = \frac{v_s}{d} \quad (1-39)$$

The boundary scattering described by Eq. (1-39) occurs not only at grain boundaries, but at any distinct boundary across which the lattice is not repeated. This is generally referred to as “size effect”,

The total scattering relaxation time  $\tau$  can be obtained by adding up the inverse of scattering relaxation time for the various processes and given by

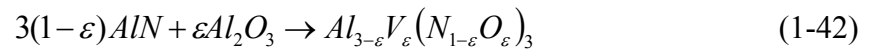
$$\tau^{-1} = \sum_i \tau_i^{-1} \quad (1-40)$$

The frequency of these lattice waves covers a range of values and scattering mechanisms or wave interactions may depend on the frequency. The thermal conductivity can be represented by the relation

$$k = \frac{1}{3} \int c(\omega) v(\omega) d\omega \quad (1-41)$$

where  $c(\omega)$  is the contribution to the specific heat per frequency interval for lattice waves of that frequency and  $l(\omega)$  is the attenuation length for the lattice waves.

Phonon scattering by defects due to oxygen presence in aluminum nitride was calculated [20, 59]. The oxygen is incorporated as dissolved  $Al_2O_3$  according to



Here  $\varepsilon$  is defined as:

$$\varepsilon = \frac{\Delta n}{n_o} \quad (1-43)$$

where,  $\Delta n$  is the number of the oxygen impurities and  $n_o$  is the number density of the nitrogen atoms in AlN;  $n_o = 4.79 \times 10^{22} \text{ cm}^{-3}$ . The oxygen replaces nitrogen and the aluminum deficit produces vacancies in the aluminum sublattices. These defects produce a thermal resistivity at room temperature of: [20, 59]

$$\left( \frac{\Delta W}{\varepsilon} \right) = 43 \text{ cmK/W} \quad (1-44)$$

### 1.4.2.2. High thermal conductivity materials

Those crystals for which  $k$  exceeds 100 W/mK at room temperature are considered to possess a high thermal conductivity [57,59,60]. Only a few nonmetallic crystals fall into this category. Most of them are adamantine (diamond-like) compound such as diamond, silicon carbide, silicon, beryllium oxide and gallium phosphide. In all of these crystals, atoms possess tetrahedral coordination. The binary compounds such as AlN, AlP, B, cubic BN, BP, BeS and GaN may all have  $k$  of greater than 100 W/mK at 300 K.

According to Leifried, Schlömann and Julian, the magnitude of  $k$  for nonmetallic crystals in the temperature range  $T \geq \theta_D$  (where,  $\theta_D$  is the Debye temperature) is given by:

$$k = \frac{B\bar{M}\delta\theta_D^3}{T\gamma^2} \quad (1-45)$$

where  $B$  is constant,  $\bar{M}$  is the average mass of an atom in the crystal,  $\delta$  is average volume occupied by one atom of the crystal and  $\gamma$  is the Grüneisen's constant. The factor  $M\delta\theta_D^3$  is maximized for light mass but strongly bonded crystals like diamond because the  $\theta_D^3$  term dominates the behavior. The  $\gamma^2$  term is smallest for adamantine crystals like Si, G and diamond. The high temperature values of  $\gamma$  are 0.73, 0.45 and 1.3 for these three crystals, respectively. Most crystals have  $1 \leq \gamma \leq 2$ . The adamantine structure also possesses the highest Debye temperatures. These are  $\theta_D \approx 2240$  K for diamond and  $\theta_D \approx 1900$  K for cubic BN.

The value of  $k$  obtained from Eq. (1-45) is valid only for face-centered cubic crystals having  $N=1$  atom per primitive crystallographic unit cell. It means that the phonon dispersion curves have only acoustic branches. For  $N \geq 2$ , there will always be three or more optic branches. As a rule these optic branches have very small group velocities and hence contribute very little to  $k$ .

The four rules for finding a nonmetallic crystal with a high  $k$  is (1) low atomic mass, (2) strong interatomic bonding, (3) simple crystal structure and (4) low

anharmonicity. Conditions (1) and (2) mean a high  $\theta_D$ , condition (3) means low  $N$  and condition (4) means small  $\gamma$ . For aluminum nitride,  $B=3.04 \text{ W/gcm}^2\text{K}^3$ ,  $N=4$ ,  $\bar{M}=20.49 \text{ g}$ ,  $\delta$  (average atomic volume) $= (2.186 \text{ \AA})^3$ . Thermal conductivity of several adamantine crystals is summarized in Table 1-2.  $\bar{M}\delta\theta_D^3$  is the Leifried-Schlomann scaling parameter which is used to order the increasing values for the expected thermal conductivity.

Table 1-2. Thermal conductivity at room temperature for several adamantine crystals [20].

Crystal	$k(\text{W/cmK})$	$\theta_D$ (K)	$\bar{M}\delta\theta_D^3 \times 10^{-2} (\text{g cm K}^3)$
Diamond	20.0	2240	24.07
BN	7.6	1750	12.02
SiC	4.9	1185	7.25
BeO	3.7	1280	4.99
BP	3.6	975	4.39
AlN	3.19	950	3.84
Si	1.56	648	2.07
GaN	1.3	525	1.360
GaP	1.0	444	1.201
AlAs	0.98	417	1.042
InP	0.70	301	0.583
Ge	0.60	374	1.074
ZnO	0.54	419	0.683
GaAs	0.58	347	0.854
AlSb	0.56	289	0.551

## **2. EXPERIMENTAL PROCEDURE**

### **2.1. Sputtering set up**

The aluminum nitride films were fabricated by reactive magnetron sputtering of an aluminum target in the gas mixture of argon and nitrogen. The schematic of the vacuum system is shown in *Figure 2-1*.

Deposition chamber is based on a stainless steel cylinder with a capacity of 50 liters, which equipped with a top and bottom plate sealed with viton o-rings. The chamber utilizes a 6 inch magnetron source and a 5 inch substrate which can be heated.

A turbopump manufactured by Pfeiffer is operated with the support of a Welch mechanical pump.

An MKS baratron pressure gauge with a range of 1 to  $10^{-4}$  Torr was used to monitor chamber pressure during the deposition. An ion gauge was used to measure base pressure of the chamber below  $10^{-4}$  Torr.

The aluminum target was 6 inch and of a purity of 99.999%. The distance between the target and substrate was fixed as 3 inch. A graphite heater which can go up to  $1100^{\circ}\text{C}$  was used. The thermocouple was located just above the heater. The heater is controlled by the Eurotherm controller. The vacuum chamber was evacuated at low  $10^{-6}$  Torr. High purity argon gas (99.999%) controlled by MKS mass flow controllers (MFC) with a maximum flow capacity of 103 sccm was introduced into the vacuum chamber. The gas pressure was measured using a MKS baratron capacitance manometer.

### **2.2. Sputtering experimental parameters and condition**

Two types of power supply were used at the mid frequency range (kHz). The first one is unipolar waveform. AC power (Etna power supply) supply generates a series of 75 kHz DC pulses modulated with 2.5 kHz frequency. The plasma was generated at a constant current mode.

The second one is asymmetric bipolar pulsed DC power supply (ENI, RPG 100). The pulsing frequency can be varied in the range of 50 kHz ~ 250 kHz. The duty cycle which is a ratio of sputtering time to overall time are 60%~98% by changing the reverse pulse time. The frequency and duty cycle are summarized in Table 2-1.

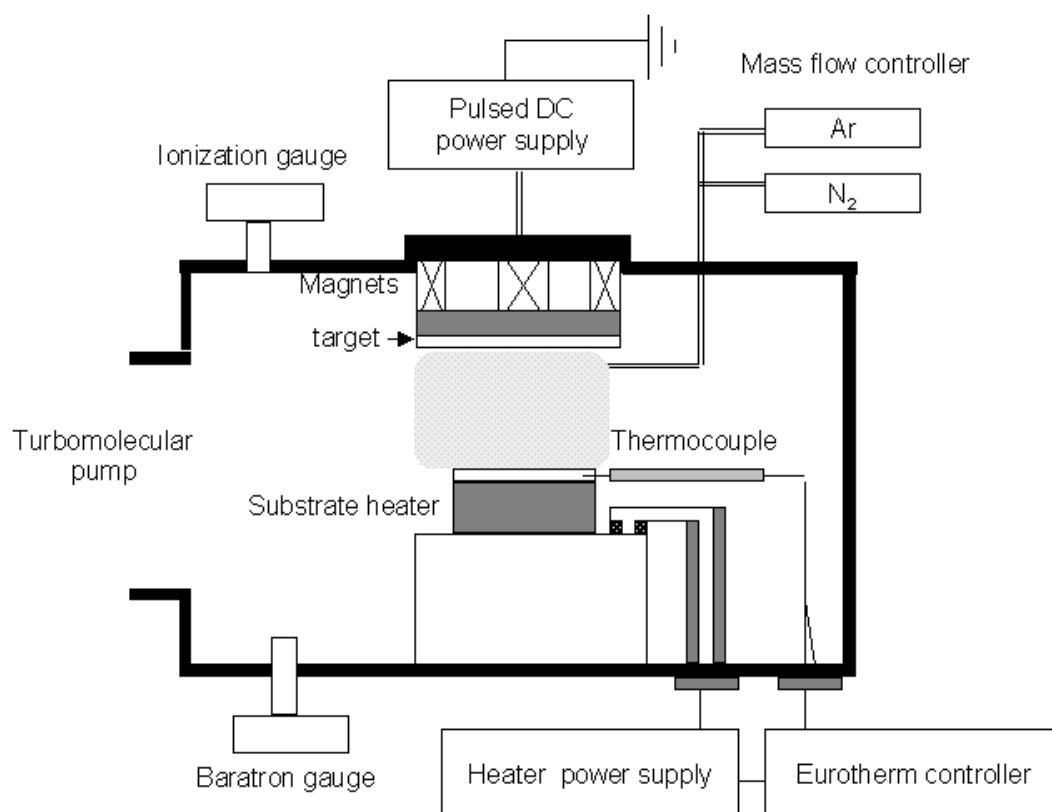


*Figure 2-1.* Schematic of magnetron sputtering system.

---

Table 2-1. Frequency and duty cycle of bipolar asymmetric pulsed DC power supply.

f (kHz)	1/f ( $\mu$ sec)	Min reverse time, $\tau_{rev}$ ( $\mu$ sec)	Max reverse time, $\tau_{rev}$ ( $\mu$ sec)	Max. $\eta$ (%)	Min $\eta$ (%)
50 kHz	20.0	0.496	8.016	98	60
75 kHz	13.3	0.496	5.296	96	60
100 kHz	10.0	0.496	4.016	95	60
250 kHz	40.0	0.496	1.616	88	60

The permanent magnetron is located above the aluminum target. Its magnetic strength is shown in *Figure 2-2*. The target is water-cooled to remove heat generated by ion bombardment and prevent the target from melting.

Degreasing for substrates was carried out by acetone and ethanol in ultrasound base, successively. Si (100), polycrystalline molybdenum and 951 Dupont Green Tape<sup>TM</sup> were used as substrates. The substrates were blown out with dry N<sub>2</sub> gas immediately before inserting them into the vacuum chamber. The vacuum chamber was evacuated to low 10<sup>-6</sup> Torr. High purity argon gas (99.999%) controlled by MKS mass flow controllers (MFC) with maximum flow capacity of 103 sccm was introduced into vacuum chamber. The pressure was measured using a MKS baratron capacitance manometer. Before deposition, the aluminum target was presputtered to remove any contaminations during exposure to the atmosphere with argon gas for 60 min. The shutter was removed after waiting for 5 minutes to reach dynamic equilibrium with argon and nitrogen plasma. The aluminum nitride were deposited on various substrates at sputtering pressure 5~50 mT. The nitrogen partial pressure was obtained by

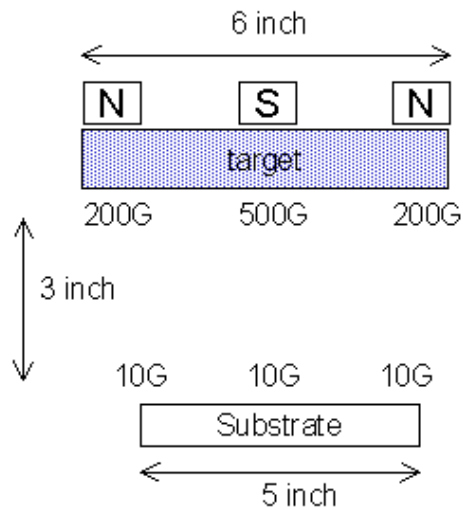


Figure 2-2. Magnetic field at the target and substrate position.

$$P(\%) = \frac{P_{N_2}}{P_{N_2} + P_{Ar}} \quad (2-1)$$

Radio frequency (RF) power having 13.56 MHz, manufactured by RFP products, was applied to induce ion bombardment to substrates. The experimental conditions are summarized in Table 2-2 and 2-3.

## 2.3. Characterization of plasma and thin films

### 2.3.1. Target voltage waveform

Target voltage waveform with respect to time change was obtained at constant current mode 2 A.

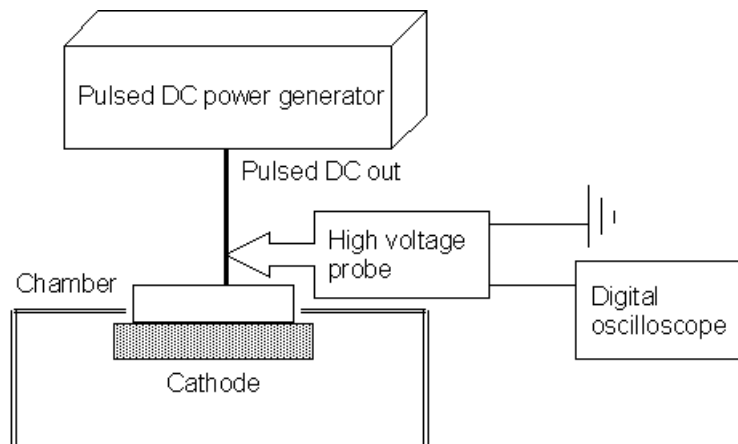


*Figure 2-3.* Target voltage measurement set-up.

---

The high voltage probe having an attenuation ratio of 1:1000 (TEKTRONIX, P6015A Standard HV probe 75 MHz) and digital oscilloscope (TEKTRONIX, TDS210 100 MHz scope) were connected to the system as shown in *Figure 2-3*. The target voltage waveforms directly from the power supply were also recorded without generating plasma.

### **2.3.2. Film thickness**

The thickness measurement of AlN films was performed using a profilometer (Dektak 3030). The samples were partially masked in order to obtain a step height between the silicon wafer and the film. The thickness of aluminum nitride thin films was measured at five different positions and averaged. Standard deviation was calculated from these.

Table 2-2. Experimental conditions for unipolar pulsed DC sputtering.

Presputtering	10 mT of Ar for 60min at 1.0A of constant current mode
Distance between the target and substrates	3"
Substrates	Si (100), Mo, 951 Tape
Sputtering gas pressure	5 mT~ 50 mT
N <sub>2</sub> gas %	60%
Growth temperature	300°C~700°C
Target current	2 A
Deposition time	30min~3hrs

Table 2-3. Experimental conditions for bipolar pulsed DC sputtering.

Presputtering	10 mT of Ar for 60min at 1.0A of constant current mode
Distance between the target and substrates	3"
Substrates	Si (100), Mo
Sputtering gas pressure	5 mT~ 50 mT
N <sub>2</sub> gas %	50%~90%
Growth temperature	300°C~700°C
Target current	1.0 A~2.5 A
Frequency for asymmetric bipolar power	50 kHz~250 kHz
Duty cycle	60%~96% at 75 kHz 60%~95% at 100 kHz 60%~88% at 250 kHz
Deposition time	30min~3hrs

### 2.3.3. X-ray phase analysis

A  $\theta$ - $2\theta$  scan was performed to determine the crystal structure and orientation of the deposited films by x-ray diffractometer with  $\text{CuK}\alpha$  radiation (Rigaku). The  $2\theta$  was varied from  $30^\circ$  to  $70^\circ$ . The step size and count time were  $0.05^\circ$  and 1 sec, respectively.

### 2.3.4. Microstructural analysis-SEM, AFM and TEM

The surface morphologies of the AlN films were observed by field emission scanning electron microscopy (FE-SEM, JEOL 6400f) and atomic force microscopy (AFM, Thermomicroscope). The AFM was operated at contact mode. The UL06C and UL06B tips composed of silicon carbide were used. The scanned areas were  $5\ \mu\text{m} \times 5\ \mu\text{m}$  and  $20\ \mu\text{m} \times 20\ \mu\text{m}$ . The images are analyzed using PSI ProScan Image Processing program. The rms (root mean square) roughness of the film was obtained from AFM images.

The specimen was cleaved for cross section observation. Microstructural analysis was carried out by transmission electron microscope (TEM, Topcon 002B, 200 kV beam and LaB6 cathode). The sample preparation for cross section view was as following. Two pieces of specimen were cut with a diamond saw from the deposited AlN film ( $\sim 10\ \mu\text{m}$ ) on 951 Dupont Green Tape<sup>TM</sup> for preparation of cross-sectional TEM sample. The film surfaces were glued together with M-bond. The backing silicon wafers were bonded to support the sandwiched sample. The M-bond was cured at  $\sim 150^\circ\text{C}$  for  $\sim 10$  hrs. The sandwiched samples were mechanically polished with SiC paper to the thickness of to about  $50\ \mu\text{m}$ . And then the sample was thinned by dimpling. The polishing was performed using  $1\ \mu\text{m}$  alumina paste. The final thinning was performed by ion milling (Gatan, dual ion milling) with 6 keV of  $\text{Ar}^+$  ions at an incidence angle of  $12^\circ$ . The total gun current was kept 1A until perforation occurred. For the plane-view TEM sample, the specimen was cut to small piece and polished the backside of the substrate to the film surface and then thinned in the same way.

### **2.3.5. Electrical properties- C-V, J-V, dielectric constant and loss**

The MIM (metal-insulator-metal) structures were fabricated to measure dielectric properties of the aluminum nitride thin film. Aluminum and molybdenum were used as bottom electrode. For aluminum, the thin aluminum film was deposited on silicon without heating by pulsed dc sputtering with argon plasma. And for a top electrode, aluminum was deposited on aluminum nitride thin films over mask having different dot sizes. The electrode area was obtained from optical microscope observation.

Capacitance-voltage measurement with 1.0V sweeping signal at 100 kHz of the MIM (Al-AlN-Al or Al-AlN-Mo) structure sample was performed using HP 4192A Impedance Analyzer at room temperature.

Keithley 617 programmable electrometer which can apply voltage up to 35 V was used for current-voltage measurement at room temperature. The step size and duration were 0.5 V and 1.0 sec, respectively.

### **2.3.6. Stress analysis by x-ray pattern**

The stress in the film was analyzed by x-ray diffraction method. The AlN powder was used as a standard material in order to eliminate errors due to misalignment of the x-ray diffractometer (Rigaku XX). The AlN powder was ground and packed in the sample holder. The  $2\theta$  was varied from  $30^\circ$  to  $70^\circ$ . The step size and count time was  $0.01^\circ$  and 5 sec.

### **2.3.7. Photoluminescence spectrum**

Photoluminescence measurements were carried out in air at room temperature with the excitation photon energy having wavelength between 325 nm and 700 nm. He-Cd laser having 325 nm (Omnichrome Series 74) was used. The PL emissions were collected along the direction of the surface normal and dispersed through a 1/2 m monochromator (Jorrel Ash Model #5). The PL spectra were recorded in the wavelength range from 300 to 700 nm.

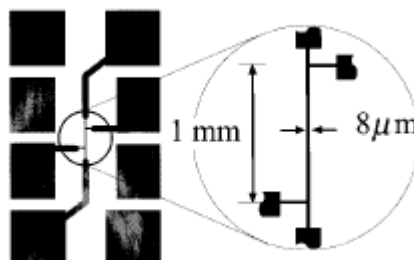


*Figure 2-4.* Pattern for the heater/thermometer line and contact pads. The width of the heater/thermometer line  $w$  is typically  $8\ \mu\text{m}$  and the length  $l$  is  $1.0\ \text{mm}$ .

---

### 2.3.8. Thermal conductivity

Thermal conductivities of the aluminum nitride films were measured by thermal mirage technique and  $3\omega$  method. For  $3\omega$  method, Au/Cr metal line was deposited on aluminum nitride thin film by e-beam evaporation. The heater/thermometer line is patterned using photolithography. The metal line pattern is shown in *Figure 2-4*.

### 2.3.9. Langmuir probe measurement

The Langmuir probe composed with tungsten wire was inserted into the vacuum chamber. The tip is covered with glass house for insulation as shown in *Figure 2-5*. Cylindrical probe was used for a double and single probe measurements.

The diameter and length of the tungsten probe are  $0.508\ \text{mm}$  and  $6\ \text{mm}$ , respectively. Two identical probes separated by  $6\ \text{mm}$  were used for double probe measurement. The probe was covered by glass bead for electrical insulation. The copper layer wrapped the tungsten probe and insulator to remove any external interference. The copper shield is connected to ground.

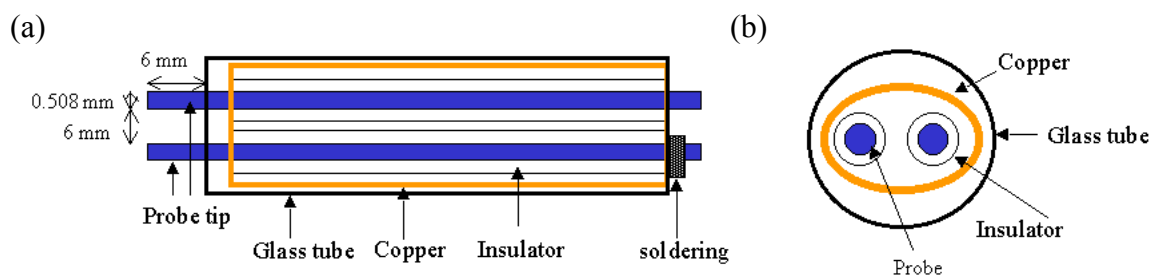


*Figure 2-5.* Double probe head (a) side view and (b) cross section view.

---

The voltage was applied to the probe by variable power supply (Kempco power supply). The voltage was varied in the range  $-100\text{V}$  and  $+100\text{V}$ . The probe current and voltage were measured by using multimeter (Fluke 85 III) and Keithley (177 microvolt DMM). The probe current with voltage change was measured at substrate position. The detailed set-up is shown in *Figure 2-6*.

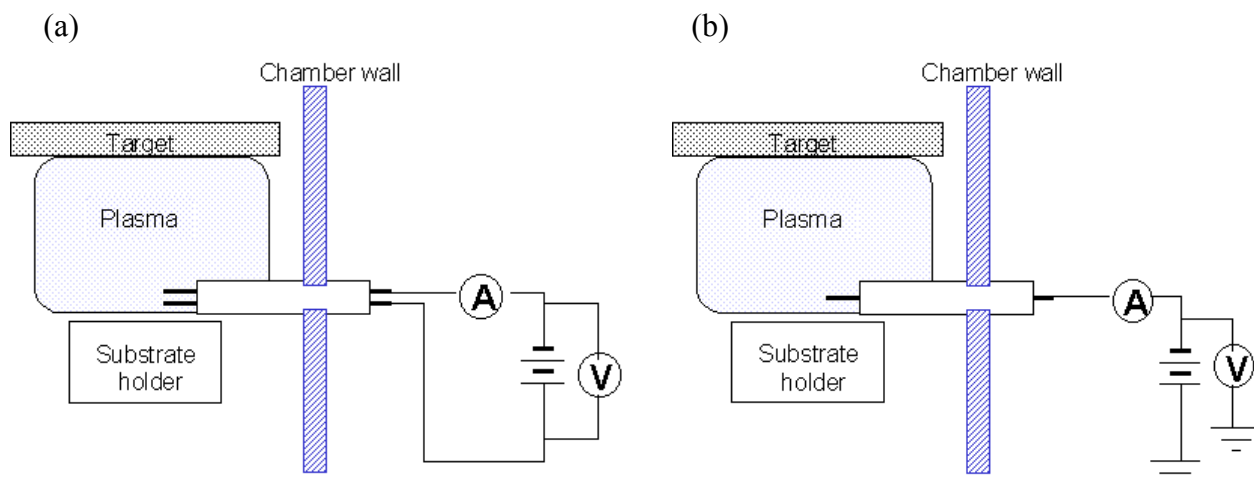


Figure 2-6. Langmuir probe measurement set-up (a) double probe and (b) single probe

---

### 3. Bipolar Asymmetric Pulsed DC Sputtering of AlN Thin Films

#### 3.1. Wave Form of Pulsed DC Power

Target voltage waveforms with respect to time were obtained by using a high voltage probe and a digital oscilloscope. Plasma was generated at a constant current mode (2.0 A). Duty cycle  $\eta$  is defined as a ratio of negative pulse time  $\tau_{on}$  to total time, which is the inverse of the frequency as following

$$\eta = \frac{\tau_{on}}{\tau_{on} + \tau_{rev}} = \frac{1/f - \tau_{rev}}{1/f} \quad (3-1)$$

where  $\eta$  is the duty cycle,  $f$  is the frequency,  $\tau_{on}$  is the negative pulse time and  $\tau_{rev}$  is the positive pulse (reverse pulse time) time. The duty cycle can be varied by changing the reverse pulse time. The minimum reverse pulse time is 496 nsec for all frequencies, corresponding to 60% of duty cycle. The maximum reverse pulse time is dependent on the pulsing frequency as shown in Table 2-1.

The target voltage waveforms for 75 kHz, 100 kHz and 250 kHz are shown in *Figures 3-1~3-3*. The duty cycle was changed from 60% to a maximum value 96% for 75 kHz, 95% for 100 kHz and 88% for 250 kHz. Pulsed dc power should generate a rectangular waveform. However, in real there are overshoots in the negative pulse and fast ringing on the positive pulse when the polarity of voltage changes. This oscillatory feature comes not from the plasma characteristics but from the pulsed DC power supply since the voltage waveform directly measured from power supply (without connecting to plasma) have the same waveform. High voltage above +100 V was observed when the target voltage was changed from negative to positive as shown in *Figures 3-1~3-3*. After fast ringing (MHz range), the reverse voltage was flattened and +37 V for 60% and 80% duty cycles. The flattened voltage region couldn't be observed due to short reverse pulse time as shown in *Figure 3-1 (c)* (96%  $\eta$  at 75 kHz), *Figure 3-2 (c)* (95%  $\eta$  at 100 kHz) and *Figure 3-3 (c)* (88%  $\eta$  at 250 kHz). The target voltage reaches up to -400 V on polarity reversal and then becomes flattened to around -300 V.

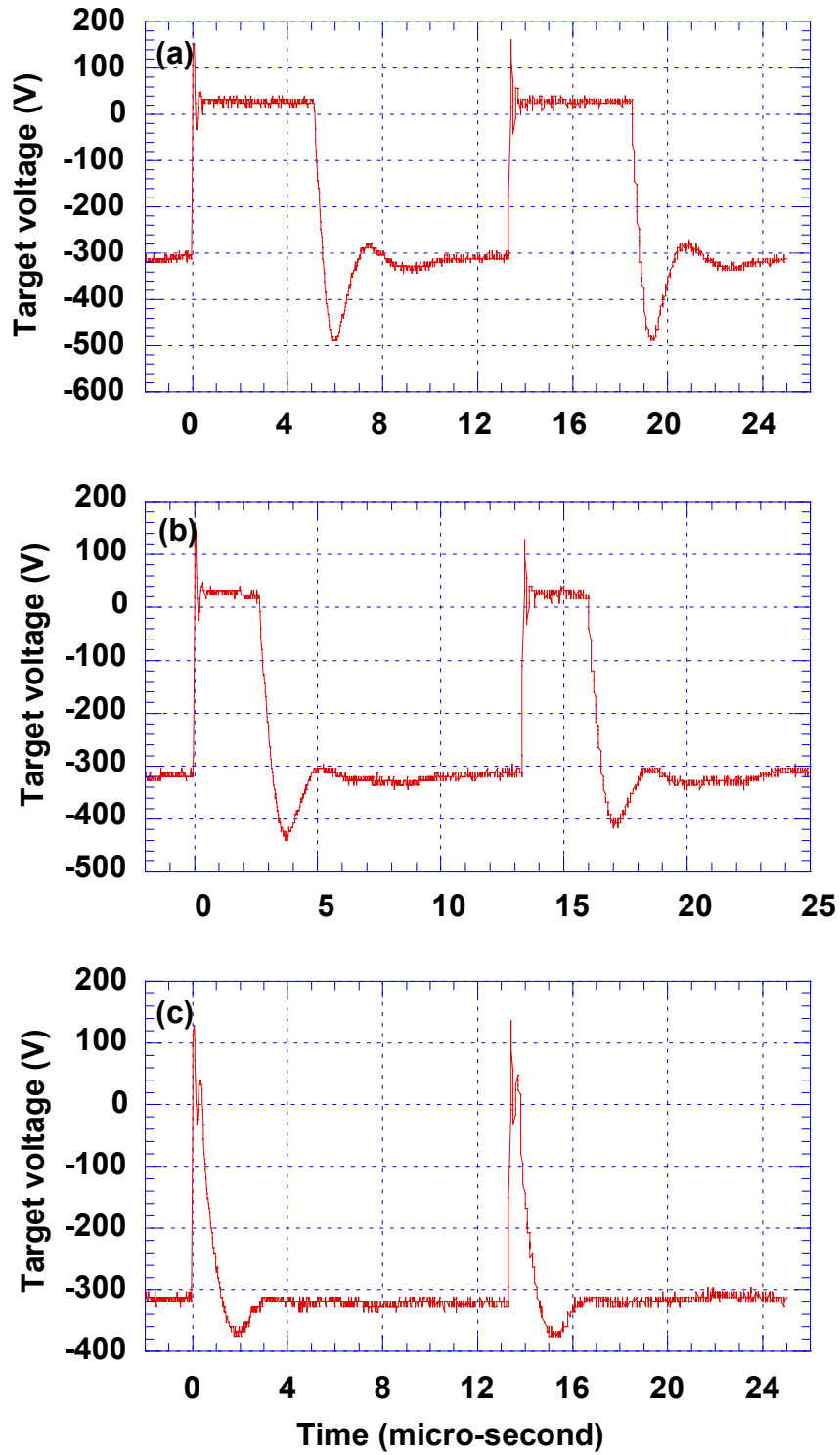


Figure 3-1. Target voltage waveforms at 75 kHz with (a) 60%, (b) 80% and (c) 96% of duty cycle (28 mT of sputtering pressure, 70% of N<sub>2</sub>, 2 A of target current).

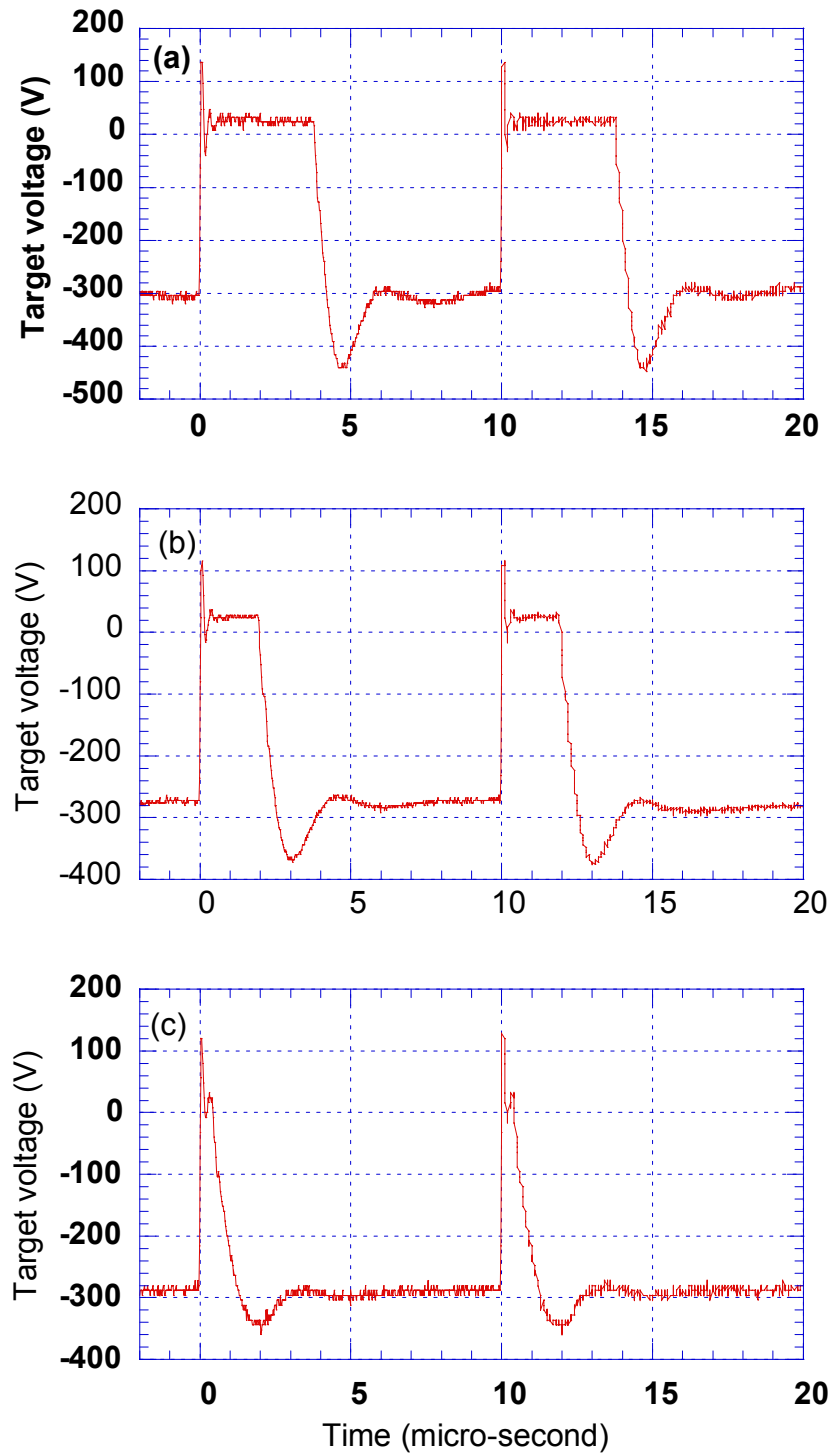


Figure 3-2. Target voltage waveforms at 100 kHz with of (a) 60%, (b) 80% and (c) 95% of duty cycle (28 mT of sputtering pressure, 70% of N<sub>2</sub>, 2 A of target current).

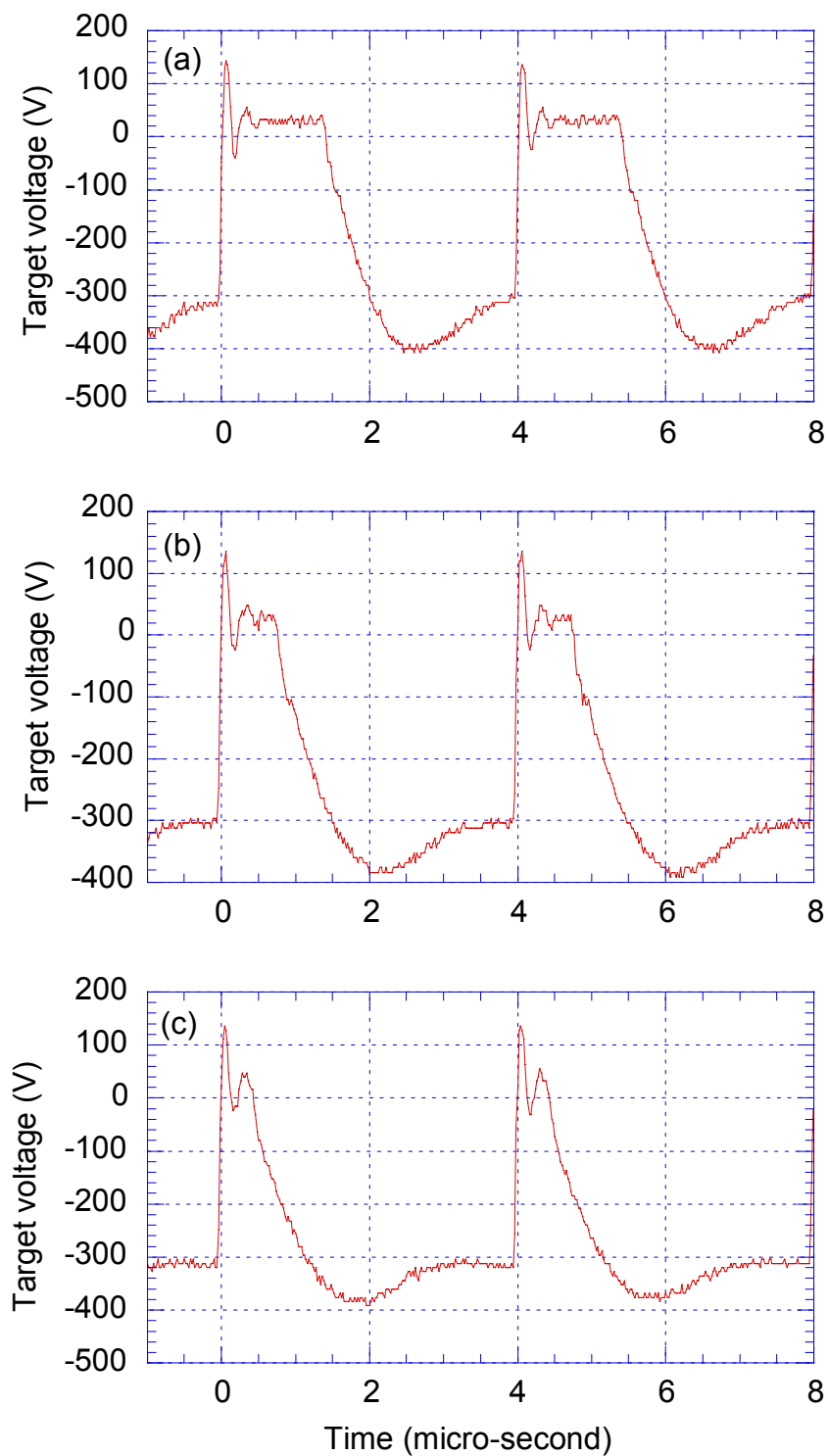


Figure 3-3. Target voltage waveforms at 250 kHz with (a) 60%, (b) 80% and (c) 88% of duty cycle (28 mT of sputtering pressure, 70% of  $N_2$ , 2 A of target current).

Since the target voltage and target current on the panel in the power supply are average values, it is important to obtain the exact target voltage waveform with respect to time. It is known [30] that this oscillatory feature was a function of the power supply and not associated with the intrinsic plasma dynamics. The effect of this overshoot in the negative pulse is still being investigated. However it is known that these oscillatory voltage will produce much more energetic particles during the pulse cycle [32].

### **3.2. Dependence of Sputtering Parameters on Crystal Orientation and Microstructures**

It is important to be able to control the crystal orientation and crystalline quality of the film for many applications. Properties of films are strongly dependent on deposition parameters such as target power, growth temperature, sputtering pressure and gas compositions [61-67]. The effects of the deposition parameters on properties of aluminum nitride thin films were investigated in DC [68,69] and RF reactive sputtering [70-75]. However, the effects of deposition parameters on the properties of films in pulsed dc sputtering have not been studied much. It is not fully understood how the deposition conditions affect the crystal orientation and microstructure of the deposited film. In this chapter, the effects of deposition conditions on the crystal orientation and microstructure of the aluminum nitride will be investigated. The deposition variables include pulsing frequency and duty cycle as well as sputtering power, sputtering pressure and nitrogen content.

#### **3.2.1. Sputtering power change**

The effect of sputtering power on the crystal orientation of aluminum nitride was investigated. The XRD results of the aluminum nitride thin films on Si (100) with a change in target current are shown in *Figure 3-4*. All peaks are corresponding to the wurtzite hexagonal phase of aluminum nitride. The aluminum nitride thin film grown at a low target current of 1.0 A (*Figure 3-4 (a)*) had low intensities of (100) and (110) peaks.

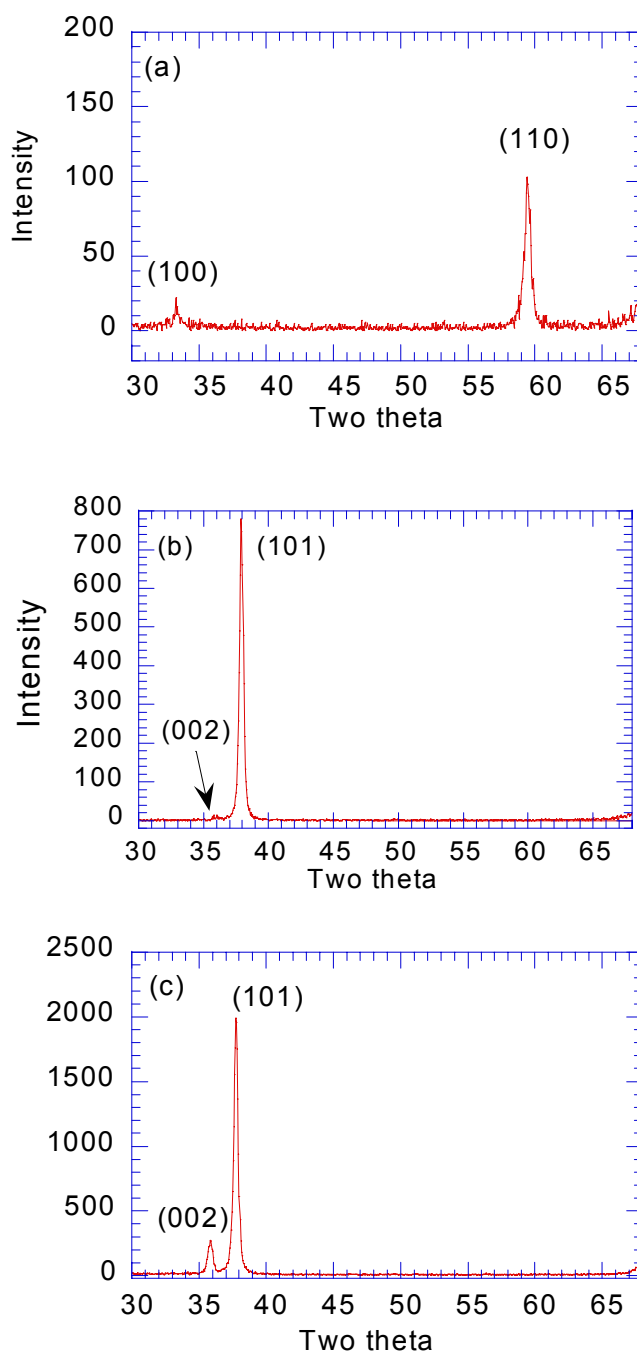


*Figure 3-4.* XRD results of the aluminum nitride thin films on Si (100) prepared at (a) 1.0 A, (b) 1.25 A, (c) 1.5 A, (d) 2.0 A and (e) 2.5 A of target current (500°C of growth temperature, 28 mT of sputtering pressure, 70% of nitrogen, 100 kHz of frequency, 80% of duty cycle).

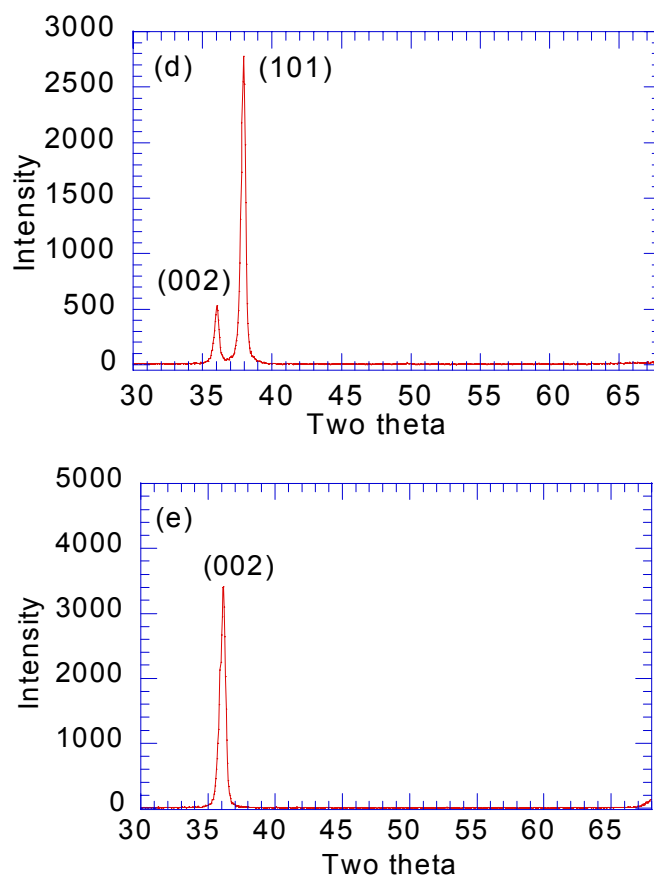


*Figure 3-4.* XRD results of the aluminum nitride thin films on Si (100) prepared at (a) 1.0 A, (b) 1.25 A, (c) 1.5 A, (d) 2.0 A and (e) 2.5 A of target current (500°C of growth temperature, 28 mT of sputtering pressure, 70% of nitrogen, 100 kHz of frequency, 80% of duty cycle).

---

The (101) peak with weak (002) peak appeared as the target current increased up to 2.0 A (*Figure 3-4 (b)-(d)*). c-axis oriented AlN thin film was obtained at 2.5 A of the target current (*Figure 3-4 (e)*).

The basal plane in the hexagonal structure has the lowest surface energy and the maximum atomic density. More energetic atoms from the target are ejected at higher target current and thus adatoms on the substrate have a greater chance to move to the lowest energy state [72]. However, at the low target current of 1.0 A, the energy of adatoms is too low to form good crystalline films. Ohuchi et al. [66] reported different results of sputtering power on the orientation of AlN films prepared by RF magnetron sputtering. The (002) orientation of AlN films was obtained at lower RF powers (100 W~300 W). The (101), (102) and (103) orientation appeared when the RF power increased to 300 W~900 W. The orientation variation of the AlN films was thought to be related with deposition rate. It may be explained as the following. At a low RF power, adatoms on the surface have a higher probability of rearrangement and a longer time to form a low-energy configuration such as the close-packed (001) atom plane. As the rate increases, however, the adatoms have a shorter time to be rearranged into low energy configurations before the next layer of arriving species determines their atom position. Cheng et al. [74] also investigated the effect of target power on the crystal orientation of aluminum nitride films by RF magnetron sputtering. They changed target power from 150 W to 350 W at the sputtering pressure of 30 mT. No crystalline orientation of AlN was observed at the low target power (150 W~200 W) due to the insufficient energy for forming crystalline structures. The (002) preferred orientation was obtained at the high target power (250 W~350 W).

The dependence of deposition rates of the aluminum nitride thin films on target current is shown in *Figure 3-5*. The deposition rate increases with target current. The number of accelerating ions towards the target increases with target power. At low target currents, the number of energetic aluminum atoms from the target is relatively low and results in low deposition rates. The deposition rate can be correlated with the degree of crystal orientation. The cross section photographs are shown in *Figure 3-6*. All films show a columnar structure. The columnar structure seen in the aluminum nitride thin films is typical as reported in other sputtered AlN films [62, 73-75]. The structure forms when a solid is generated from a vapor flux which arrives perpendicular to the substrate with lesser movement of adatoms [47].

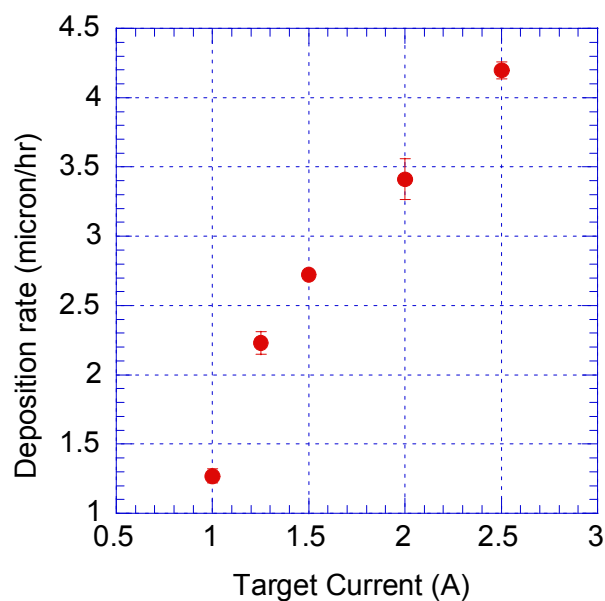


*Figure 3-5.* Deposition rates of the aluminum nitride thin films on Si (100) with target current variations (500°C of growth temperature, 28 mT of sputtering pressure, 70% of nitrogen, 100 kHz of frequency, 80% of duty cycle).

---

The development of the columnar structure is very sluggish at low target current of 1.0 A (*Figure 3-6 (a)*). The columnar growth becomes more apparent as the target current increases up to 2.0 A. At these target current ranges (1.25 A~2.0 A), however, the columns are not continuous and their growth direction is quite random. The aluminum nitride thin film grown at 2.5 A (*Figure 3-6 (e)*) showed well-developed columns. These films have homogeneous structure along the thickness. These aluminum nitride thin films belong to Zone 1, where very small grains grow out of the primary nuclei and proceed to the top of the film.

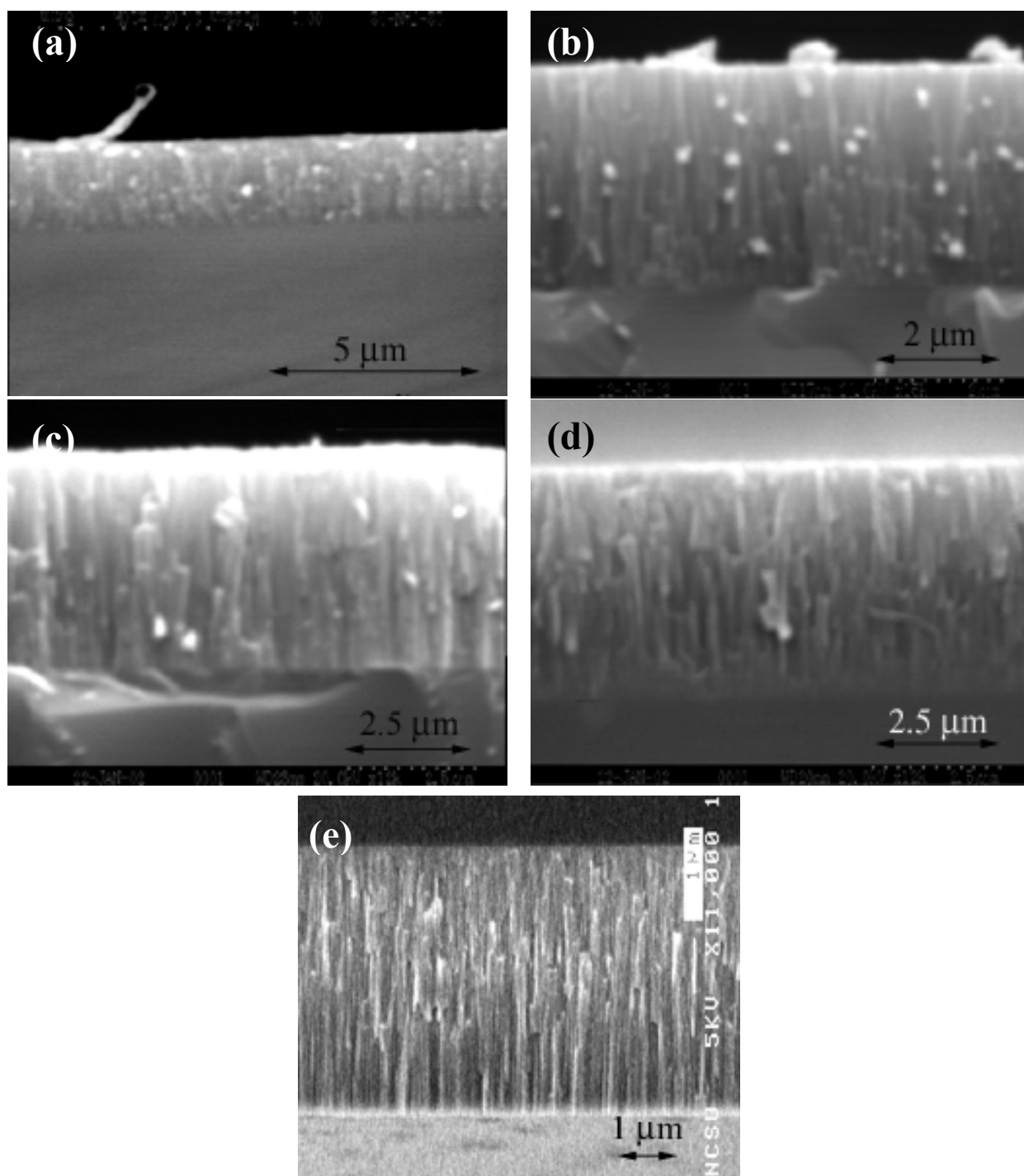


*Figure 3-6.* Cross section views of the aluminum nitride thin films on Si (100) grown at (a) 1.0A, (b) 1.25A, (c) 1.5A, (d) 2.0A and (e) 2.5A of target current (500°C of growth temperature, 28 mT of sputtering pressure, 70% of nitrogen, 100 kHz of frequency, 80% of duty cycle).

The AFM images of the deposited films are shown in *Figure 3-7*. The scanned area was  $5\ \mu\text{m} \times 5\ \mu\text{m}$ . The elongated grains and some pores are observed at the low target current of 1.0A (*Figure 3-7 (a)*). As the target current increases, the grains became round. Very small grains with some nodular defects were observed for the aluminum nitride thin films grown at the target current of 2.5 A (*Figure 3-7 (d)*). The nodular defects have been usually observed at high deposition rates. Surface roughness of thin film is important for some applications including SAW (surface acoustic wave) devices. The rough surface will impede wave transmission and increase propagation loss. The root mean square (rms) surface roughness  $R_a$  of the aluminum nitride films was obtained from the AFM images (*Figure 3-7*). Very smooth surface was obtained for the film grown at the target current of 1.0A. For the films grown in the range of 1.25 A and 2.0 A had very rough surface with  $R_a \sim 22\ \text{nm}$  while the film grown at 2.5 A had smooth surface with  $R_a \sim 8\ \text{nm}$  in *Figure 3-8*. This indicates that the surface morphologies and roughness of the deposited film are related with crystal orientation. For the (002) orientation, surface morphology is least pronounced as shown in *Figure 3-7 (d)*. This is because the close-packed basal plane shows very little microcrystalline facetings. For the (102) and (101) orientation, the (102) and (101) planes are grown parallel to the substrate and terminated at the surface. It shows a high degree of microcrystalline faceting. The aluminum nitride thin films having mixed orientations with (002) and (101) planes had rough surface. Ohuchi et al. [66] observed similar results with these observations.

### **3.2.2. Growth temperature change**

The effect of growth temperature on crystal orientation was investigated. The XRD results of the aluminum nitride films with growth temperature are shown in *Figure 3-9*. All other deposition conditions were kept constant: 2 A of target current, 28 mT of sputtering pressure, 70%  $\text{N}_2$ , 100 kHz of frequency and 80% of duty cycle. Only the (101) peak of hexagonal AlN was observed at the temperature of  $300^\circ\text{C}$  (*Figure 3-9 (a)*).

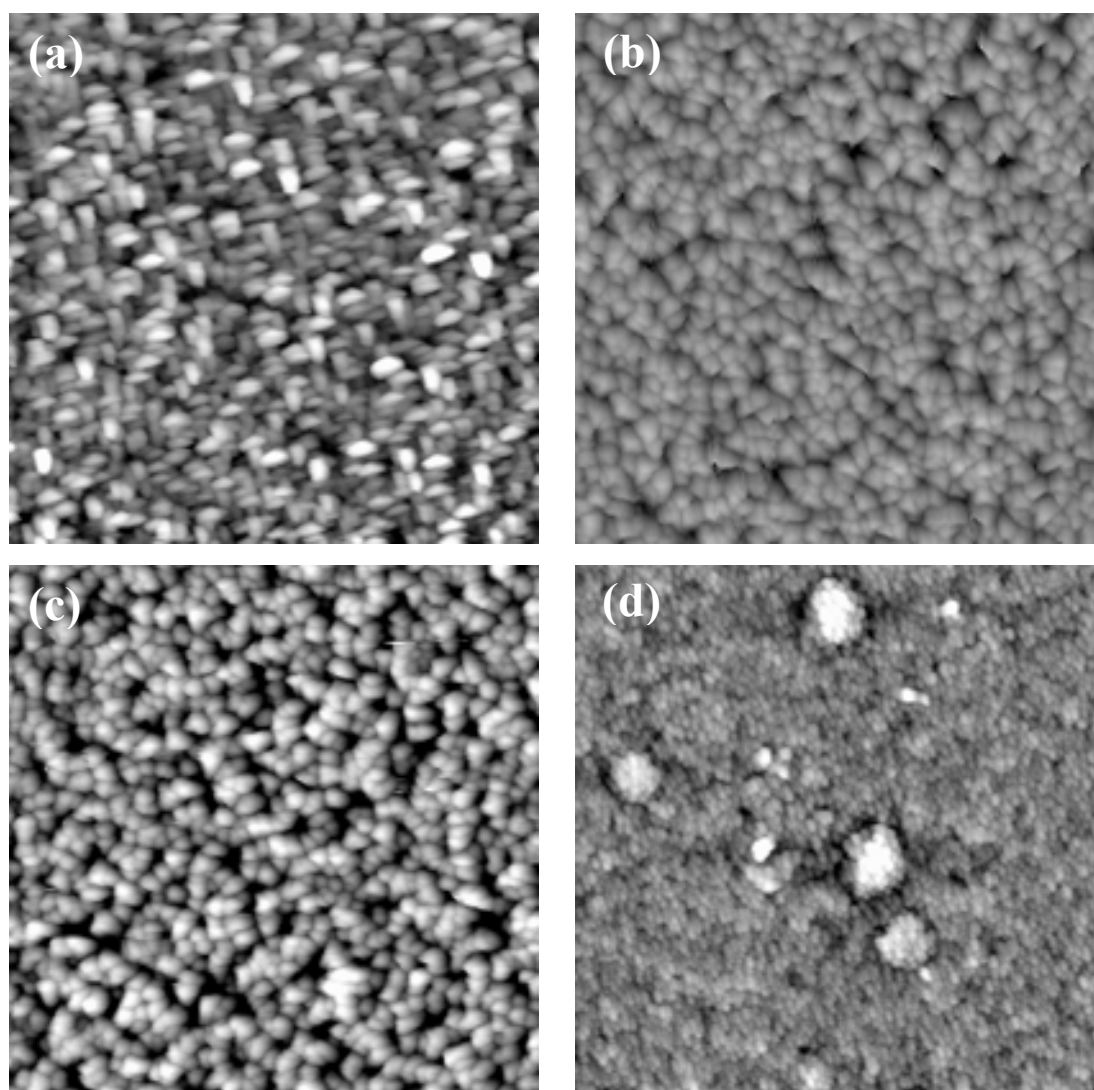


*Figure 3-7.* AFM images of the aluminum nitride thin films on Si (100) grown at (a) 1.0 A, (b) 1.5 A, (c) 2.0 A and (d) 2.5 A of target current (500°C of growth temperature, 28 mT of sputtering pressure, 70% of nitrogen, 100 kHz of frequency, 80% of duty cycle). Scan area is  $5\ \mu\text{m} \times 5\ \mu\text{m}$ .

---

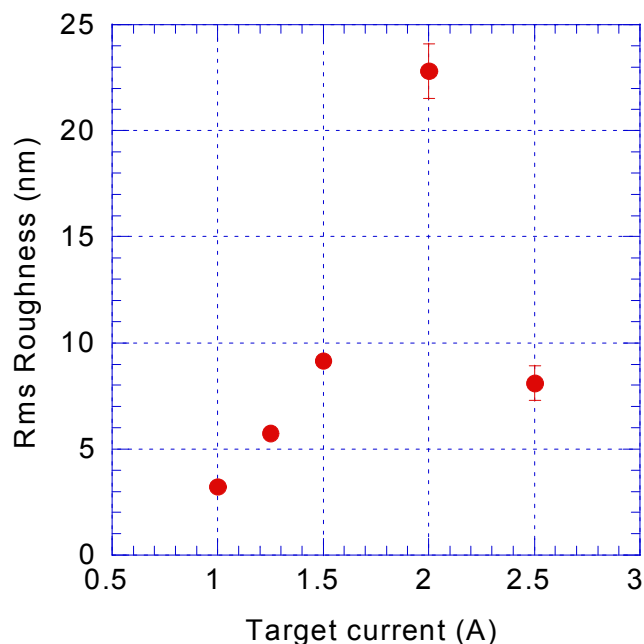


*Figure 3-8.* Rms surface roughness of the AlN films grown on Si (100) with variations of target currents (500°C of growth temperature, 28 mT of sputtering pressure, 70% of nitrogen, 100 kHz of frequency, 80% of duty cycle).

---

The (002) peak began to appear as growth temperature increased to 500°C (*Figure 3-9 (b)*). The c-axis-oriented AlN film was obtained at 700°C (*Figure 3-9 (c)*). Similarly to other deposition techniques such as MBE, CVD, laser ablation and VPE, the raised growth temperature is expected to increase the mobility of adatoms on the substrate during growth, although the kinetics of arriving species is different. Substrate temperature controls the mobility of the adsorbed atoms and the resulting structural development of the films. A surface with low adatom mobility tends to form crystallite structures with a low density. With increasing the growth temperature, the mobility of adatoms increases, leading to the lowest energy state with the (002) orientation.

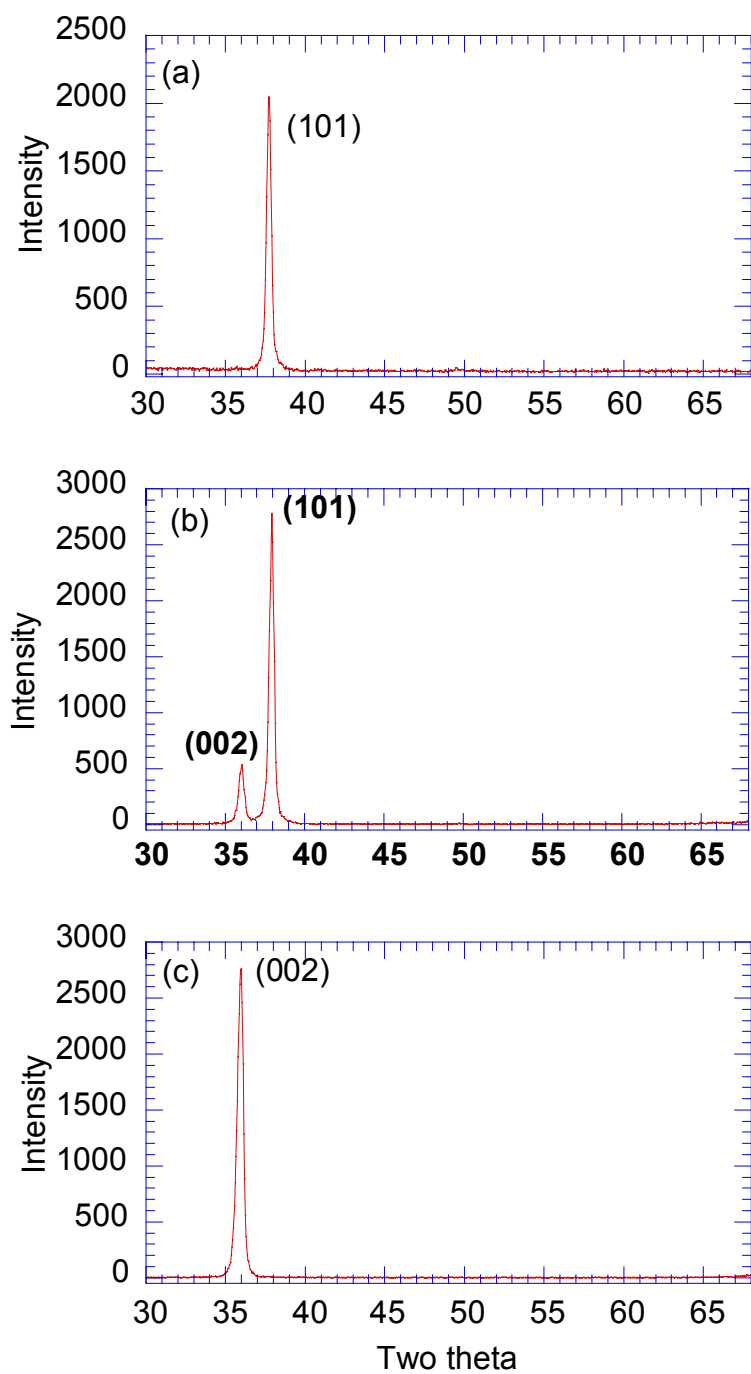
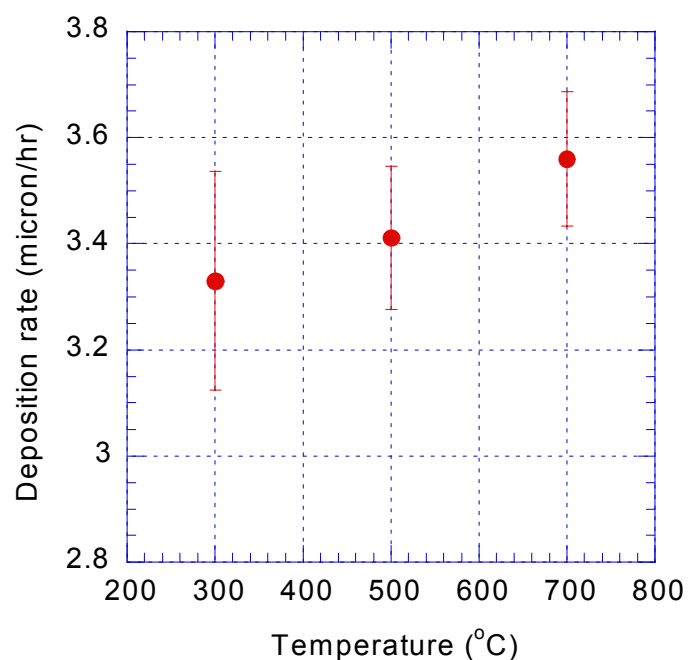


Figure 3-9. XRD results of the aluminum nitride thin films on Si (100) grown at (a) 300°C, (b) 500°C and (c) 700°C (28 mT of sputtering pressure, 70% of nitrogen, 2 A of target current, 100 kHz of frequency, 80% of duty cycle).



*Figure 3-10.* Deposition rates of the aluminum nitride thin films on Si (100) with growth temperature change (28 mT of sputtering pressure, 70% of nitrogen, 2 A of target current, 100 kHz of frequency, 80% of duty cycle).

---

Cheng et al. [74] reported that the crystal quality of the aluminum nitride thin films prepared by RF sputtering was improved by increasing substrate temperature from 150°C to 350°C with the increased mobility of adatoms. It should be mentioned that the growth temperature is not usually same with substrate temperature. Since thermocouple detects the temperature at the position just above the heating element, the actual substrate temperature is lower than the temperature reading. The difference between the real substrate temperature and the thermocouple reading may increase at higher temperatures.

The deposition rates of the aluminum nitride thin films are shown in *Figure 3-10*. The deposition rate increases slightly with the growth temperature. The sticking coefficient of the aluminum nitride on silicon substrate seems not to change significantly within this temperature range since the deposition rate of thin films is related to the sticking coefficient of adatoms on substrate.

*Figure 3-11* shows the microstructures of the aluminum nitride thin films with the change of growth temperature. All films have a columnar structure. The aluminum nitride thin films grown at different growth temperatures showed distinctly different surface morphology. At the low temperature of 300°C (*Figure 3-11 (b)*), the surface morphology of the film couldn't be observed clearly by FE-SEM even at high magnifications. The surface of the aluminum nitride thin film grown at 500°C (*Figure 3-11 (d)*) is faceting (triangular) while grains become round as growth temperature increases to 700°C (*Figure 3-11 (f)*). The surface morphology of the film grown at 700°C are similar with those grown at the target current of 2.5 A having nodular defects (*Figure 7 (d)*). The rms surface roughness  $R_a$  obtained from the AFM images is shown in *Figure 3-12*. The surface roughness of the AlN film showed a maximum when the growth temperature was 500°C.

### **3.2.3. Sputtering gas pressure change**

The effect of sputtering pressure on crystal orientation and microstructure of the aluminum nitride films were examined. *Figure 3-13* shows the XRD results of the aluminum nitride thin films prepared at a frequency of 100 kHz and a duty cycle of 80%. The sputtering pressure changed from 5 mT to 28 mT. The nitrogen content was kept to 70% of total pressure and the target current was 2 A. Very weak (002), (102) and (103) peaks appeared at the low pressure of 5 mT (*Figure 3-14 (a)*). The AlN film grown with 10 mT of sputtering pressure showed strong c-axis orientation (*Figure 3-13 (b)*). Further increase in sputtering pressure caused the (101) peak of the AlN to grow while the intensity of (002) peak decreased (*Figure 3-13 (c)*).

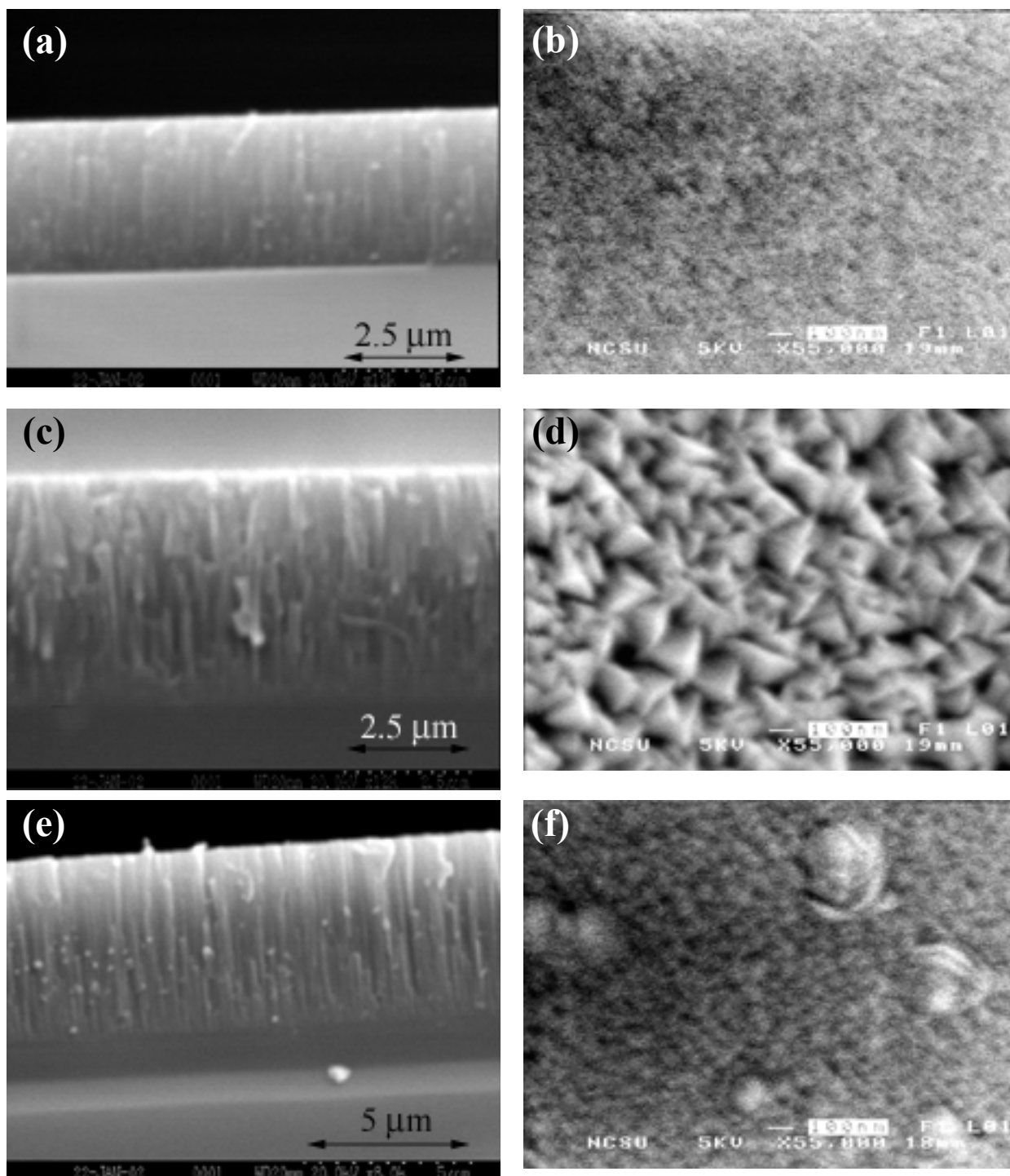
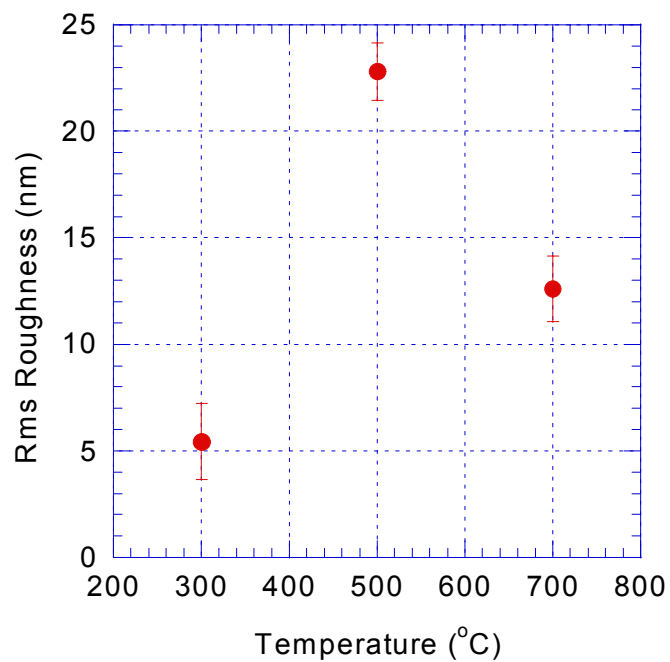


Figure 3-11. Cross section views and surface morphologies of the aluminum nitride thin films on Si (100) grown at (a) and (b) 300°C, (c) and (d) 500°C, (e) and (f) 700°C (28 mT of sputtering pressure, 70% of nitrogen, 2 A of target current, 100 kHz of frequency, 80% of duty cycle).



*Figure 3-12.* Rms surface roughness of the aluminum nitride thin films on Si (100) with growth temperature change (28 mT of sputtering pressure, 70% of nitrogen, 2 A of target current, 100 kHz of frequency, 80% of duty cycle).

---

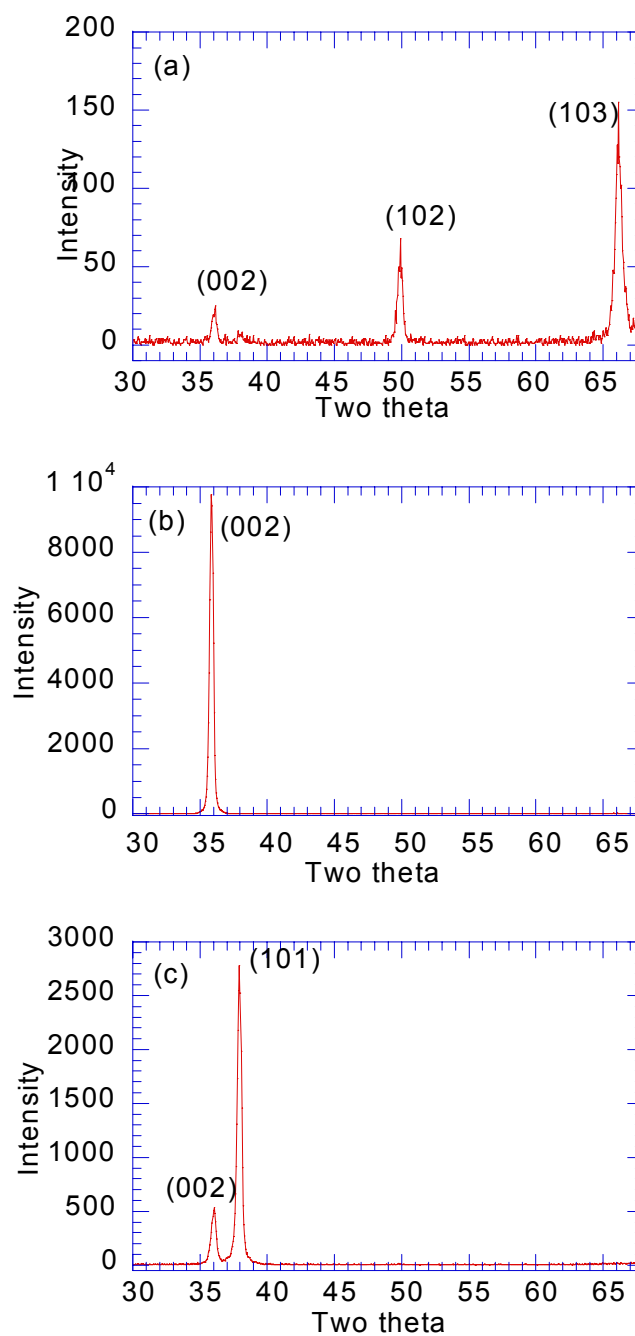


Figure 3-13. XRD results of the aluminum nitride thin films on Si (100) prepared with (a) 5 mT, (b) 10 mT, (c) 28 mT of sputtering pressures at 100 kHz of frequency and 80% of duty cycle (500°C of growth temperature, 2 A of target current, 70% of nitrogen).

The sputtering pressure effect was also investigated at a different frequency/duty cycle, 250 kHz/60% duty cycle. At the low sputtering pressure of 5 mT (*Figure 3-14 (a)*), very weak (002), (101), (102) and (103) peaks of the AlN were observed similar with the XRD of the aluminum nitride thin film grown with 5 mT at the 100 kHz /80% duty cycle. The (002) peak increased while the (102) and (103) peaks decreased when the sputtering pressure increased to 10 mT (*Figure 3-14 (b)*). At the 28 mT of sputtering pressure (*Figure 3-14 (c)*), the (102) and (103) peaks disappeared completely.

Many studies [62,63,69,72,76] have been reported on the effect of sputtering pressure on crystal orientation of aluminum nitride films prepared by DC or RF magnetron sputtering. The (002) orientation was obtained at low sputtering pressures, while the (100), (101) and (102) orientations at higher pressures. This dependence of crystal orientation on sputtering pressure may be explained by the kinetic energy of sputtered atoms. Ideally, sputtering pressure should be low so that material can easily travel through vacuum from sputtering target to substrate. Since plasma is maintained by collisions between electrons and neutral gas atoms, a substantial pressure is required to exist the plasma. Sputtered atoms travel in a line-of-sight mode at low sputtering pressures, in which the energy imparted at the substrate may cause damage of the growing films as evident in the low intensities of several peaks in XRD (*Figure 3-13 (a)* and *Figure 3-14 (a)*) [76].

Deposition rates of the aluminum nitride thin films grown at 100 kHz and 250 kHz are shown in *Figure 3-15*. The deposition rate decreases with sputtering pressure for 100 kHz/80% duty cycle while it shows a maximum value at 10 mT for 250 kHz/60% duty cycle. Usually higher deposition rates are obtained at low pressures due to fewer collisions and scattering between the sputtered gas molecules.

The effects of sputtering pressure on microstructure of the AlN film are shown *Figures 3-16* and *17*. *Figure 3-16* is corresponding to the AlN films grown at 100 kHz/80% duty cycle.

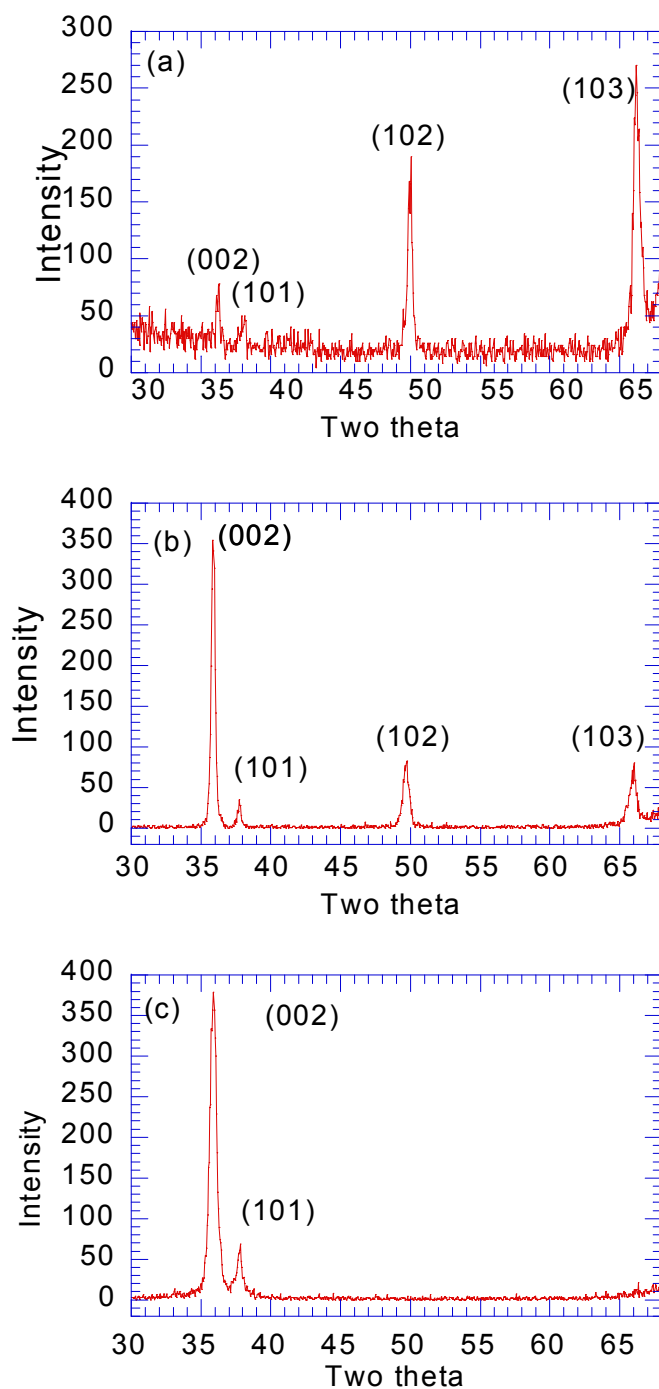
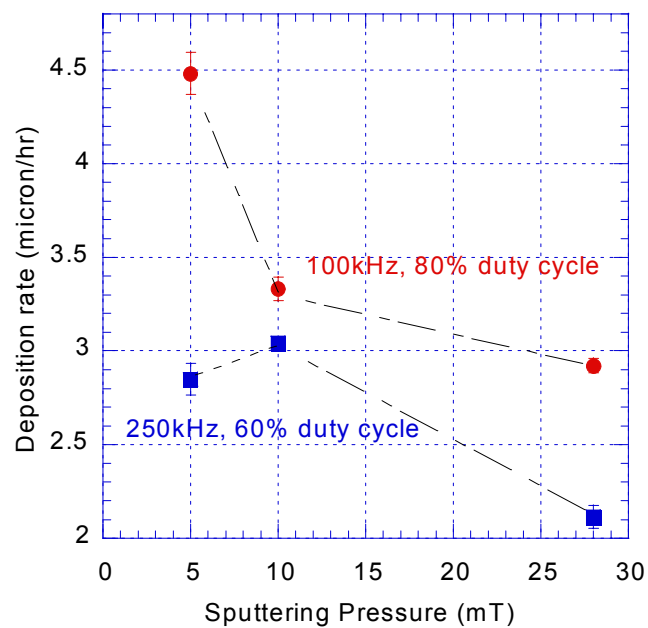
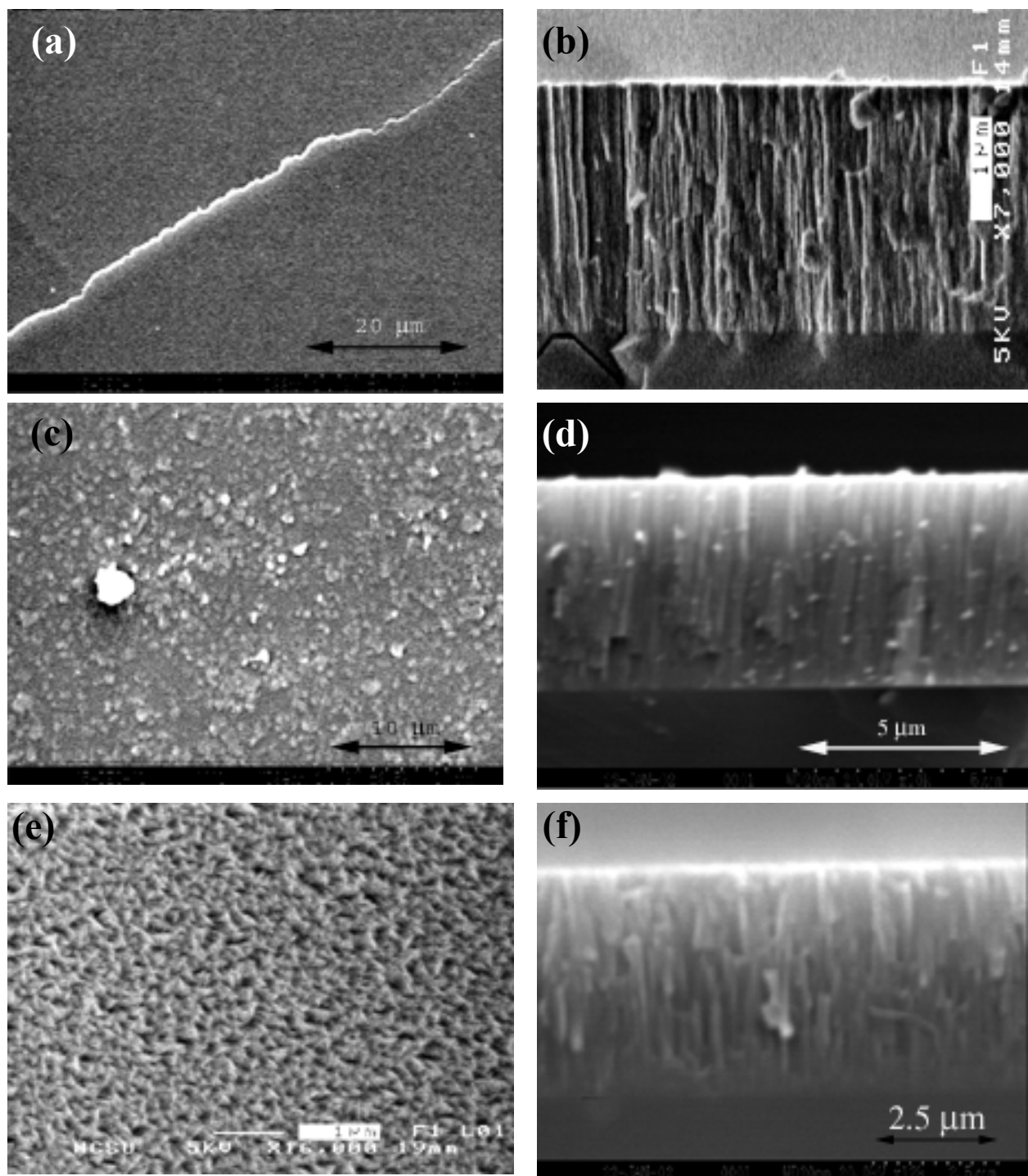


Figure 3-14. XRD results of the aluminum nitride thin films on Si (100) prepared with (a) 5 mT, (b) 10 mT, (c) 28 mT of sputtering pressures at 250 kHz of frequency and 60% of duty cycle (500°C of growth temperature, 2 A of target current, 70% of nitrogen).



*Figure 3-15.* Deposition rates of the aluminum nitride thin films on Si(100) with change in sputtering pressure (500°C of growth temperature, 2 A of target current, 70% of nitrogen).

---



*Figure 3-16.* Surface morphologies and cross section of the aluminum nitride thin films grown with (a) and (b) 5 mT, (c) and (d) 10 mT, (e) and (f) 28 mT of sputtering pressure at 100 kHz and 80% of duty cycle (500°C of growth temperature, 2 A of target current, 70% of nitrogen).

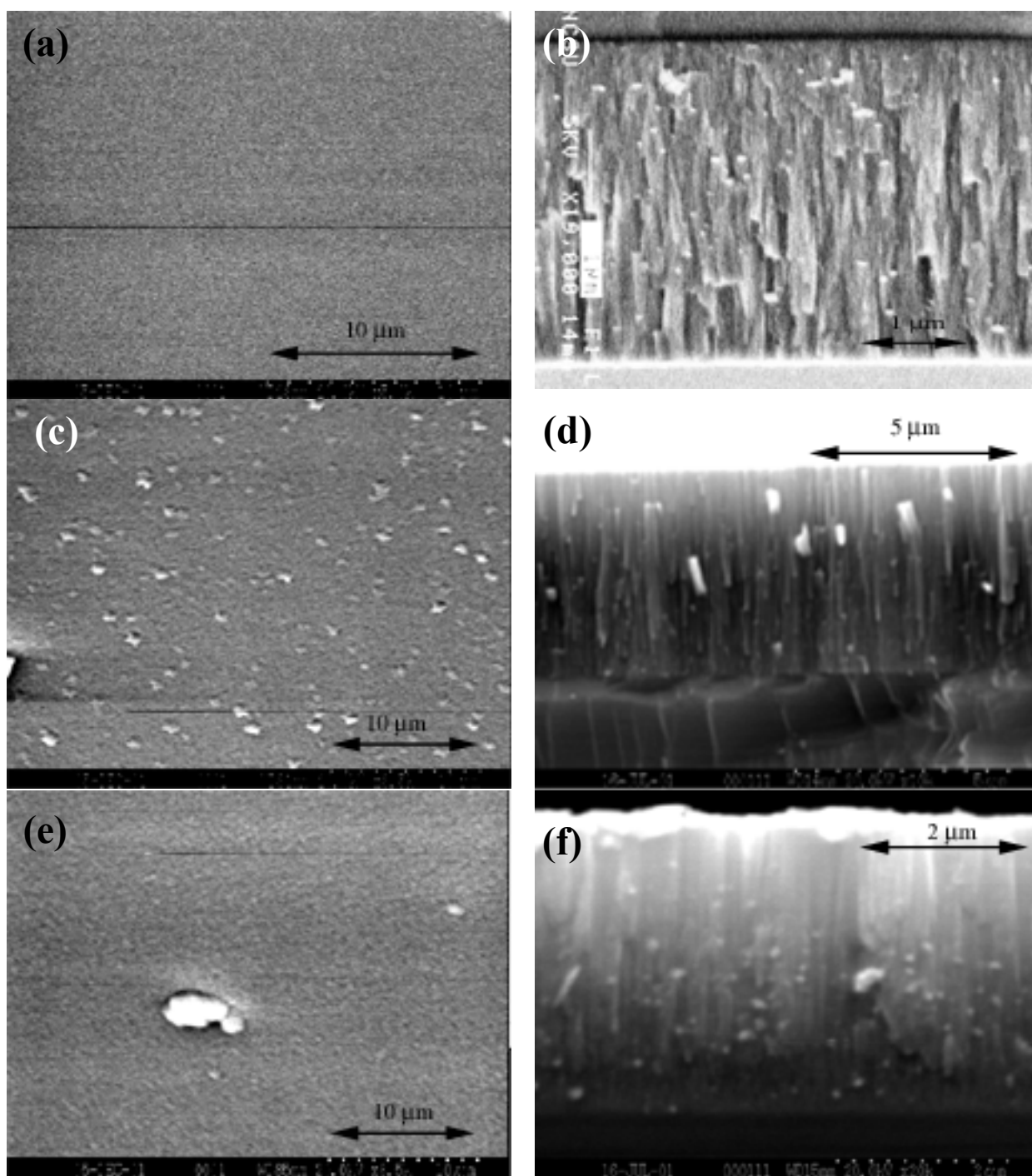


*Figure 3-17.* Surface morphologies and cross section of the aluminum nitride thin films grown with (a) and (b) 5 mT, (c) and (d) 10 mT, (e) and (f) 28 mT of sputtering pressure at 250 kHz and 60% of duty cycle (500°C of growth temperature, 2 A of target current, 70% of nitrogen).

The cross section photographs showed that the AlN films have a columnar structure for deposition conditions. Cracks were observed in the film grown with 5 mT of sputtering pressure (*Figure 3-16 (a)*). This might be due to the impartment of high energy to the film as mentioned before. The film grown at 10 mT of sputtering pressure had round grains (*Figure 3-16 (b)*). The AlN film grown at 28 mT of sputtering (*Figure 3-16 (e)*) showed a rough surface.

The microstructure of the AlN films grown at 250 kHz/60% duty cycle is shown in *Figure 3-17*. The AlN film grown at a low pressure, 5 mT (*Figure 3-17 (b)*) had discontinuous columns and smooth surface (*Figure 3-17 (a)*). The films grown at 250 kHz/60% duty cycle seemed to have denser structure. The surface roughness of the aluminum nitride films increased with increasing the sputtering pressure for both frequencies as shown in *Figures 3-18*.

#### **3.2.4. Nitrogen concentration change**

*Figure 3-19* shows the XRD results of the aluminum nitride thin films on Si (100) with variations of nitrogen content when a 100 kHz/80% duty cycle was used. Total sputtering pressure of argon and nitrogen mixture was kept 10 mT. The target current was 2 A. The multi-orientations with very weak intensities were obtained at 50% and 90% of nitrogen content (*Figures 3-19 (a) and (c)*) while strong (002) peak was observed in the aluminum nitride grown with 70% of nitrogen content. The plasma composition is an important parameter for making stoichiometric films. The crystal orientation of the AlN films changed dramatically with nitrogen contents. It was reported that the (002) peak intensity of AlN increases [15, 16] with increasing nitrogen content above 50% of nitrogen in RF sputtering. On the contrary, Okano reported [77] that the c-axis orientation has been improved with decreasing N<sub>2</sub> concentration. Kumar et al. [78] also obtained highly oriented c-axis AlN films at low N<sub>2</sub> concentrations. These conflicting results may be due to the different types of sputtering power and system design. Therefore the results cannot be compared directly with reported results.

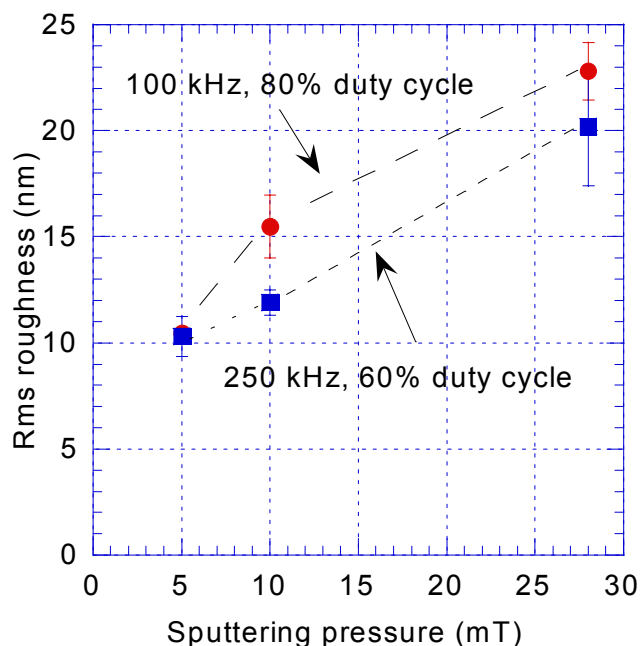


*Figure 3-18.* Surface roughness (rms) of the AlN films grown on Si (100) with variations of sputtering gas pressure (500°C of growth temperature, 70% of N<sub>2</sub>, 2 A of target current).

---

There will be changes in the mean free path of sputtered particles, ionization cross-sections, target surface state and ionization energy as well as plasma chemical composition when the relative content of nitrogen gas is increased. These factors may influence the crystal orientation of the deposited films.

The dependence of nitrogen content on deposition rate is shown in *Figure 3-20*. The deposition rate was highest at 70% of nitrogen content where the XRD showed c-axis orientation. The film deposited with the high nitrogen content of 90% has a low deposition rate. It might be due to the inefficient sputter yield of the nitrated target.

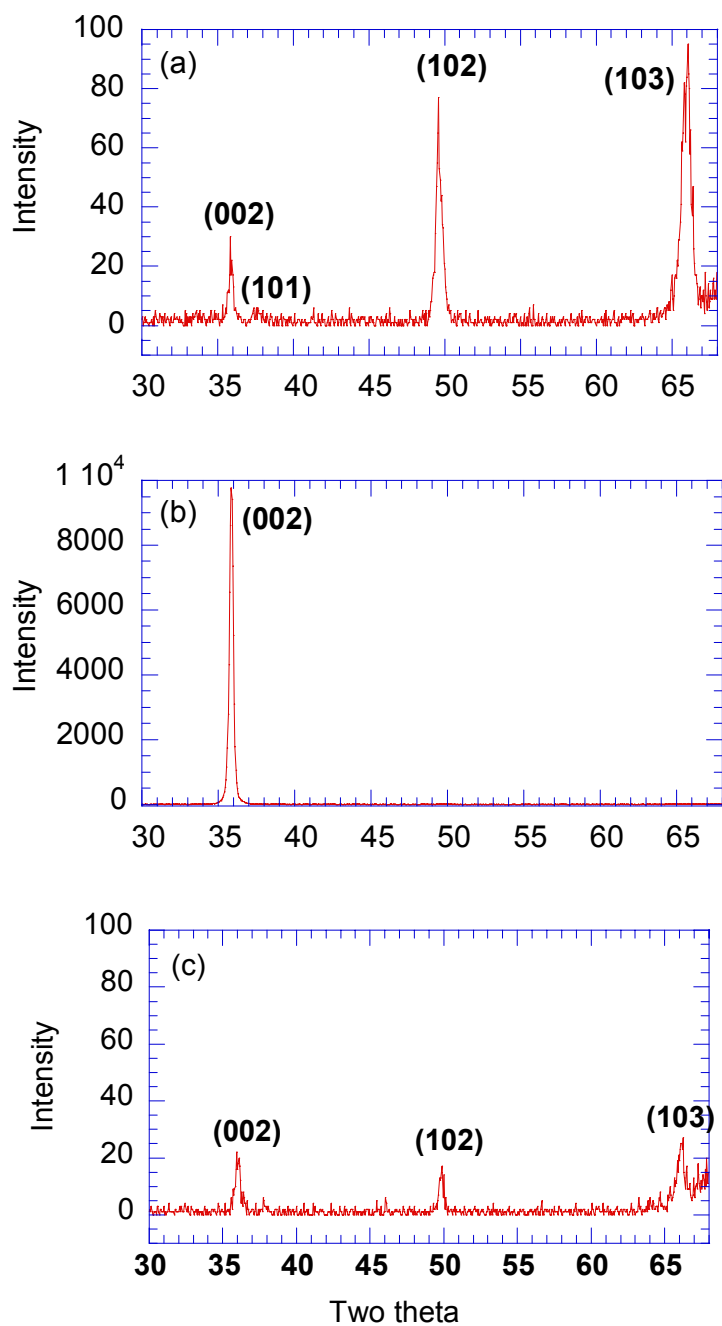
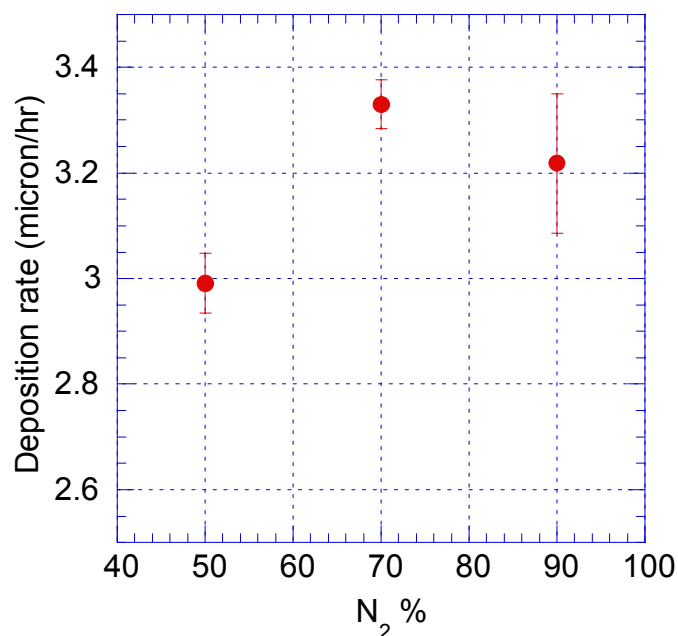


Figure 3-19. XRD results of the aluminum nitride thin films on Si (100) prepared by (a) 50%, (b) 70% and (c) 90% of N<sub>2</sub> (500°C of growth temperature, 2 A of target current, 10 mT sputtering pressure, 100 kHz of frequency, 80% of duty cycle).



*Figure 3-20.* Deposition rates of the aluminum nitride thin films on Si (100) with N<sub>2</sub> contents (500°C of growth temperature, 2 A of target current, 10 mT sputtering pressure, 100 kHz of frequency, 80% of duty cycle).

---

*Figure 3-21* shows the microstructures of the aluminum nitride thin films with the variation of nitrogen content. The cross-section views showed a columnar structure. The AlN films were dense for all nitrogen contents. The roughness of the AlN film grown at 70% of nitrogen was highest,  $R_a \sim 16$  nm (Figure 3-22)

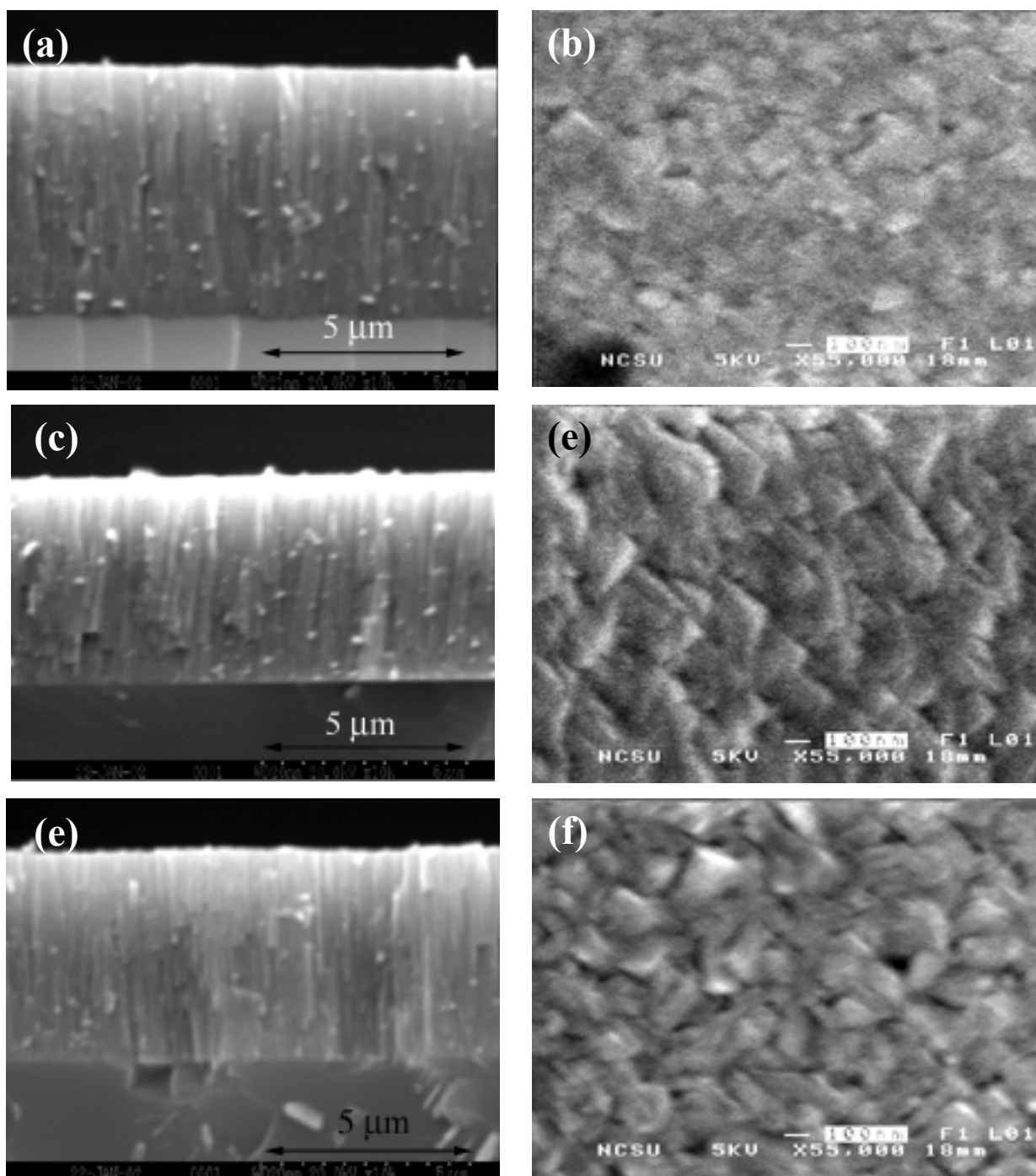
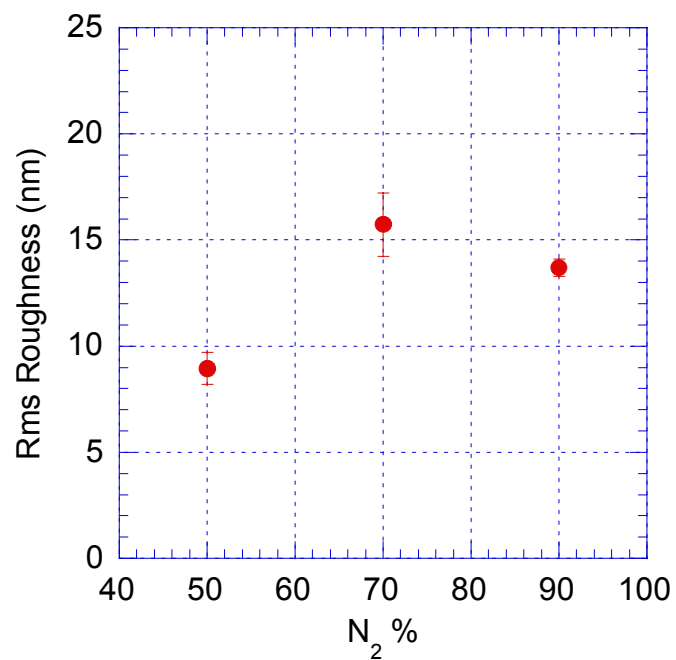


Figure 3-21. Cross section views and surface morphologies of the aluminum nitride films on Si (100) grown with (a) and (b) 50%, (c) and (d) 70%, (e) and (f) 90% of  $N_2$  at 10 mT of sputtering pressure. (500°C of growth temperature, 2 A of target current, 100 kHz of frequency, 80% of duty cycle).



*Figure 3-22.* Surface roughness (rms) of the AlN films grown on Si (100) with variations of N<sub>2</sub> content (500°C of growth temperature, 2 A of target current, 100 kHz of frequency, 80% of duty cycle).

---

### 3.2.5. Negative pulse time

The effects of negative pulse  $\tau_{on}$  on the properties of AlN films were examined. The reverse pulse time  $\tau_{rev}$  was set to a constant of 0.496  $\mu\text{sec}$  and  $\tau_{on}$  was increased from 3.504  $\mu\text{sec}$  to 12.834  $\mu\text{sec}$  as shown in *Figure 3-23*. The XRD results of the aluminum nitride thin films are shown in *Figure 3-24*. The aluminum nitride film grown with 12.834  $\mu\text{sec}$  of negative pulse time (*Figure 3-24 (a)*) showed a strong (101) peak with weak (002) and (102) peaks. With decreasing the negative period to 9.504  $\mu\text{sec}$  (*Figure 3-24 (b)*), the (002) peak of AlN was found to grow. Only the (002) peak was observed with further decrease in the negative voltage period to 3.504  $\mu\text{sec}$  (*Figure 3-24 (c)*).

The plot of deposition rates of AlN films versus negative voltage period is shown in *Figure 3-25*. The deposition rate reached maximum when  $\tau_{on}$  was 9.504  $\mu\text{sec}$ . Since actual sputtering occurs during negative pulse  $\tau_{on}$ , it is expected that the deposition rate would be highest at the longest  $\tau_{on}$ . The  $\tau_{rev}$  might be too short to remove charges completely accumulated during the negative voltage period, resulting in a decrease in ion bombardment on the target surface and a decrease in deposition rates. Kelly et al. [38] studied the effect of reverse voltage magnitude on deposition rate. Increasing the reverse voltage increased from 10 to 20% of the normal operating voltage resulted in an increase in the deposition rate of almost 50%. This effect has been attributed to enhanced target cleaning during reverse pulse.

The microstructures of the AlN films on Si (100) are shown in *Figure 3-26*. The non-continuous columnar structures are observed in *Figure 3-26 (a)*. The aluminum nitride thin film grown with short negative pulse showed very dense structure (*Figure 3-26 (e)*). The rms roughness also increased with the negative pulse time (*Figure 3-27*).

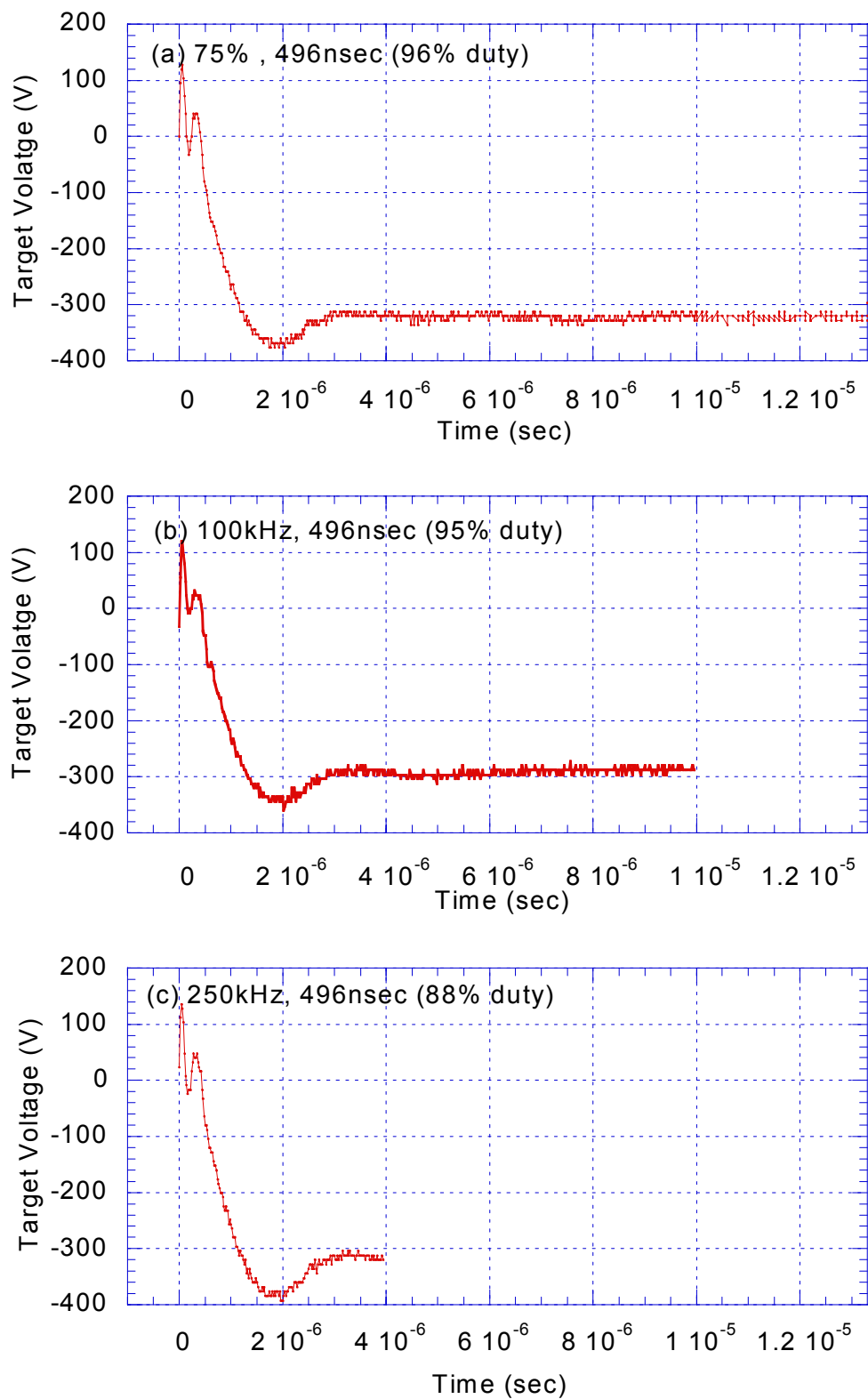


Figure 3-23. Target voltage vs. time at 496 nsec of constant reverse pulse time.

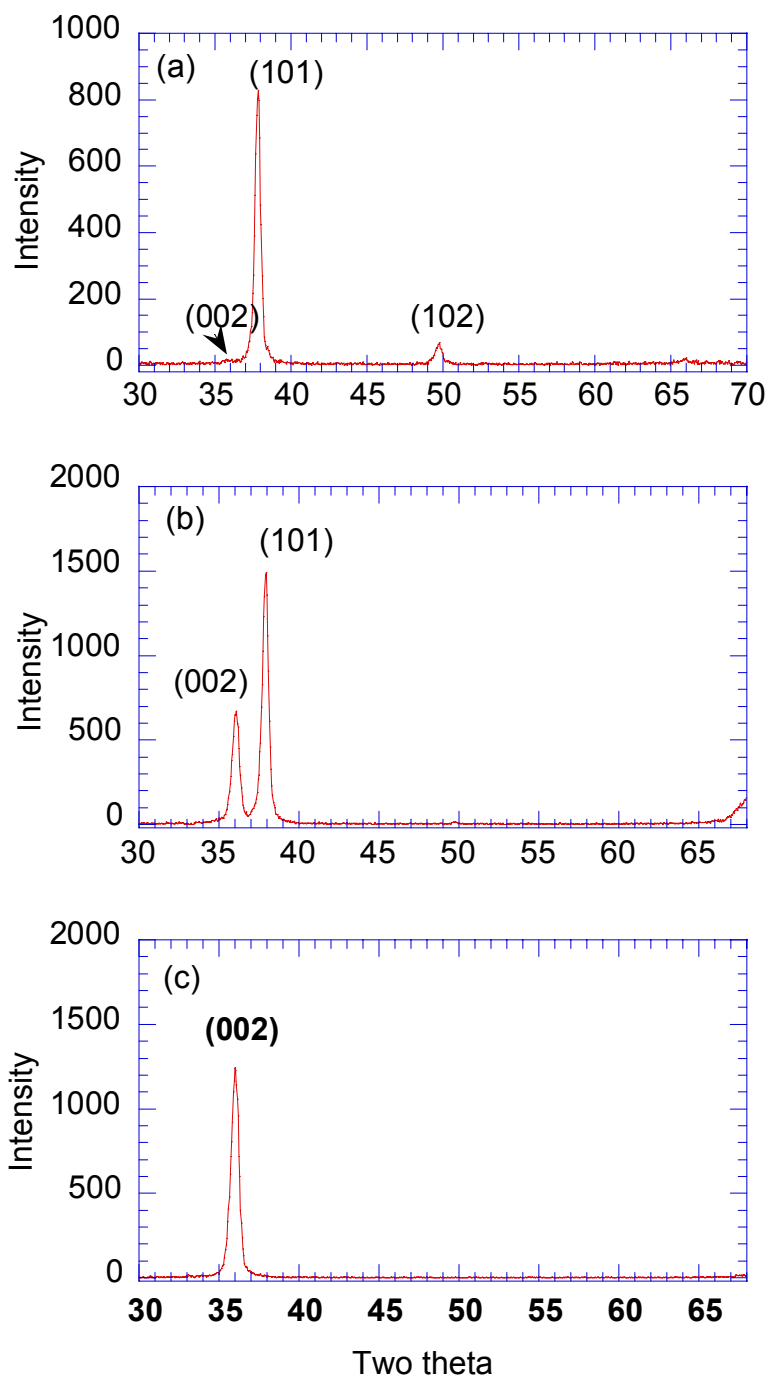
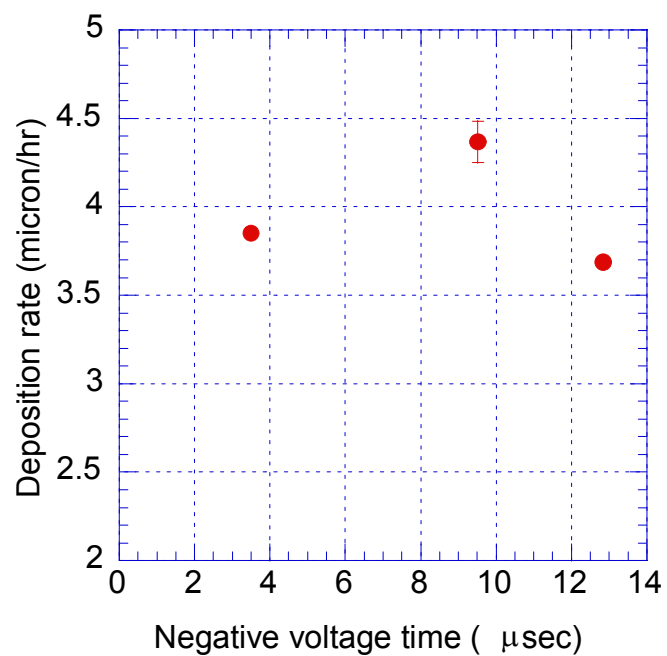


Figure 3-24. XRD results of the aluminum nitride thin films on Si (100) prepared at (a) 12.834  $\mu\text{sec}$ , (b) 9.504  $\mu\text{sec}$  and (c) 3.504  $\mu\text{sec}$  of negative pulsed time (500 $^{\circ}\text{C}$  of growth temperature, 28 mT of sputtering pressure, 70% of  $\text{N}_2$ , 2 A of target current, 496 nsec of reverse pulse time).



*Figure 3-25.* Deposition rates of the aluminum nitride thin films on Si(100) with negative period variations (500°C of growth temperature, 28 mT of sputtering pressure, 70% of N<sub>2</sub>, 2 A of target current, 496 nsec of reverse pulse time).

---

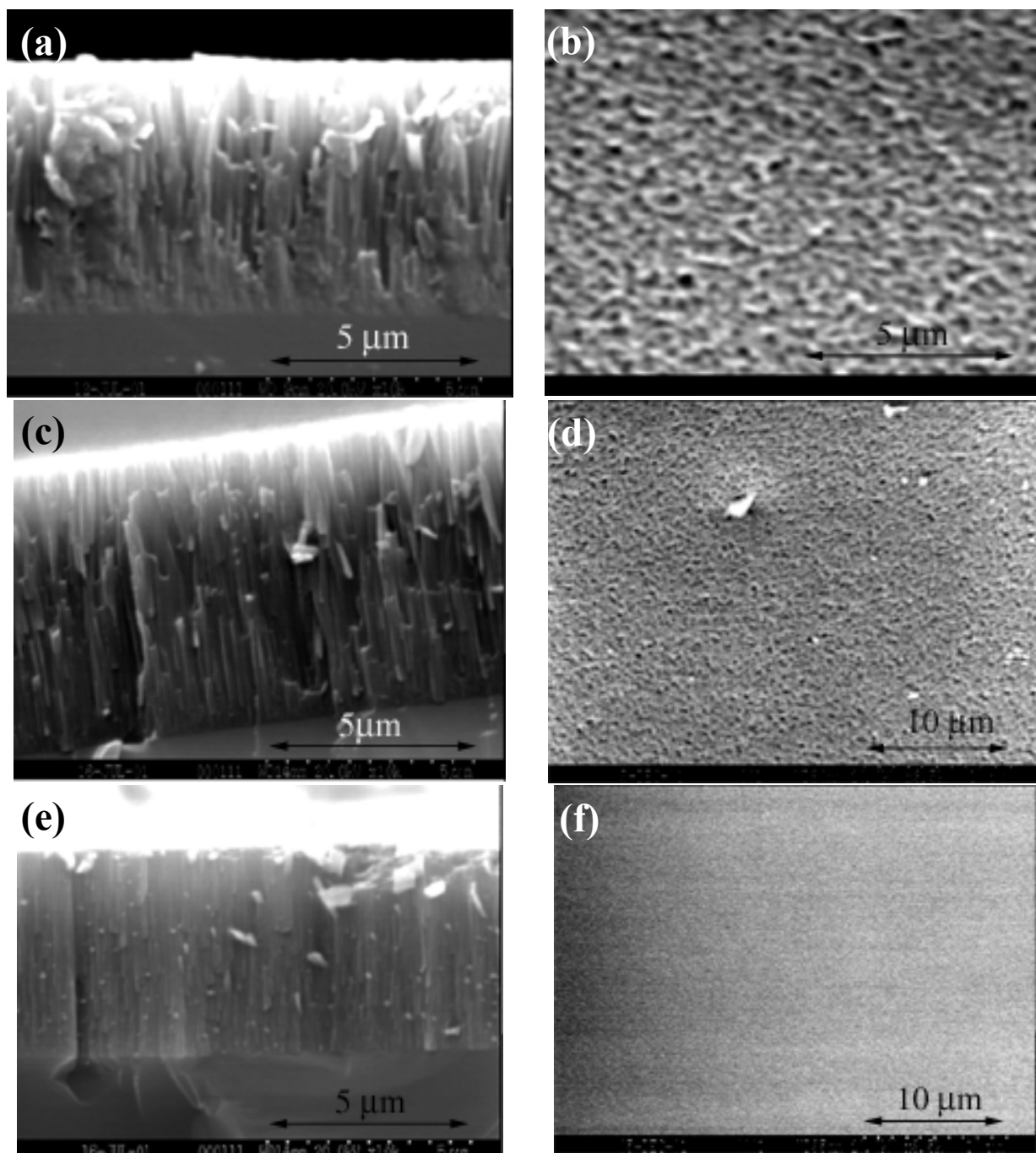
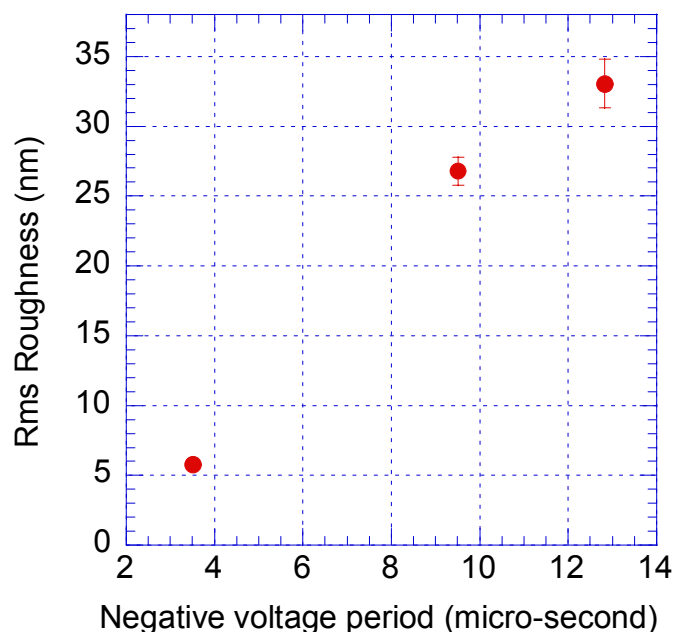


Figure 3-26. Cross sections and surface morphologies of the aluminum nitride thin films on Si (100) prepared with (a), (b) 12.834  $\mu\text{sec}$ , (c), (d) 9.504  $\mu\text{sec}$  and (e), (f) 3.504  $\mu\text{sec}$  of negative pulse time (500°C of growth temperature, 28 mT of sputtering pressure, 70% of  $\text{N}_2$ , 2 A of target current, 496 nsec of reverse pulse time).



*Figure 3-27.* Surface roughness (rms) of the AlN films grown on Si (100) with variations of negative pulsed time. (500°C of growth temperature, 28 mT of sputtering pressure, 70% of N<sub>2</sub>, 2 A of target current, 496 nsec of reverse pulse time).

---

### 3.2.6. Frequency/duty cycle change

The effect of frequency and duty cycle change on the crystal orientation of AlN thin films was investigated. *Figure 3-28* shows the XRD of the AlN thin films grown at 75 kHz at 60%, 80% and 96% of duty cycle. The deposition condition was 500°C of growth temperature, 28 mT of sputtering pressure, 70% of N<sub>2</sub>, and 2 A of target current. The (101) and (102) peaks were observed for all duty cycles. The ration of (101) and (102) peaks increases with increasing duty cycle. The XRD result of the AlN films grown at a frequency of 100 kHz is shown in *Figure 3-29*. The AlN thin film grown at 60% of duty cycle showed the c-axis orientation. The (101) peak increased while the

(002) peak decreased as the duty cycle increases. The crystal orientation of the AlN film with change in duty cycle at a frequency of 250 kHz showed opposite results (*Figure 3-30*). The c-axis orientation of the AlN film was obtained at a highest duty cycle of 88%. The AlN films showed the mixed orientation at low duty cycle of 60% and 80%.

The XRD results of the AlN films on Si (100) are summarized with respect to negative pulse time as shown in *Figure 3-31*. The aluminum nitride films tend to have (101) and (102) orientations at long negative pulse time ( $> 9 \mu\text{sec}$ ). The (002) peak began to grow as the negative pulse time decreased. In the middle negative pulse time, the c-axis orientation was obtained ( $3 \sim 6 \mu\text{sec}$ ). The (101) peak appeared again when the negative pulse time decreased further.

The effects of pulsing frequencies and duty cycles on deposition rate are shown in *Figure 3-32*. The deposition rates were plotted with respect to the negative pulse time. As the duty cycle increases, the deposition rates increased for all pulsing frequencies, 75 kHz, 100 kHz and 250 kHz due to the increase in sputtering time. At constant duty cycle of 60% and 80%, the deposition rate increases with decreasing pulsing frequency. The AlN film grown at 75 kHz had the lowest deposition rate even though it had the largest duty cycle.

### **3.2.7. Discussion on preferential orientation**

The crystal orientations of AlN films were strongly dependent on deposition condition. The mechanism for preferential orientation of AlN films has not been known clearly. The equilibrium form of wurtzite is made of {100} and {001} planes. The nucleation on the substrate will be random at the initial stage of crystal growth. But only some nucleations survive whose fastest growth directions are closest to the normal to the substrate. This geometrical selection causes preferential orientation. When the growth rate of the (100) plane is faster than that of the (001) plane, the nucleation with (100) planes normal to the substrate grows and it becomes the (100) preferred orientation.

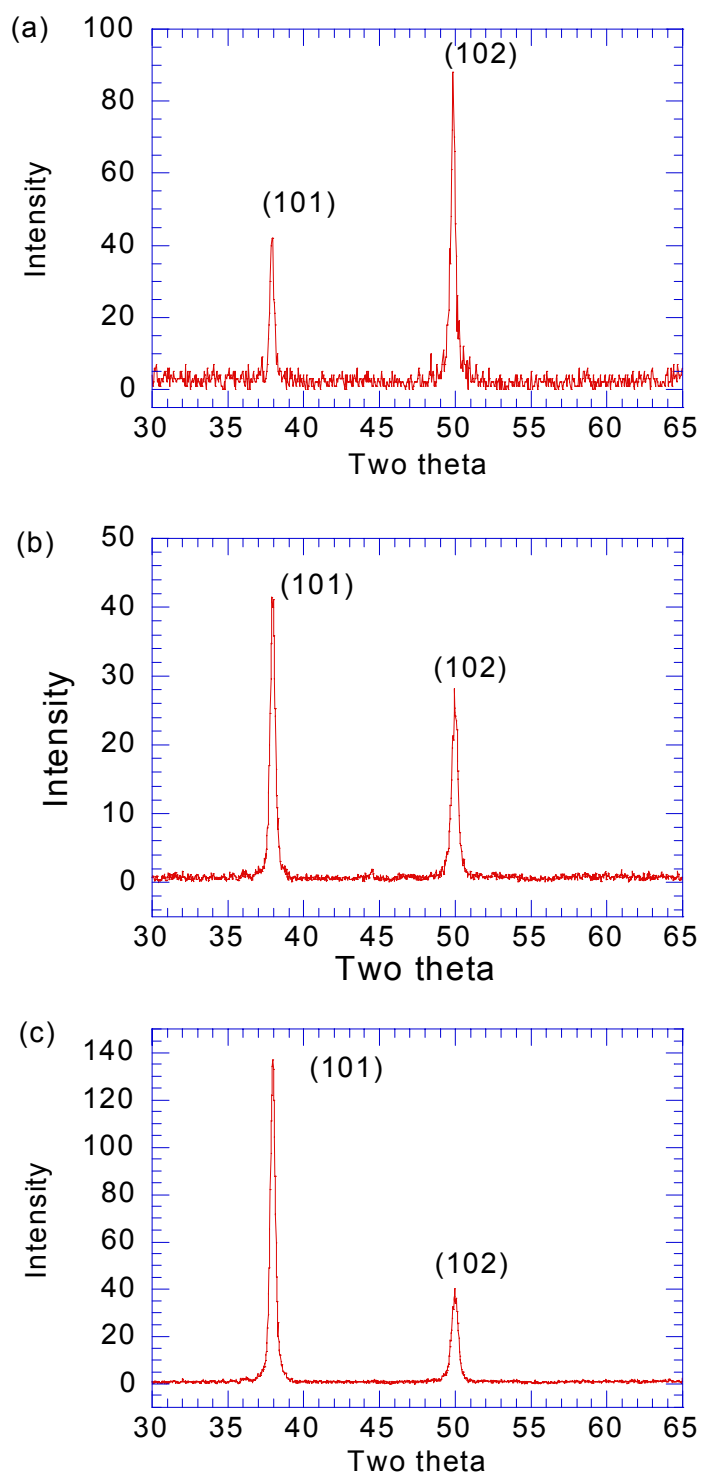


Figure 3-28. XRD results of the aluminum nitride thin films grown at (a) 60%, (b) 80% and (c) 96% of duty cycle at 75 kHz (500°C of growth temperature, 28 mT of sputtering pressure, 70% of N<sub>2</sub>, 2 A of target current).

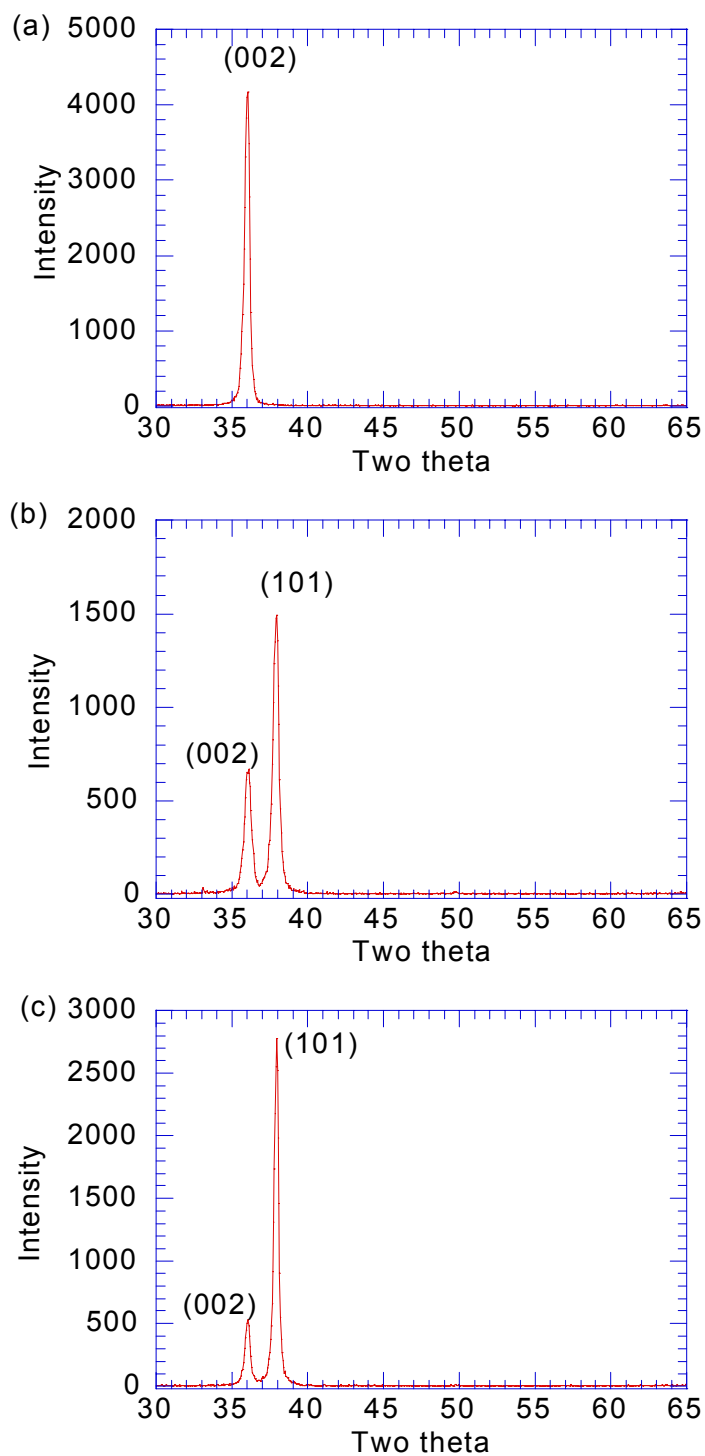


Figure 3-29. XRD results of the aluminum nitride thin films grown at (a) 60%, (b) 80% and (c) 95% of duty cycle at 100 kHz (500°C of growth temperature, 28 mT of sputtering pressure, 70% of N<sub>2</sub>, 2 A of target current).

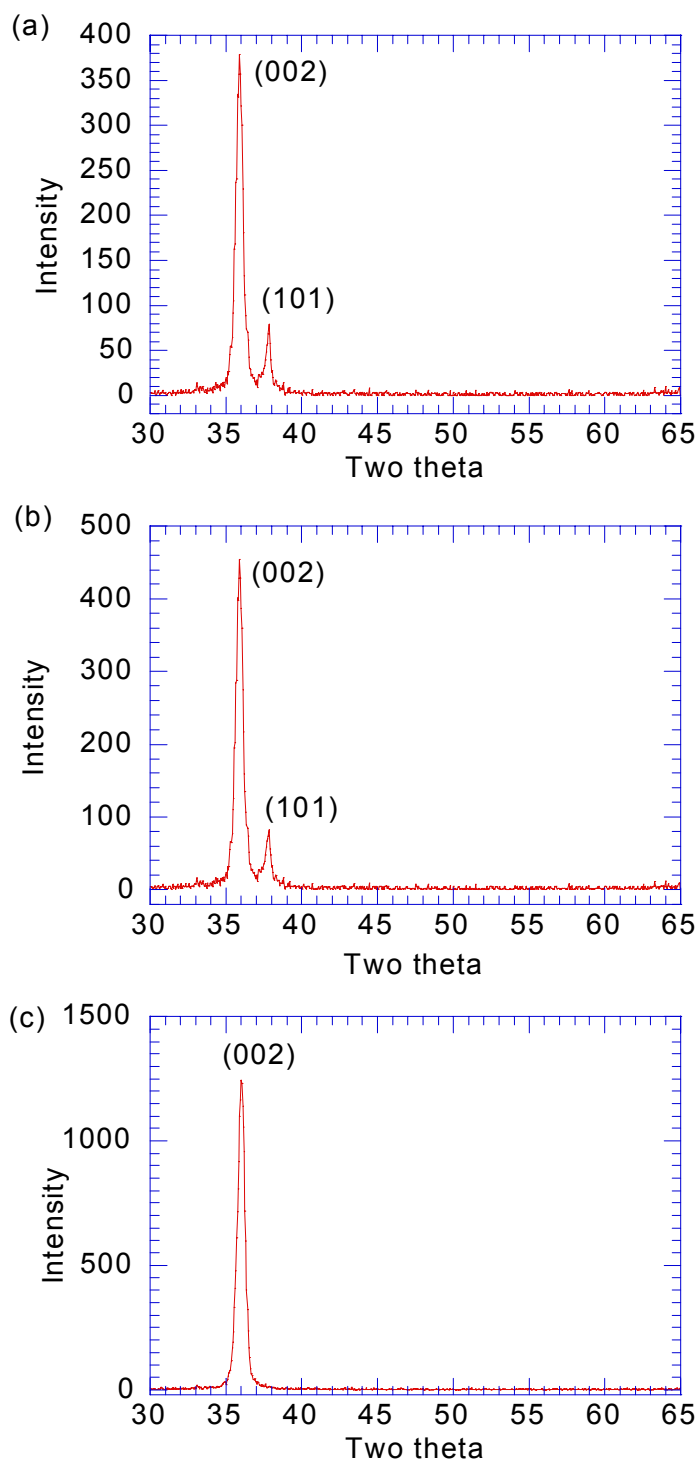


Figure 3-30. XRD results of the aluminum nitride thin films grown at (a) 60%, (b) 80% and (c) 88% of duty cycle at 250 kHz (500°C of growth temperature, 28 mT of sputtering pressure, 70% of N<sub>2</sub>, 2 A of target current).

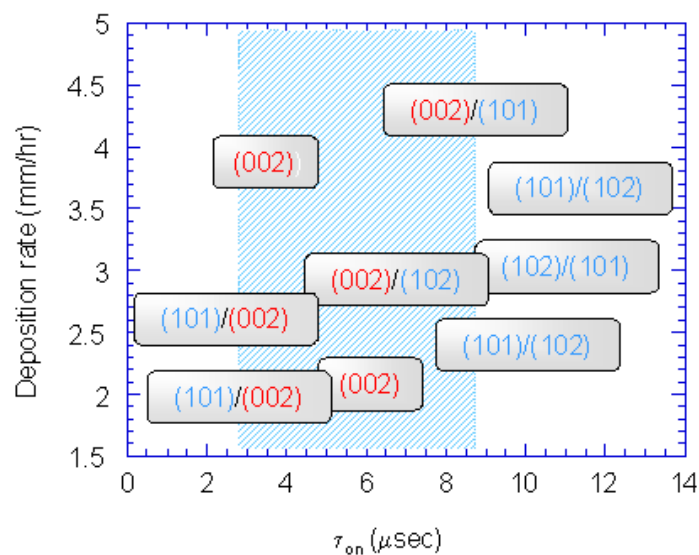


Figure 3-31. XRD results of the aluminum nitride films on Si (100) as a function of negative pulse time  $\tau_{on}$  (500°C of growth temperature, 28 mT of sputtering pressure, 70% of  $N_2$ , 2 A of target current).

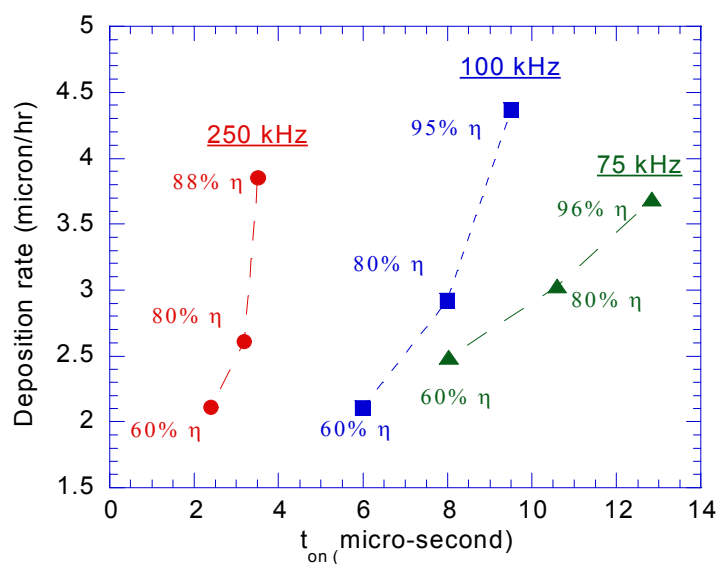


Figure 3-32. Deposition rates of the aluminum nitride thin films on Si (100) versus negative pulse time (500°C of growth temperature, 28 mT of sputtering pressure, 70% of  $N_2$ , 2 A of target current).

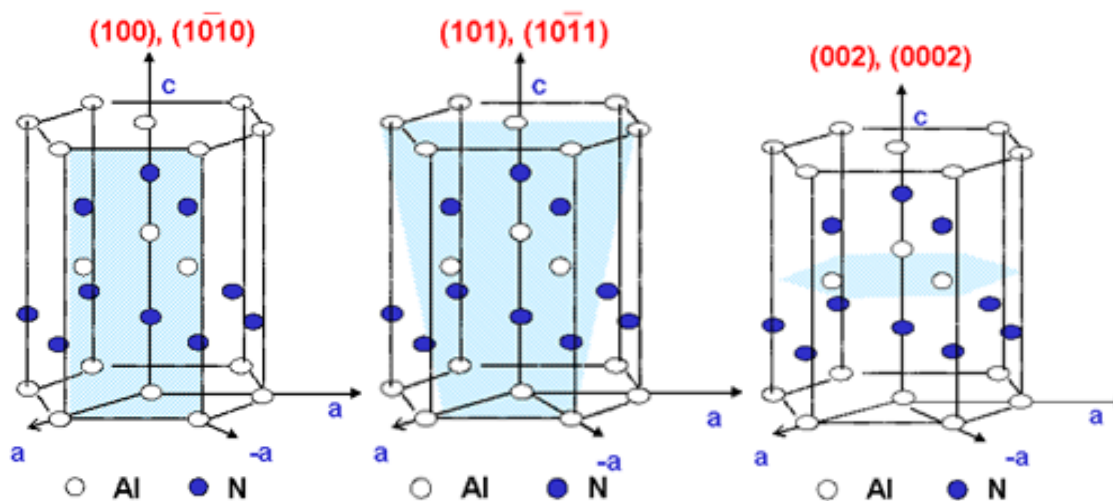


Figure 3-33. Geometry of the crystallographic planes for (002), (102) and (101) in the hexagonal AlN lattices.

Therefore, the difference in growth rate of the planes decides the orientation. Yumoto et al. [79] explained the preferential orientation of AlN films by an extended periodic bond chain (PBC) theory. The periodic bond chain model was originally proposed by Alexander to interpret the orientation mechanism of AlN films from the relationship of angles between the crystalline planes [80]. In this theory [67,79], Al-N dimers are formed when the collisions of Al and N atoms occur between the Al target and the substrate. Under these conditions, the (100) orientation tends to be obtained. Xu et al. [68] controlled the crystal orientation by changing experimental conditions, such as target power, pattering pressure and the distance between target and substrate. A longer distance and a higher sputtering pressure are conducive to the growth of AlN (100) films, whose c-axis is parallel with the substrate. It was explained by the decrease in energy of particles due to collisions between sputtered particles.

The crystalline structure of AlN was discussed in Chapter 1-1. The (002), (101) and (100) planes of the wurtzite structure are shown in *Figure 3-33*. For the (002) orientation, the c-axis is normal to the substrate and the plane parallel to the substrate is the close-packed basal plane, with either all aluminum or nitrogen atoms. On the other hand, for (100) or (110) orientations, where the c-axis is parallel to the substrate, the atoms are loosely packed and the plane consist of equal number of aluminum and nitrogen atoms. For the (101) orientation with either aluminum or nitrogen atoms, loosely packed structure than that for the (002) plane would be formed. As mentioned before, adatoms need a sufficient kinetic energy to rearrange themselves and form the (002) orientation. This energy can be supplied by changing target power, growth temperature, sputtering pressure, gas composition and negative pulse time. The crystal orientation of the AlN film will be correlated with the results of Langmuir probe in Chapter 5.

### **3.3. Electrical analysis**

#### **3.3.1. Dielectric characteristics of MIM capacitor**

Dielectric characteristics of a metal (Al or Mo)-AlN-metal (Al) (MIM) capacitor were evaluated. In order to know whether the aluminum or molybdenum electrode provided ohmic or Schottky contacts to the AlN films, measurement of capacitance  $C$  as a function of applied voltage  $V$  was made as shown in *Figure 3-34*. The capacitance is independent of the applied voltage. When Schottky barriers are formed on an insulator surface, a depletion region is generated. The capacitance  $C_d$  of the depletion region depends on the voltage drop  $V_j$  across the junction. For a constant impurity concentration,  $C_d^{-2}$  depends linearly on  $V_j$ . For varying impurity concentrations the value of  $d(C_d^{-2})/dV_j$  can be used to determine the doping profile [81]. The depletion region is not evident at the Al/AlN interface since  $C$  is independent of  $V$ . The contact is therefore ohmic rather than Schottky. The overall capacitance is then given by the geometric expression

$$C = \varepsilon\varepsilon_0 \frac{A}{d} \quad (3-1)$$

where  $C$  is the capacitance (F),  $\varepsilon$  is the dielectric permittivity,  $\varepsilon_0$  is the permittivity of vacuum ( $8.854 \times 10^{-12}$  F/m),  $A$  is the electrode area and  $d$  is the film thickness. *Figure 3-35* shows the plot of  $C$  as a function of electrode size at a constant films thickness. The capacitance increases linearly with electrode size for two different bottom electrodes. The slope of a plot is given by  $\varepsilon_r\varepsilon_0/d$  and gives a value of permittivity of the aluminum nitride thin film with known film thickness.

The dielectric constant and dielectric loss of the aluminum nitride thin films with aluminum and molybdenum as bottom electrodes are shown in Table 3-1. The dielectric constant was between 8.5 and 11.5, which is similar with reported values for AlN [82-92]. Adam et al. [84] reported the dependence of dielectric constant on film thickness. The dielectric constant was between 4 and 11 for thicker layers ( $\geq 100$  Å) and decreased to values between 2 and 6 for thicknesses below 100 Å. And Dimitrova et al. [90] reported low dielectric constants (6.8~7.1) due to the presence of nitrogen vacancies in the AlN lattice.

The aluminum nitride thin films grown on aluminum electrode have lower dielectric losses than those of the samples grown on polycrystalline molybdenum. The measured values are similar with those prepared by the DC magnetron sputtering method reported by Dimitrova et al. [90], but higher than other reported values [88,89]. The structural and electrical properties such as leakage current, dielectric properties, surface roughness and thermal stability are strongly related to the nature and state of the bottom electrode [93,94]. For dense materials having neither remnant second phase nor a highly contiguous matrix, the stable dielectric constant appears to be about 8.6 between 1 kHz and 1 MHz [95]. Xinjiao et al. [96] reported that c-axis oriented AlN film had a higher dielectric constant than non-oriented AlN film. However, there was no explanation about the results. The high dielectric constant of AlN may be attributed to the increased

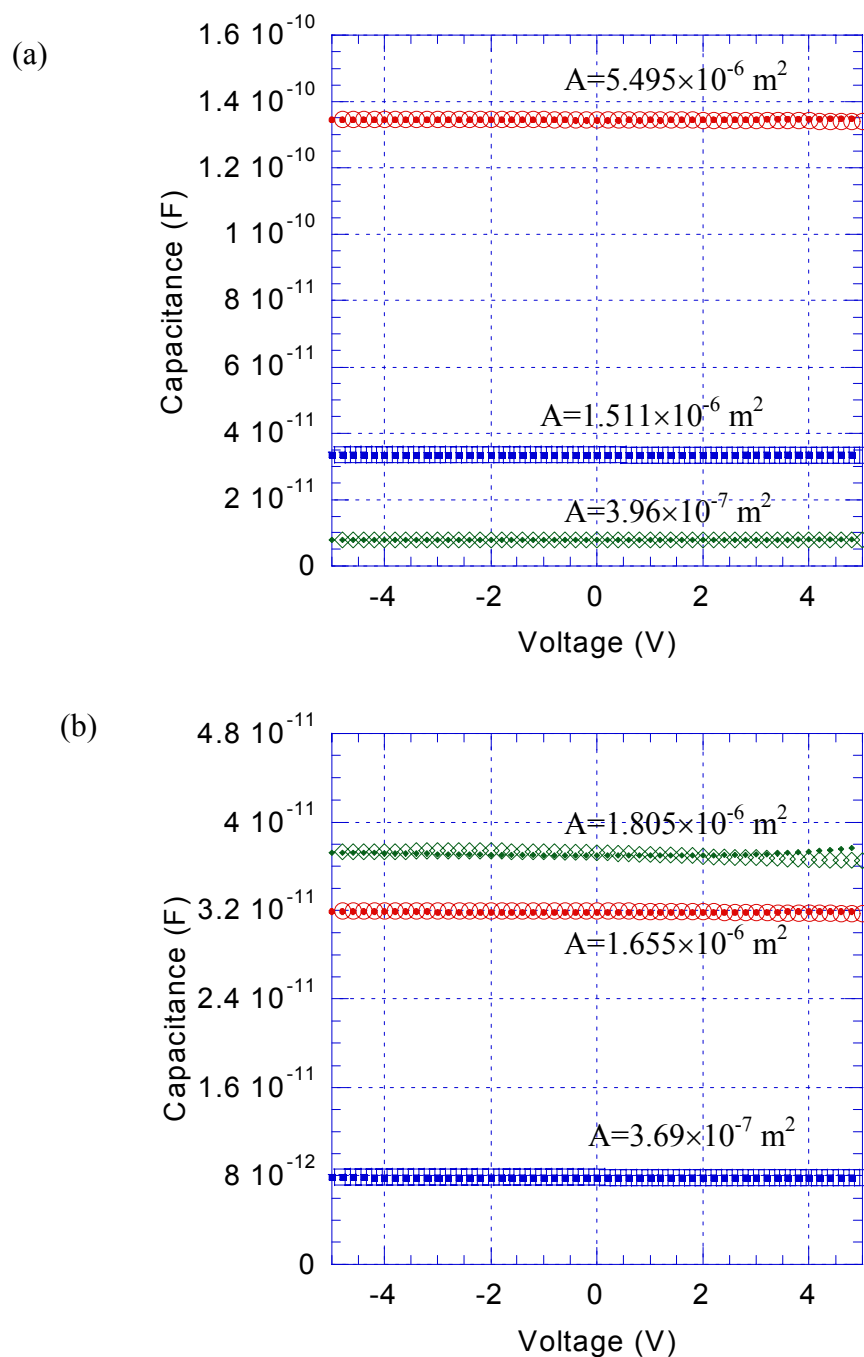
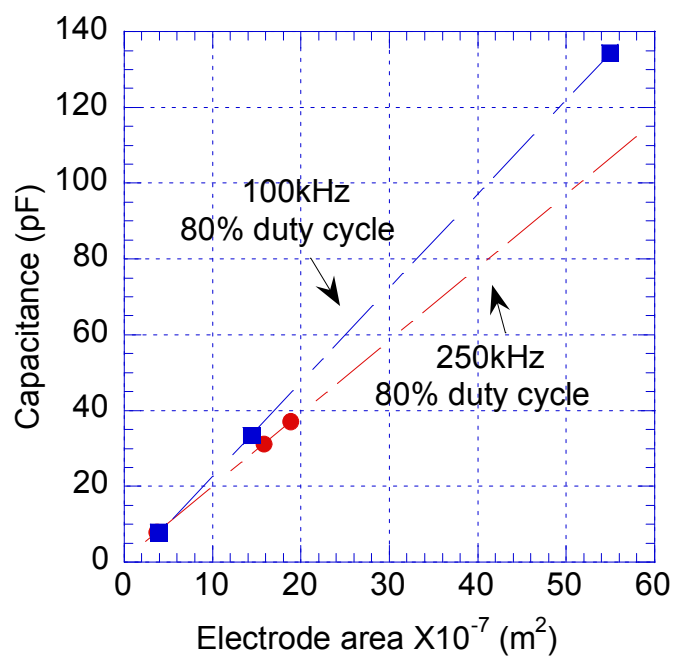


Figure 3-34. Capacitance versus voltage of the aluminum nitride films grown on (a) Al bottom electrode (100 kHz/80% duty cycle) and (b) molybdenum bottom electrode (250 kHz/80% duty cycle) with different top electrode areas. The measurement was performed at 100 kHz.



*Figure 3-35.* Capacitance versus electrode area of the aluminum nitride thin films measured at 100 kHz (Deposition condition; 28 mT of sputtering pressure, 70% of N<sub>2</sub>, 2 A of target current, 80% of duty cycle).

---

Table 3-1. Dielectric properties of the aluminum nitride films on Al and Mo measured at 100 kHz (Deposition condition: 500°C of growth temperature, 28 mT of sputtering pressure, 70% of N<sub>2</sub>, 2 A of target current). The number in parenthesis is standard deviation.

	Al bottom electrode		Mo bottom electrode	
	k	Loss	K	Loss
100 kHz	11.10 (0.88)	0.0706 (0.0031)	11.47	0.161 (0.015)
250 kHz(t=3.17 (0.093))	8.62	0.0775	9.3	0.133 (0.0011)
250 kHz(t=3.91 (0.093))	-	-	8.50 (0.25)	0.0807 (0.0021)
250 kHz(t=5.78 (0.0378))	8.50	0.0886 (0.0064)	11.5	0.233(0.053)

polarization due to impurities at grain boundaries and defects in structure, which is most pronounced at low frequency [83,84].

### 3.3.2. Current density-voltage measurement

The field dependence of DC conductivity was examined by the measurement of current density-electric field (J-E) characteristics. The current density versus electric field of the aluminum nitride thin films is shown in *Figure 3-36*. Several electrical processes can allow electrical charges to move in insulators, leading to sizable current densities. If current is linear with voltage V, conduction mechanism is ohmic. It occurs at a low field

strength. At high fields, these films exhibit a non-linear conduction. Possible dominant conduction mechanisms in non-linear relationship may be (a) Fowler-Nordheim tunneling, (b) Poole-Frenkel, (c) Schottky and (d) space charge limited conduction (SCLC) [93,97-99]. Since the film thickness used in the measurement is several microns, the tunneling process can be ruled out.

The ohmic's law is applied when current density  $J$  is proportional to voltage  $V$ .  $J$  is expressed as [97]

$$J = en_0\mu\frac{V}{d} \quad (3-2)$$

where  $n_0$  is the concentration of thermally generated electrons in the conduction band,  $\mu$  is the mobility and  $d$  is the film thickness. In higher electric fields, the power law conductivity may be identified with the space charge limited conductivity. This conductivity is dominated by an exponential distribution of trap levels, where  $J$  is given by

$$J = e\mu N_c \left( \frac{\varepsilon}{eN_0 kT_t} \right)^l \frac{V^{l+1}}{d^{2l+1}} \quad (3-3)$$

$$J = kE^n \quad (3-4)$$

where  $N_c$  is the effective density of states in the conduction band,  $l$  is  $n-1$ ,  $E$  is the electric field ( $V/d$ ) and  $n$  is the power exponent. The distribution of trap is described by

$$N(E) = N_0 \exp\left(-\frac{E}{kT_t}\right) \quad (3-5)$$

where  $N(E)$  is the trap density unit energy range at an energy  $E$  below the conduction band edge,  $N_0$  is the trap density per unit energy range at the conduction band edge and  $T_t$  is a temperature parameter characterizing the distribution.

If the conduction mechanism of the dielectric film is the Poole-Frenkel conduction based on the field-assisted carrier excitation from centers within band gap. The following relationship is governed

$$J = J_0 \exp\left(\frac{\beta_{PF} V^{1/2}}{kTd^{1/2}}\right) \quad (3-6)$$

where  $J_0$  ( $=\sigma_0 E$ ) is the low-field density,  $E$  is the electric field,  $k$  is the Boltzmann's constant,  $T$  is the absolute temperature and  $\beta_{PF}$  is the Poole-Frenkel field-lowering coefficient given by  $\beta_{PF}=(e^3/\pi\epsilon_r\epsilon_0)^{1/2}$ , where  $e$  is the electronic charge. Schottky emission shows a similar linear variation between  $\log J$  and  $V^{1/2}$  at low voltage fields. The Schottky field-lowering coefficient  $\beta_s$  is half the value of  $\beta_{PF}$  (at high voltage fields). Schottky emission is prominent where the electrode contacts dominate the conduction and Poole-Frenkel emission is important in thicker films where bulk defects dominate the conduction.

The absence of linearity between  $\ln J$  vs.  $V^{1/2}$  eliminates the Poole-Frenkel conduction mechanism. Szmidt et al. [91] reported the Poole-Frenkel conduction in nanocrystalline AlN films ( $\epsilon \sim 8$ ) on Si and GaAs prepared by MOCVD. The current density with an electric field variation is plotted logarithmically as shown in *Figure 3-37*. The slopes are all about unity, which indicates ohmic conduction up to the upper limit of an electric field in the measurement ( $\sim 100$  kV/cm). The curve fittings for the measured  $J$  versus  $E$  by using Eq. (3-4) are summarized in Table 3-2.

According to the SCLC theory [93,100], this ohmic mode occurs in insulating films as long as the bulk-generated current in film exceeds the current due to an injected free carrier from the electrodes. Adam et al. [84] prepared the electrical properties of aluminum nitride thin films by reactive magnetron sputtering for gate dielectrics.

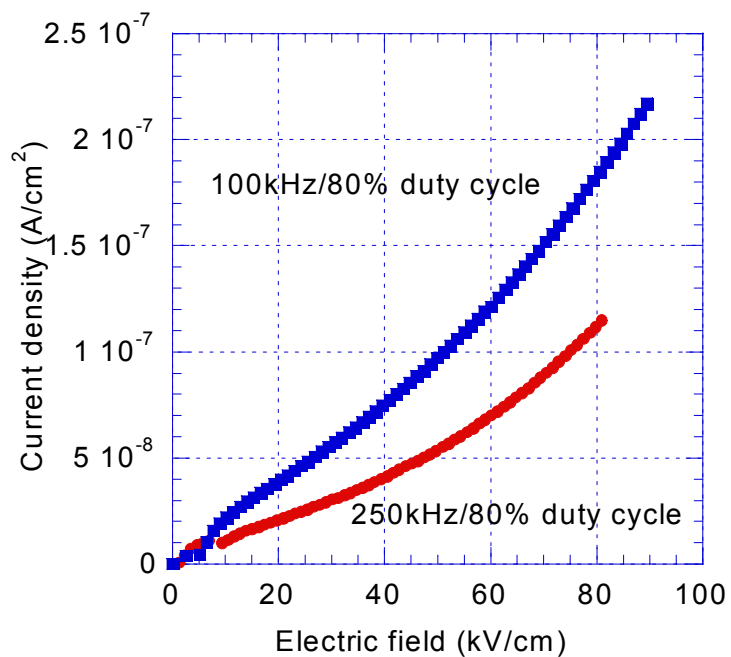


*Figure 3-36.* Current density-electric field curve of the aluminum nitride thin films on molybdenum bottom electrode grown at different frequencies (Deposition condition: 500°C of growth temperature, 28 mT of sputtering pressure, 70% of N<sub>2</sub>, 2 A of target current).

---

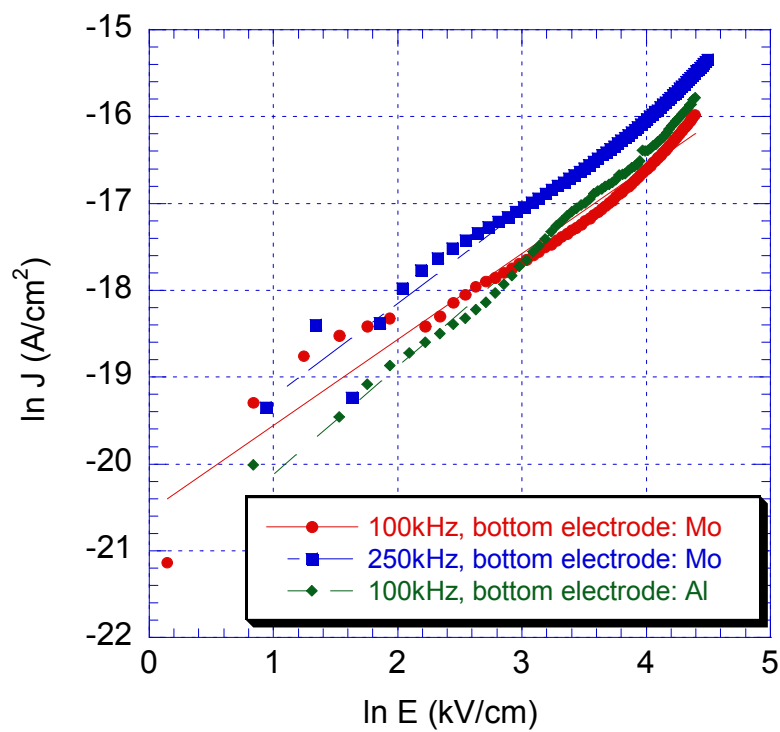


*Figure 3-37.*  $\ln J$  vs.  $\ln E$  curves of the aluminum nitride thin films (500°C of growth temperature, 28 mT of sputtering pressure, 70% of  $\text{N}_2$ , 2 A of target current, 80% of duty cycle).

Table 3-2. Summary of the curve fitting results of  $\ln J$  vs  $\ln E$ .

	100 kHz, 80% $\eta$ AlN on Mo electrode	100 kHz, 80% $\eta$ AlN on Al electrode	250 kHz, 80% $\eta$ AlN on Mo electrode
Eq. from curve fitting*	$J=1.52 \times 10^{-9} E^{1.079}$ (R=0.99064)	$J=5.26 \times 10^{-10} E^{1.2439}$ (R=0.99741)	$J=1.19 \times 10^{-9} E^{0.99057}$ (R=0.97988)
Power exponent, n	1.079	1.2439	0.99057
$e n_0 \mu^{**}$	$1.52 \times 10^{-9}$	$5.26 \times 10^{-10}$	$1.19 \times 10^{-9}$

\*J in  $A/cm^2$ , E in kV/cm

\*\* From Eq. (2)

The current-voltage of the AlN didn't follow either Fowler-Nordheim tunneling or Frenkel-Pools emission transport mechanism [84].

Leakage current and dielectric breakdown voltage can't be obtained due to the instrumental limit. However, the aluminum nitride thin films withstand up to max. electric field in the measurement (~100 kV/cm). The reported breakdown voltage of the aluminum nitride thin films is 1~6 MV/cm. Generally, the thicker the film is, the more imperfections are produced in the sputtered film. It results on poor homogeneity of the film [96]. Liufu et al. [92] ascribed the dc breakdown voltage dependence on film thickness due to the decrease in heat transfer with increasing film thickness as one of the decreasing factors. They observed that results in silicon dioxide and other dielectric materials.

### 3.4. Residual stress analysis

Virtually all vacuum-deposited coatings are in a state of stress. The total stress is composed of thermal stress and intrinsic stress [46,101]. Thermal stress is due to the difference between the thermal expansion coefficients of the coating and substrate materials. The intrinsic stress is due to the accumulation effects of the crystallographic flaws that are built into the coating during deposition.

Large residual stresses that develop in the film may cause micro-cracks in the film or cause the film to peel off from the substrate. Therefore, the control of residual stress is essential in order to synthesize mechanically stable AlN films.

The stress of the deposited AlN films was estimated by x-ray diffraction analysis. In the following, the stress analysis method in references [69] and [102] was used.

Two assumptions are made in the stress analysis: (1) the stress state in the films is equi-biaxial and (2) the crystal is very small and each crystal has a random orientation around the c-axis with  $2\pi$  rotational freedom. Under these assumptions, the relationship between the lattice strain  $\varepsilon_{33}^L$  and the stress  $\sigma$  is

$$\varepsilon_{33}^L = \left\{ (s_{11}^C + s_{12}^C - 2s_{31}^C) \sin^2 \Psi + 2s_{31}^C \right\} \sigma \quad (3-7)$$

where  $s_{ij}^C$  is the elastic compliances of a single crystal and  $\psi$  is the angle between the normal axis of the diffracting planes and the surface normal axis, which is identical to the c-axis. Eq. (3-7) indicates that lattice strains for each diffraction plane should lie on a straight line against  $\sin^2 \psi$ . From the slope of the line determined by the least-square method, the stress value can be estimated by knowing the elastic compliances of the aluminum nitride. The values of  $s_{ij}^C$  for an AlN crystal are:  $s_{11}^C = 0.35 \times 10^{-5}$ ,  $s_{12}^C = -0.10 \times 10^{-5}$ ,  $s_{31}^C = -0.08 \times 10^{-5} \text{ Mpa}^{-1}$  [69]. Table 3-3 summarizes the angle  $\psi$  and diffraction planes.

In this stress analysis method, various diffraction planes in a wide range of  $\psi$  angles were used for the measurement of lattice strain.

---

Table 3-3. Diffraction planes and related parameters. (Cu K $\alpha$  = 1.541 Å)

hkl	2 $\theta$	$\psi$	$\sin^2\psi$
002	36.041	0	0
101	37.917	61.6	0.77
102	47.816	42.8	0.46
103	66.054	31.6	0.27

AlN powder is used as a standard material in order to eliminate errors due to misalignment of the stress measurement system. The strain is then calculated by the following equation:

$$\varepsilon_{33}^L = \varepsilon_{(hkl,\psi)} = \frac{d_{f(hkl,\psi)} - d_{p(hkl,\Xi)}}{d_{p(hkl,\Xi)}} \quad (3-8)$$

where  $d_f$  and  $d_p$  are the measured interplanar distances of the film and the powder, respectively.

The relation of strain versus  $\sin^2\psi$  plot is shown in *Figure 3-38*. Tables 3-4 and 3-5 summarize the stress estimation with change in sputtering pressure change at two deposition conditions, 100 kHz, 80% duty cycle and 250 kHz, 60% duty cycle. The negative sign in slope means compressive stress while positive sign means tensile stress in the films. As sputtering pressure decrease, the magnitude of the residual stress increases.

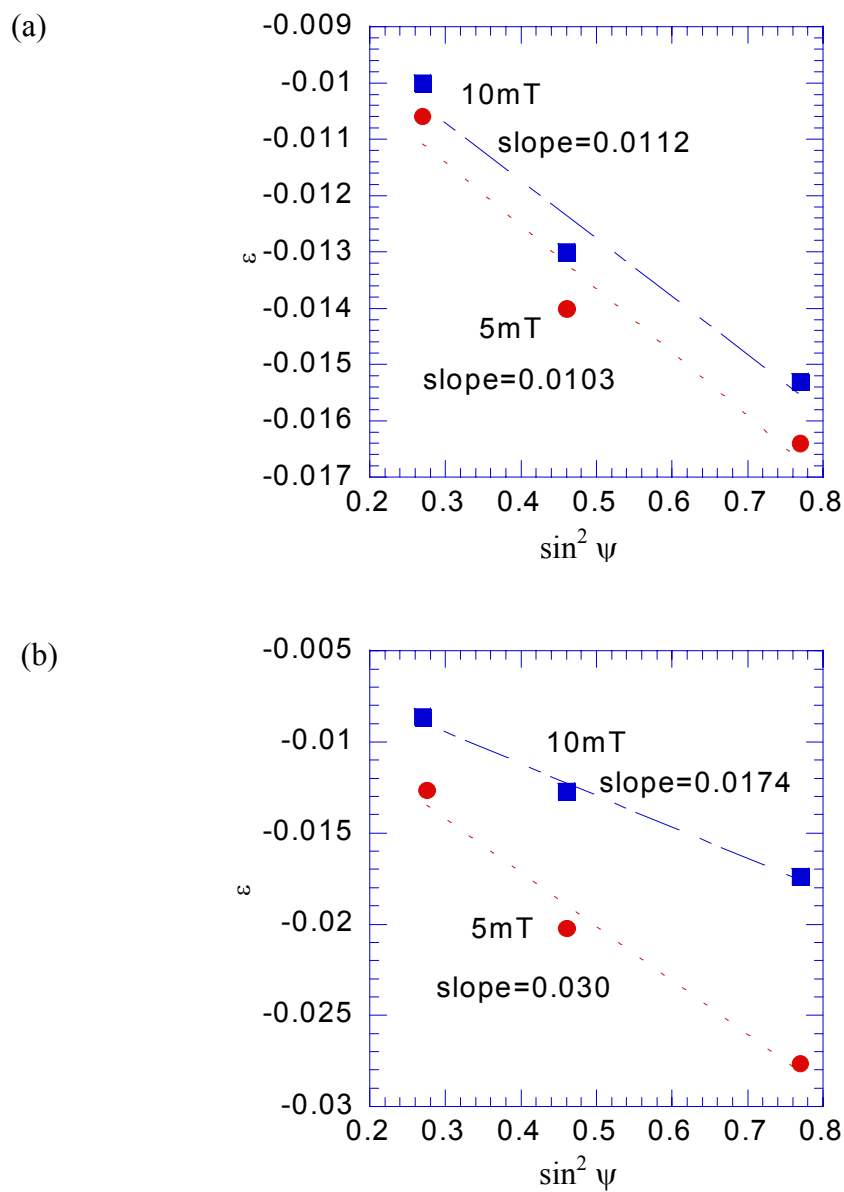


Figure 3-38. Plot of  $\sin^2 \psi$  and lattice strain obtained from XRD pattern of the AlN films grown at (a) 100 kHz/80% duty cycle and (b) 250 kHz/60% duty cycle (500°C of growth temperature, 70% of  $N_2$ , 2 A of target current).

Table 3-4. Residual stresses of the aluminum nitride films on Si (100) at different sputtering pressures. (500°C of growth temperature, 70% of N<sub>2</sub>, 2 A of target current).

	100 kHz/80% duty cycle		250 kHz/60% duty cycle	
	5 mT	10 mT	5 mT	10 mT
Sputtering pressure	5 mT	10 mT	5 mT	10 mT
Residual stress (GPa)	-2.84	-2.51	-7.2	-4.23

Table 3-5. Residual stress of the aluminum nitride thin films on Si (100) with change in duty cycle at 75 kHz of frequency (500°C of growth temperature, 28 mT of sputtering pressure, 70% of N<sub>2</sub>, 2 A of target current).

Duty cycle	60% duty cycle	80% duty cycle	96% duty cycle
Residual stress (GPa)	-5.1	-5.3	-5.5

The results are consistent with the atomic peening model [103,104] in which compressive stress is generally attributed to the bombardment of the growing films by energetic atoms originating from the target, either as positive ions neutralized and reflected there or as sputtered negative ions which are accelerated away from the target. Increased scattering of these energetic atoms decreases their energy and thus the compressive stress in the films.

Table 3-6. Photoluminescence peak of the aluminum nitride thin films.

75 kHz, 60% duty cycle		100 kHz, 80% duty cycle	
Wavelength (nm)	FWHM	Wavelength (nm)	FWHM
425 nm (2.99 eV)	75 nm	450 nm (2.82 eV)	88 nm
490 nm (2.59 eV)	116 nm	525 nm (2.42 eV)	93 nm

### 3. 5. Photoluminescence of aluminum nitride

Luminescence phenomena have been used as a tool for the study of defects in materials. The development of optical measurements over last few decades has led to significant advances in understanding both intrinsic and extrinsic (defect) nature of solids. Luminescence experiments have played a prominent role in these advances.

The PL spectrums of the aluminum nitride thin films grown at different frequency/duty cycle are shown in *Figure 3-39*. The AlN films were grown at the condition of 500°C, 28 mT of sputtering pressure, 70% N<sub>2</sub>, 2.0 A of target current. The AlN films had a broad luminescence band in the range of 350 nm and 650 nm and asymmetric shape. By assuming a Gaussian line shape for the luminescence band, the PL spectra can be deconvoluted into several peaks (dotted line). The analyzed photoluminescence peaks of the aluminum nitride films are summarized in Table3-6. The PL peaks for the film grown at 100 kHz/80% duty cycle are located at higher wavelength (lower energy).

Siewiec et al. [105] reported photoluminescence spectrum of nanocrystalline AlN as well as other wide band gap materials grown by plasma assisted CVD method. They found that PL spectrum of AlN differed significantly from those of GaN, BN and C<sub>3</sub>N<sub>4</sub>.

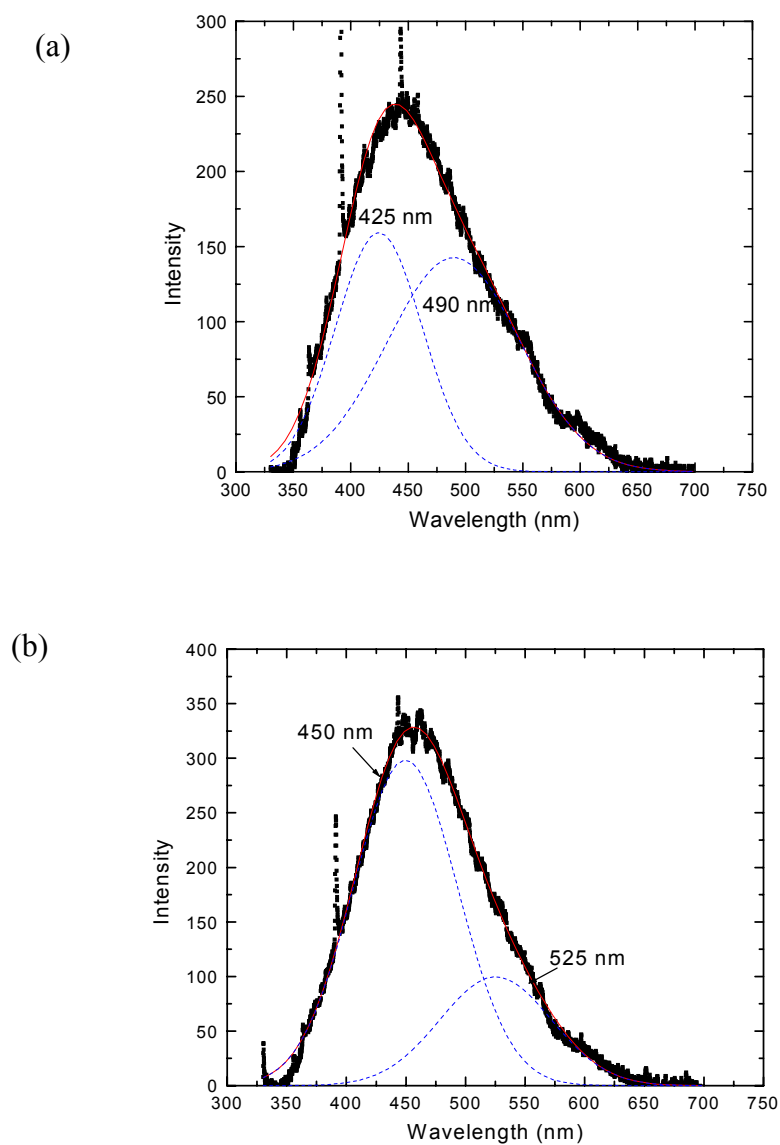


*Figure 3-39.* Photoluminescence spectrums of the aluminum nitride (a) 75 kHz/60% duty cycle and (b) 100 kHz/80% duty cycle (500°C of growth temperature, 28 mT of sputtering pressure, 70% of N<sub>2</sub>, 2 A of target current).

---

Strong emission appeared in the region of 2.25 to 2.75 eV and a weak one was observed at about 3.45 eV UV range. The peak near 2.8 eV is usually attributed to oxygen impurities [106,107]. Sun et al. [108] studied photoluminescence of aluminum nitride films prepared by pulsed laser deposition. They observed broad PL spectrum in the wavelength 300 nm and 600 nm and attributed this to oxygen related defects or nitrogen vacancies. Harris et al. [109-112] investigated the oxygen related defect in an AlN single crystal and polycrystalline ceramics. The AlN ceramics were prepared by sintering at 1850°C with Y<sub>2</sub>O<sub>3</sub> sintering additives. They also found broad PL spectrum in the range 280 nm and 450 nm originated from oxygen related defects.

The peak became broad and the peak center shifted to higher wavelength with increasing oxygen content [109]. The common thing in the reported PL studies is broad spectrum in AlN containing oxygen even though the AlN was prepared by different methods. The PL spectra in the AlN film might be related with oxygen even though the existence of oxygen was not identified by any characterization methods.

### **3.6. Thermal conduction of AlN thin films**

The  $3\omega$  method has been used extensively for measuring the thermal conductivity of thin films and bulk materials [113-7,118,119]. The  $3\omega$  method uses a single metal-line as both the heater and thermometer as shown in *Figure 2-4*. An AC driving current at angular frequency of  $\omega$  heats the surface of the dielectric film at a frequency of  $2\omega$ . Since the resistance of a pure metal increases with temperature, the temperature oscillation also produces another subsequent oscillation of the electrical resistance at the frequency of  $2\omega$ . The magnitude of the temperature oscillation in the line is determined by a compensated balance between the heat generated by Joule heating and the heat lost by thermal conduction into the substrate (and surrounding). The line geometry causes the heat generated by Joule heating to propagate in the form of cylindrical (thermal) waves into the substrate.

Cahill's analysis [113-115] shows that the frequency dependence of the temperature oscillation  $\Delta T$  is inversely proportional to the thermal conductivity  $k$  of the material as shown in the following equation:

$$\Delta T = \frac{P}{k\pi l} \left( \frac{1}{2} \ln \frac{D}{r^2} - 0.2306 - \frac{1}{2} \ln \omega - \frac{i\pi}{4} \right) \quad (3-9)$$

where  $P$  is the amplitude of the heater power per unit length,  $D$  is the thermal diffusivity of the material,  $l$  is the line length,  $r$  is the distance,  $\omega$  is frequency and  $R$  is the line's resistance. The temperature oscillation through the film  $\Delta T_f$  can be obtained from

$$\Delta T_f = \Delta T - \Delta T_{\text{sub}} \quad (3-10)$$

When film thickness  $t$  is smaller than the width of the heater  $w$ , heat flow in the thin film is one-dimensional and the thermal conductivity of the layer can be found using the equation,

$$\Delta T_f = \frac{P}{k} \frac{t}{w} \quad (3-11)$$

*Figure 3-40* shows the temperature oscillation of the heater/thermometer line as a function of frequency for the aluminum nitride thin films on a molybdenum and a silicon substrate. The temperature oscillation  $\Delta T$  is frequency independent as shown in *Figure 3-40*. The thermal conductivities of the aluminum nitride grown at various deposition conditions were obtained from the temperature oscillation as summarized in Table 3-7. The thermal conductivities of the films are in the range of 12 ~ 17 W/m, which are significantly lower than that for bulk AlN. The crystal orientation of films is loose packed structure, (101), (102) and (103) planes. The mean free paths of phonon are calculated from Eq.  $k = \frac{1}{3} C_v v l$  and are in the range 3~4 nm.

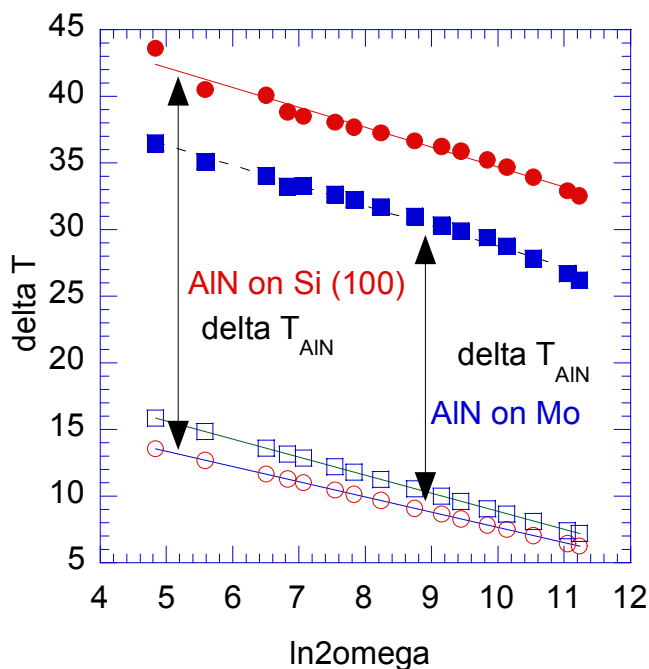


Figure 3-40. Measured amplitude of the temperature oscillation,  $\Delta T$  as a function of frequency of the AlN film grown on Si and Mo (500°C of growth temperature, 75 kHz of frequency, 60% of duty cycle, 28 mT of sputtering pressure, 70% of N<sub>2</sub>, 2 A of target current) thickness of 0.2-1.0 μm).

Kuo et al. [120] reported that the thermal conductivity of aluminum nitride films (0.48~25.2 W/mK) grown by plasma source molecular beam epitaxy (PSMBE). They used thermal mirage method for the thermal diffusivity measurement. They found that more highly textured structures with larger grain sizes present better thermal properties. Jacquot et al. [121] found that temperature dependence of thermal conductivity of the nanocrystalline (5-15 nm range) aluminum nitride films (~310 nm thickness) is similar to

what observed for glass due to the limitations of the mean free path. It may be induced by geometrical effects associated with disordered nature of the structure. Lambropoulos et al [122,123] reported the thermal conductivity of thin films for a large variety of materials (oxides, fluorides, nitrides, amorphous metals and superconductors with The values are as much as two orders of magnitude lower than that of corresponding bulk solid. They attributed this difference to the unique microstructure of thin films, which prevents them from exhibiting bulk-like properties. When deposited with physical deposition methods like sputtering, these films may contain voids, pinholes and nodular defects, reducing the density and integrity of the film. All reduce a phonon mean free path and lower thermal conductivity.

---

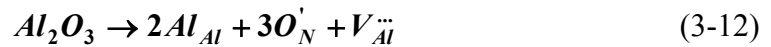
Table 3-7. Thermal conductivity of the aluminum nitride films on Si (100) and Mo measured by  $3\omega$  method.

Deposition condition	k (W/mK)	l (nm)*	Crystal orientation
<u>AlN on Si (t=3.73 <math>\mu\text{m}</math>)</u> 500°C, 28 mT, 70% N <sub>2</sub> , 75 kHz, 60% $\eta$ , 2 A	12.3	3.14	(101)/(102)/(103)
<u>AlN on Mo</u> 500°C, 28 mT, 70% N <sub>2</sub> , 75 kHz, 60% $\eta$ , 2 A	16.6	4.24	(101)/(102)/(103)
<u>AlN on Si (t=1.8 <math>\mu\text{m}</math>)</u> 300°C, 28 mT, 70% N <sub>2</sub> , 100 kHz, 80% $\eta$ , 2 A,	15	3.83	(101)

\*from  $k = \frac{1}{3} C_v v l$  ( $C_v$ =heat capacity 2347 J/m<sup>3</sup>K,  $v$ =phonon velocity 5000 m/sec)

---

In addition to the microstructural features of the film, oxygen in the AlN lattice is known to affect thermal conductivity of AlN strongly. Due to higher affinity of aluminum to the oxygen over nitrogen, oxygen is always in the aluminum nitride. Slack [20,60] proposed that the incorporation of oxygen in AlN occurs by the dissolution of  $Al_2O_3$  by the following reaction:



where  $V_{Al}$  denotes a vacant aluminum site. Above certain oxygen content of 0.75 at.%, complex defect such as inversion domain boundary is formed, resulting in an abrupt decrease in thermal conductivity. The enhancement of the thermal conductivity of AlN can be achieved by adding sintering additives such as CaO and  $Y_2O_3$  [124-126]. These additives remove aluminum vacancies caused by oxygen impurities as shown in Eq. (3-12) as well as pores and defects. Most oxygens are removed from AlN and the residual oxygen impurities are localized at the triple points, resulting in high thermal conductivity. It seems that oxygen contamination is inevitable in sputtering processing. It is reported that about 2 at. % of oxygen was present in the sputtered AlN film even at base pressure of low  $10^{-7}$  Torr [127]. The AlN film grown at 500°C showed very broad PL spectrum (*Figure 3-39 (b)*). As mentioned before, the PL peak width increases and thermal conductivity of AlN decreases as oxygen impurity increases. This might be responsible for the low thermal conductivity of the AlN films.

The distribution of oxygen in AlN is also important for high thermal conductivity. Gorzawski et al. [124] studied the effect of distribution of oxygen on thermal conductivity. They found that the sample having oxygen segregated at the inversion domain boundary has a higher thermal conductivity than that has oxygens located in the AlN lattice even though the former has higher content of oxygen. The distribution of oxygen as well as amount of oxygen seems to be important for achieving high thermal conductivity. About 260 W/mK is the highest known value for bulk AlN [126].

## **4. Unipolar Pulsed DC Sputtering of AlN Thin Films**

### **4.1. Wave Form of Pulsed DC Power**

A unipolar power supply was used to see the effect of different power supply in the aluminum nitride thin film deposition. The power waveform is shown in *Figure 4-1* [128]. The power supply generate waves at 75 kHz modulated at 2.5 kHz. The polarity of voltage doesn't change during the cycle in this case of unipolar power supply. The power to the target was disrupted for the short period of time as shown in *Figure 4-1*. The measured power waveform had an overshoot as shown in *Figure 4-1 (a)*. The circulating power and reflected power are monitored during sputtering deposition. The effective power is delivered to the target for sputtering and circulating power is reflected back to the power supply due to a buildup of insulating material on the target surface. If effective power is greater than circulating power, the deposition mode is in the metal mode of operation in which there is a higher concentration of Al being deposited than AlN. And if effective power is smaller than circulating power, the deposition mode is in a poisoned mode in which AlN is being deposited.

### **4.2. Dependence of sputtering parameters on crystal orientation and microstructures**

#### **4.2.1. Bias effect**

Applying bias to the substrate to attract the ions will be beneficial or un-beneficial to the properties of growing films, depending on the flux and energy of ions. Energetic particles incident on the surface of the growing film transfer energy and momentum to atoms in the lattice of film as they slow down. Although re-sputtering may occur, the major thrust of momentum must be into the coating material. Thus knock-on atoms of the coating material are driven further into the bulk where they tend to fill the microvoids that appear to be an inherent consequence of low  $T/T_m$  deposition. Therefore, there will be enhanced diffusion of adatoms. If the energy of bombarding ions is too high, however, defects will be created in the film. Low energy ion bombardment during

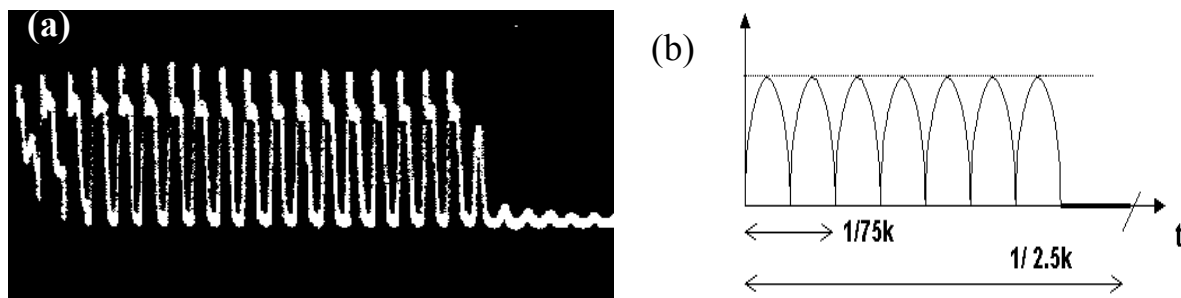
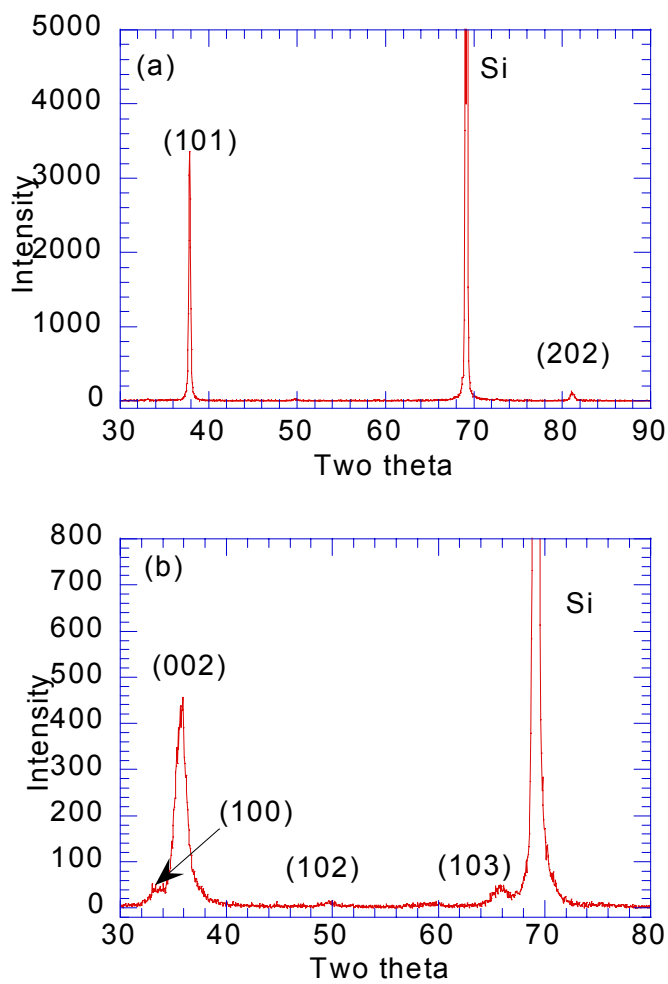


Figure 4-1. (a) Measured unipolar waveform [128] and (b) illustration for the measured waveform.

---

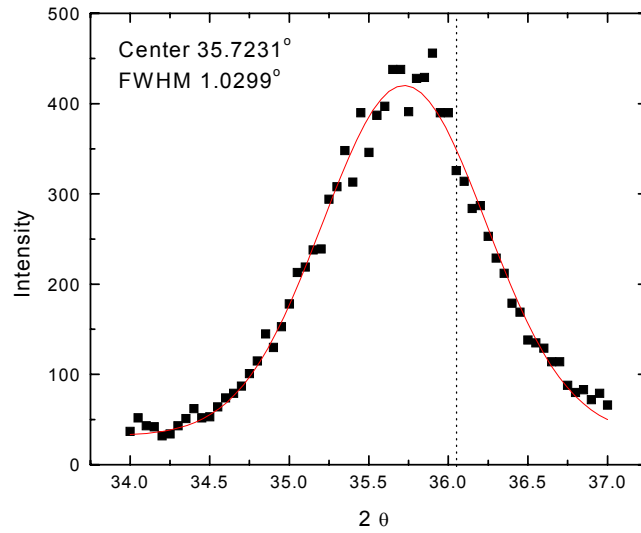
growth can change nucleation characteristics morphology, composition, crystallinity, and composition [129, 130].

Figure 4-2 shows the XRD results of the aluminum nitride thin films on Si (100). It shows the effect of substrate bias. The growth condition was 50 mT of sputtering pressure, 60% of nitrogen content, 2 A of target current and 950°C of growth temperature. Without applying a substrate bias, the aluminum nitride shows the (101) orientation (Figure 4-2 (a)). The orientation was changed to the preferred c-axis orientation by applying a substrate bias as shown in Figure 4-2 (b). By applying bias, the crystal orientation of the aluminum nitride thin film changed to (002) orientation, which is the lowest energy configuration. However, the (002) peak is very broad. The peak broadening comes usually from two reasons. The first one is due to small grain size (particle-size broadening) and the other one is due to stress inside films (strain broadening) [131]. By assuming that the XRD profile of (002) peak follows a Gaussian function, the XRD of the sample prepared with bias was analyzed in the  $2\theta$  range of  $34^\circ$  and  $37^\circ$  range. The result is shown in Figure 4-3. The biaxial stress of the AlN films was estimated from the value of c-lattice constant. The biaxial stress  $\sigma$  is related to the c-axis strain by the modulus of elasticity [132]



*Figure 4-2.* XRD results of the aluminum nitride thin films on Si (100) prepared with (a) without substrate bias and (b) with RF 100 W bias (growth temperature, 950°C, sputtering pressure 50 mT, 60% nitrogen, target current 2 A).

---



*Figure 4-3.* (002) peak of AlN film. The dotted line indicates the (002) peak position of 36.04° for an AlN powder sample. The solid line is Gauss fitting.

---

$$\sigma = [(2C_{13} - (C_{11} + C_{12})(C_{33}/C_{13}))]\varepsilon_z \quad (4-1)$$

where  $C_{ij}$  are the elastic constants for AlN, given as  $C_{11}=396$  GPa,  $C_{12}=137$  GPa,  $C_{13}=108$  GPa and  $C_{33}=373$  GPa. The film strain  $\varepsilon_z$  along the c-axis is given by

$$\varepsilon_z = \frac{c - c_o}{c_o} \quad (4-2)$$

where  $c_0$  is the strain free lattice parameter ( $c_0=4.9938 \text{ \AA}$ ) measured from an AlN powder. Since the tensile c-axis strain is proportional to the compressive biaxial stress, the calculated stress of the film is  $-9.42 \text{ GPa}$ , which is huge compressive stress in the film. Bombardment of the film surface by ions or energetic neutrals can produce compressive stress both by implanting these particles into the film and by momentum transfer to surface atoms as discussed in Chapter 3.

The effect of bias on the microstructures of the aluminum nitride thin films is shown in *Figure 4-4*. The sample grown without bias shows a typical columnar structure (*Figure 4-4 (a)*) while the sample grown with bias shows the very dense structure which was induced by the increased mobility of adatoms by ion bombardment.

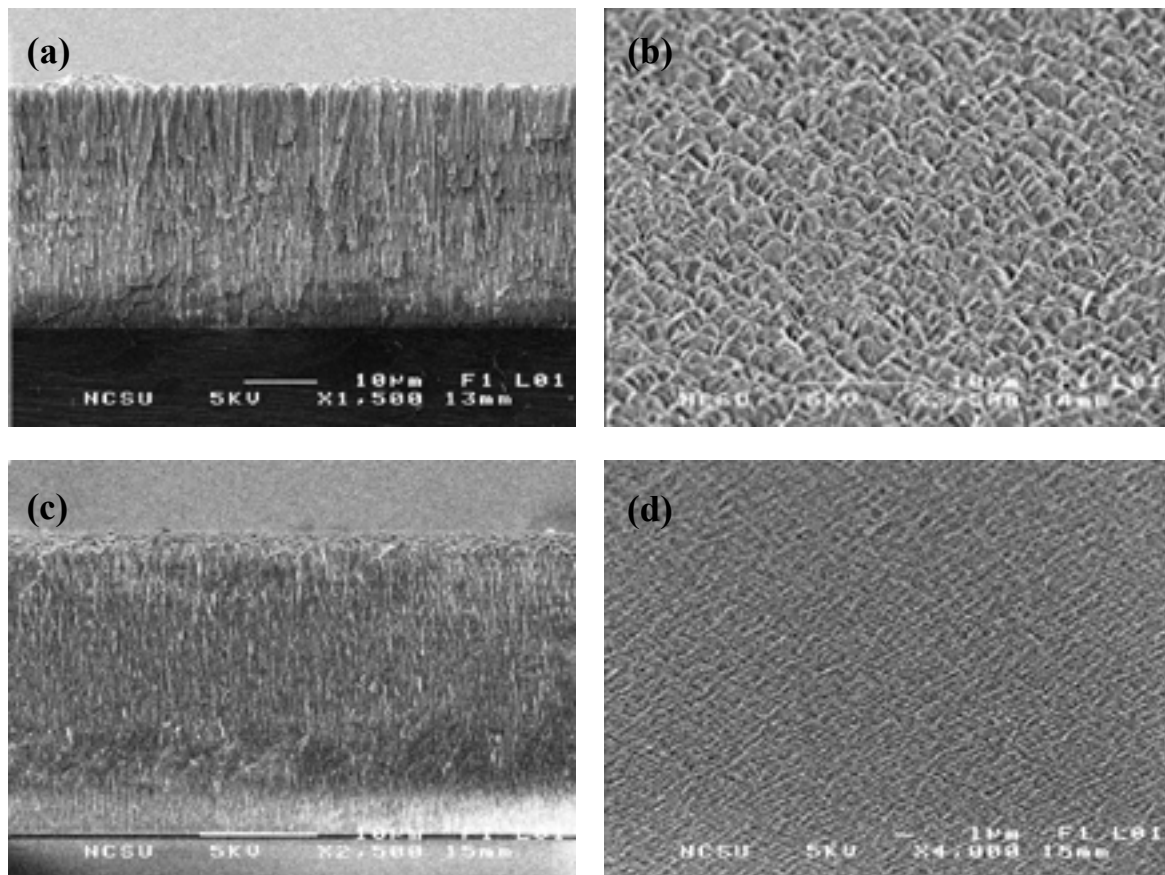


*Figure 4-4.* Microstructures of the aluminum nitride thin films on Si (100) prepared (a) and (b) without bias, (c) and (d) with RF 25 W bias (950°C of growth temperature, 50 mT of sputtering pressure, 60% of nitrogen, 2 A of target current).

---

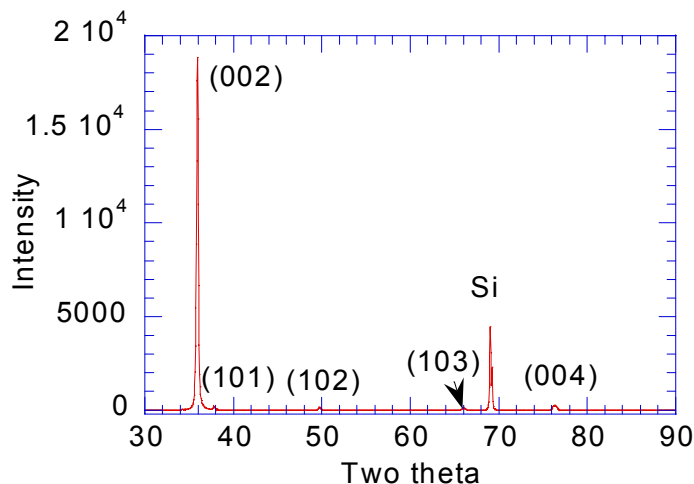


*Figure 4-5.* XRD of the aluminum nitride film on Si (100) (1100°C of growth temperature, 28 mT of sputtering pressure, 60% of N<sub>2</sub>, 25W of RF bias, 2 A of target current).

---

#### 4.2.2. Long deposition processing stability

The long-term deposition stability of insulating materials coating is important in industrial applications. The insulating materials will cover all chamber surfaces and the chamber will be electrically isolated. This is known as "disappearing anode effect" which sometimes lead to arcing on the target surface. The long deposition stability of the aluminum nitride thin films was investigated.

*Figure 4-5* shows the XRD results of the aluminum nitride thin films grown for 20 hrs of deposition time. The deposition condition was 28 mT of sputtering pressure, 60% of nitrogen content, 2 A of target current, 25 W of substrate bias, 1100°C of growth temperature.

---

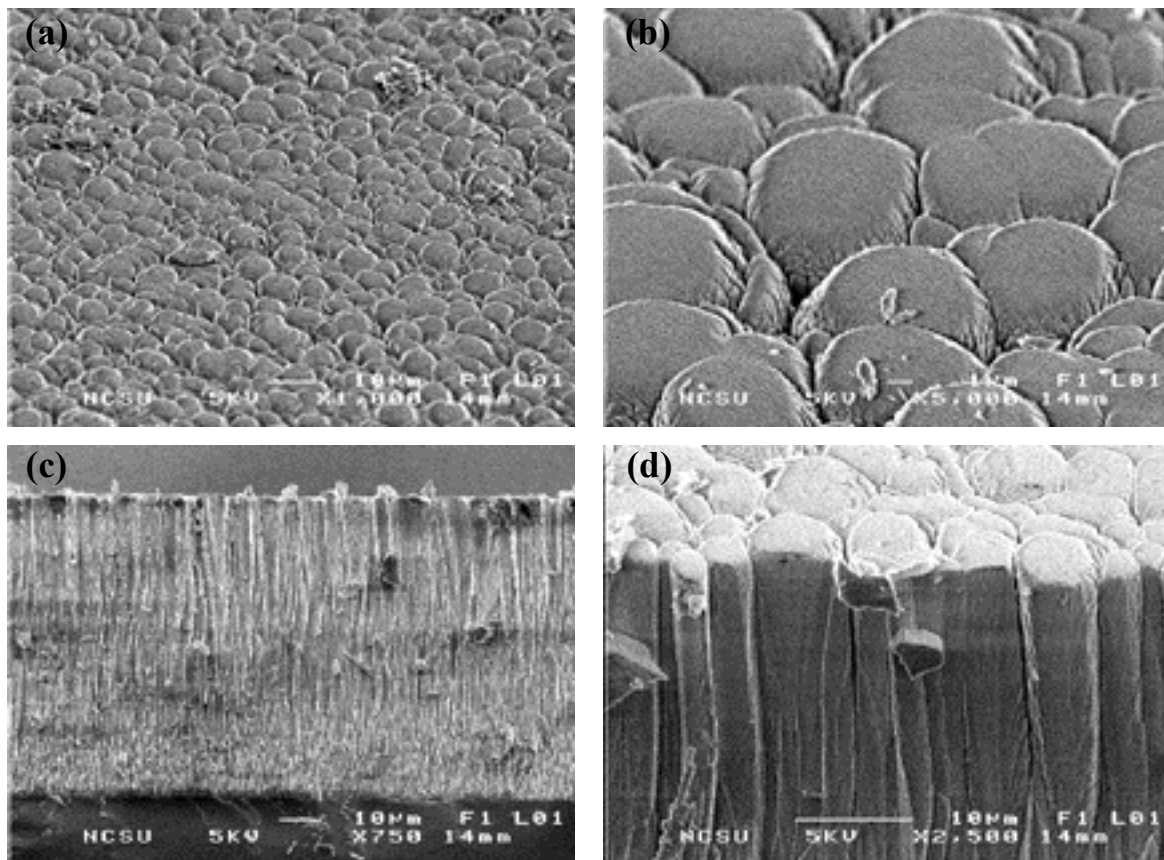


*Figure 4-6.* Microstructures of the aluminum nitride thin films on Si (100) (1100°C of growth temperature, 28 mT of sputtering pressure, 60% of N<sub>2</sub>, 25W of RF bias, 2.0 A of target current).

The real substrate temperature by a pyrometer was about 800°C, which is quite lower than the thermocouple reading. About 3.25 µm/hr of deposition rate (65 µm thickness) was obtained with these deposition conditions. Very strong c-axis orientation with very weak peaks of (101), (102) and (103) was obtained as shown in *Figure 4-5*.

The microstructures of the deposited films are shown in *Figure 4-6*. At initial periods of deposition, the grains were initially very small and then became bigger as the

film grew. This feature is corresponding to Zone T. The surface of film was rough due to the large grains.

#### **4.2.3. Deposition on LTCC (low temperature co-fired ceramics) substrate**

The LTCC substrate has been used in some microelectronic applications requiring low temperature processing [133]. The low temperature processing allows inexpensive conductor materials such as Ag and Cu to be used in the resulting packages. LTCC Tapes are glass-ceramic composite materials. The ceramic filler is usually alumina,  $\text{Al}_2\text{O}_3$  but it could be any other ceramics. The usual composition also includes glass frit to lower processing temperature as well as rendering the material compatible with other thick film components. Typical properties of the Dupont Green Tape<sup>TM</sup> 951 used in this work are summarized in Table 4-1. Most of commercially available LTCC tapes have very low thermal conductivities (about 3 W/mK) due to the large content of refractory ceramics. For high power applications of LTCC tape, however, better thermal management has been needed as discussed in Chapter 1. *Figure 4-7* shows an example of the use of aluminum nitride thin films as a potential heat sink in a multilayer LTCC structure. The surface morphology of a Au conductor screen-printed and fired on the 951 LTCC substrate is shown in *Figure 4-8*. The Au conductor screen printed on the tape was discontinuous and island-like presumably due to the rough surfaces of the 951 Tape as shown in *Figure 4-8* (b). For thick film applications, the rough surface may improve adhesion between contacting layers.

XRD results of the aluminum nitride thin films on the 951 Tape grown at 500°C and 700°C are shown in *Figures 4-9* and 4-10. The deposition conditions were 5 mT of sputtering pressure, 60% of nitrogen content, 2 A of target current. The AlN film grown at low growth temperature and without bias showed multi-orientation (*Figure 4-9* (a)).

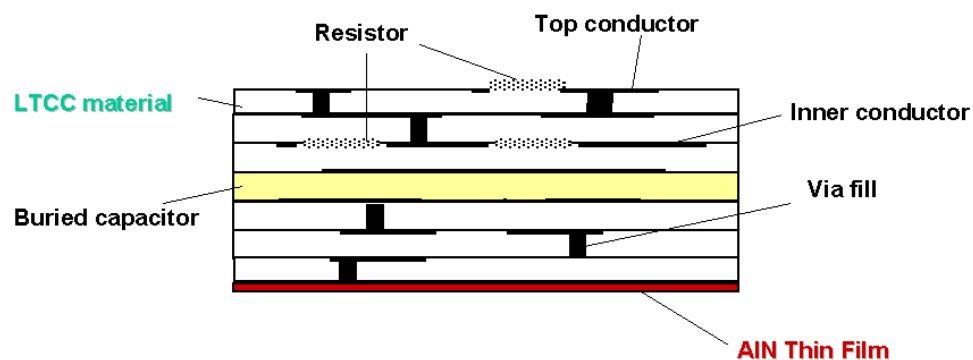
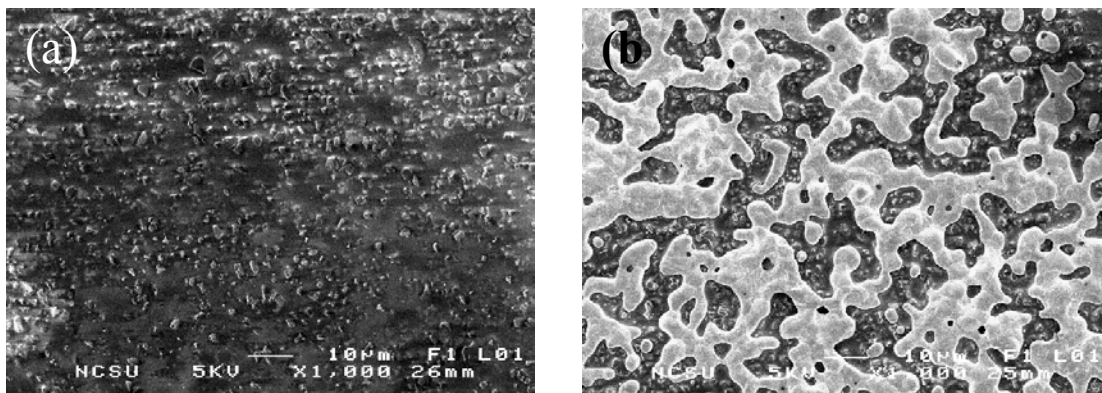


Figure 4-7. An example of aluminum nitride thin film used as a heat sink in multi-layer LTCC structure.

Table 4-1. Typical properties of fired 951 LTCC Green Tape™ (Courtesy of Dupont Co.).

<b>Electrical</b>	
Dielectric constant (@10 MHz)	7.8
Dissipation factor (@10 MHz)	0.15%
Insulation resistance (@100V DC)	$>10^{12} \Omega$
Breakdown voltage (V/25 $\mu$ m)	1000 V
<b>Physical</b>	
Thermal expansion (25°C-300°C)	5.8 ppm/°C
Density	3.1 g/cm <sup>3</sup>
Surface smoothness	0.22 $\mu$ m
Thermal conductivity	3.0 W/mK
Flexural strength	320 MPa



*Figure 4-8.* Surface morphologies of the as-received (a) tape 951 and (b) tape 951 having screen-printed gold.

---

Strong c-axis oriented AlN film was obtained by applying substrate bias as shown in *Figure 4-9* (b). The AlN films grown at 700°C for both conditions had c-axis preferred orientation (*Figure 4-1*). The effect of applying bias to the substrate is more effective. The crystal orientation of the AlN film changed to the (002) orientation which is the lowest energy configuration by applying bias or increasing growth temperature.

*Figure 4-11* shows the surface morphologies of aluminum nitride films on the 951 tape. Aluminum nitride films on the 951 tape and screen-printed gold were quite rough due to the rough surface of 951 tape.

*Figure 4-12* shows the cross-sections of the aluminum nitride films on the 951 tape grown at 500°C with 25W of RF substrate bias. It has a columnar structure which is not continuous. Variations in height of grown AlN films were observed mainly due to the rough surface of 951 tape as shown in *Figure 4-11* (a). Aluminum nitride films on screen-printed gold are shown in *Figure 4-12* (c) and (d).

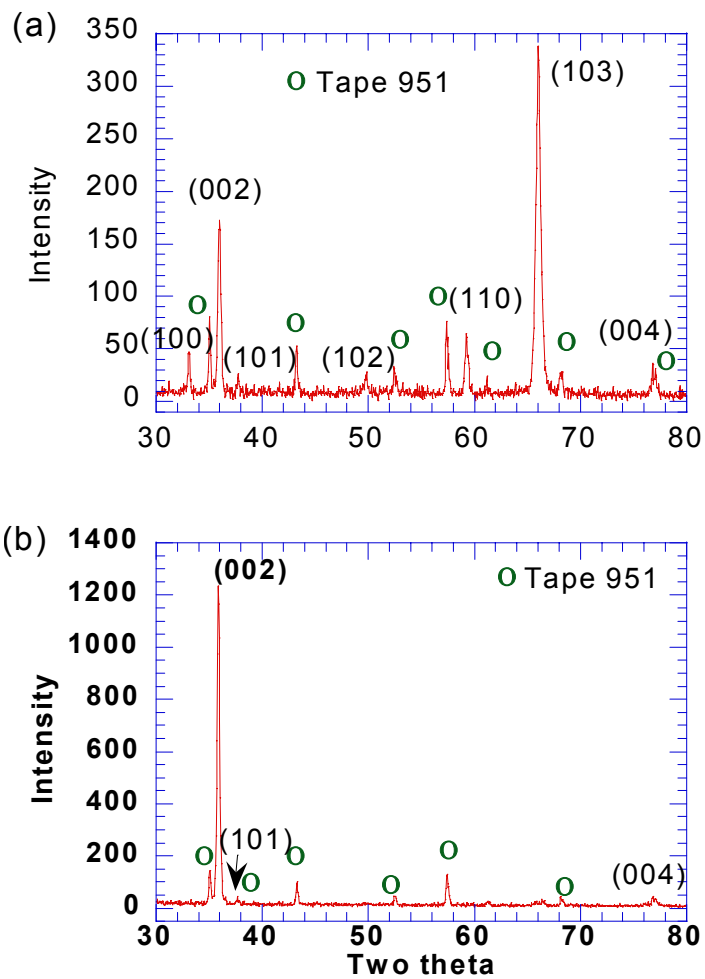


Figure 4-9. XRD results of the aluminum nitride thin films on tape 951 grown at 500°C  
(a) without bias and (b) 25 W RF bias to the substrate.

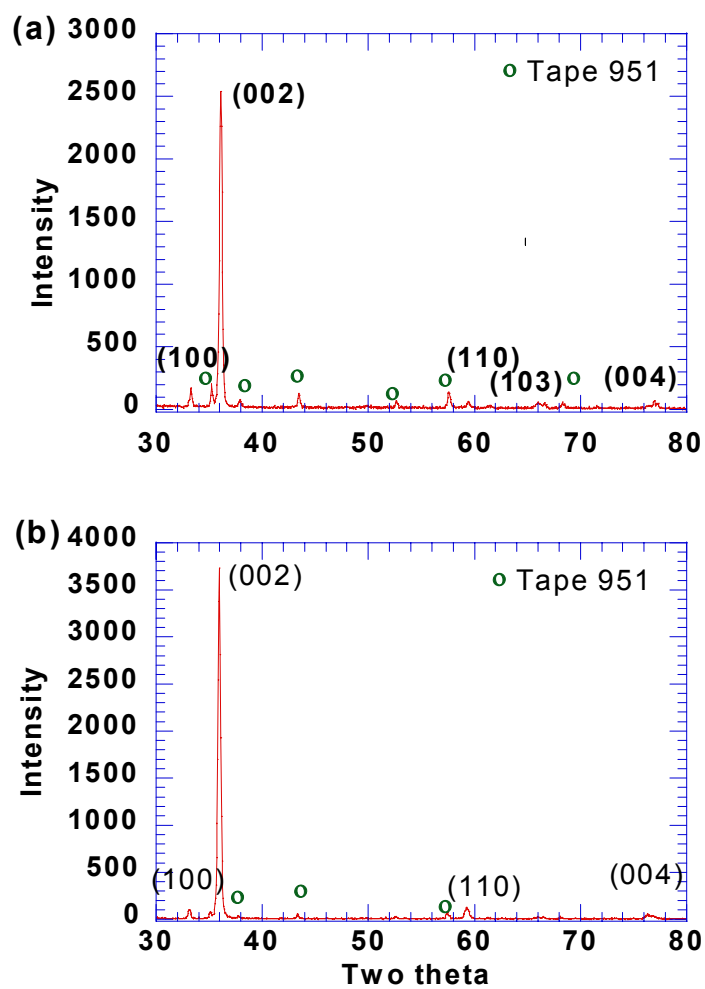
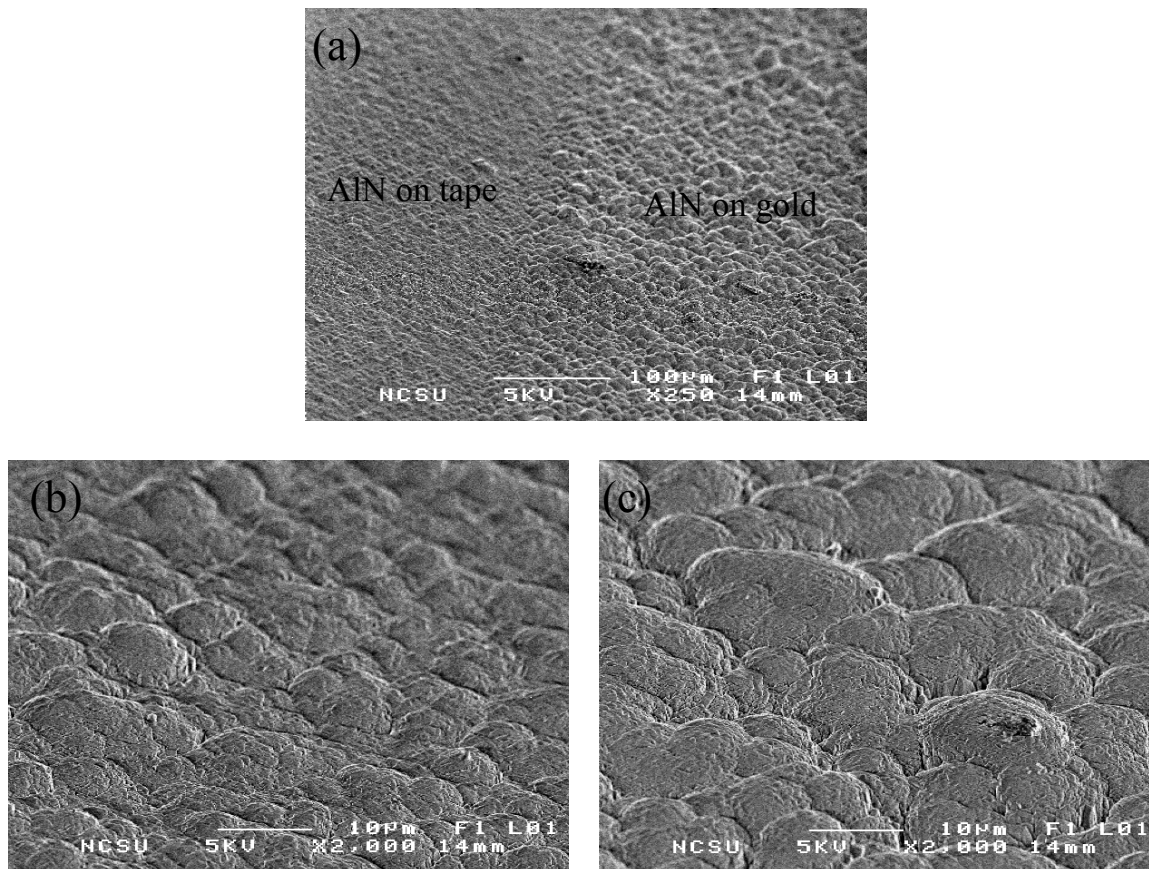


Figure 4-10. XRD results of the aluminum nitride thin films on tape 951 grown at 700°C (a) without bias and (b) 25 W RF bias to the substrate.

---



*Figure 4-11.* Surface morphologies of the (a) AlN films on tape 951, (b) AlN on tape 951 (high magnification) and (c) AlN on screen-printed gold (700°C of growth temperature, without bias, 5 mT of sputtering pressure, 60% of N<sub>2</sub>, 2 A of target current).

---

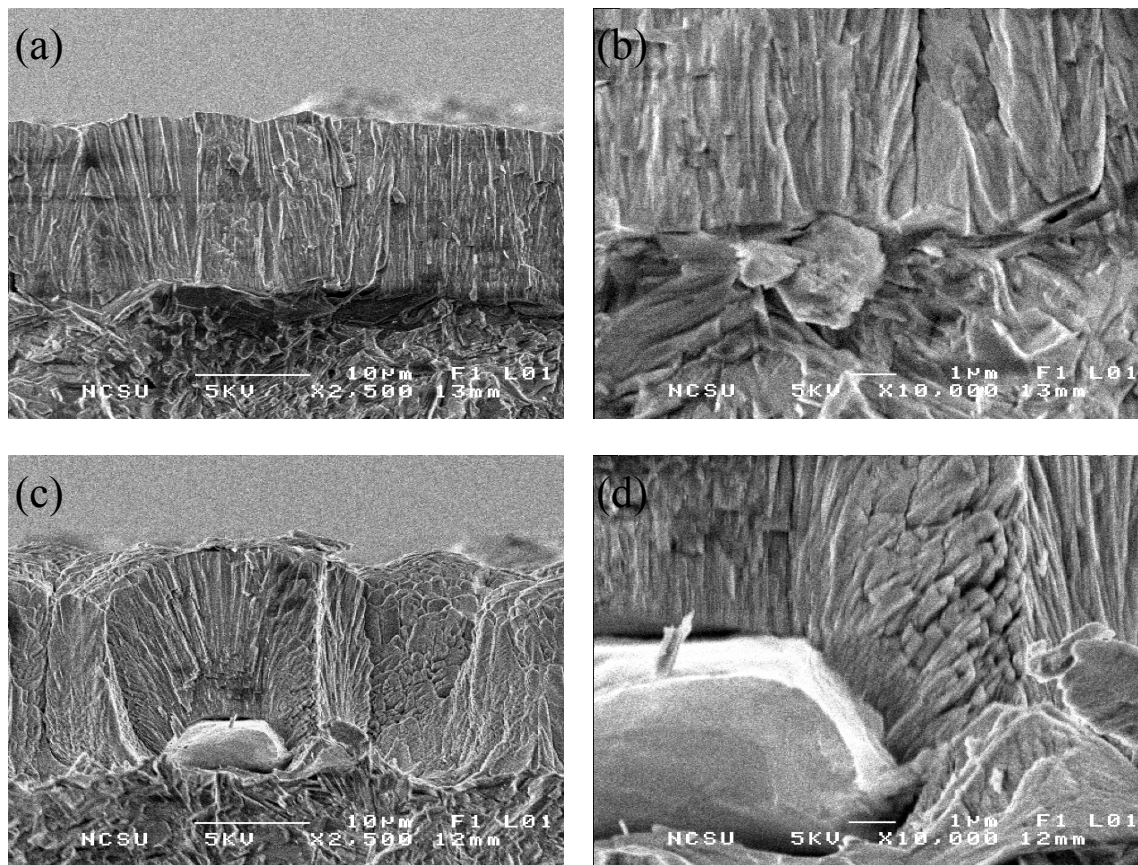


*Figure 4-12.* Cross-sections of the (a) and (b) AlN on tape 951, (c) and (d) AlN on screen-printed gold on tape 951 (500°C of growth temperature, 25 W of RF bias, 5 mT of sputtering pressure, 60% of N<sub>2</sub>, 2 A of target current).

---

Table 4-2. Deposition rates of the sputtered aluminum nitride films.

	Without bias	25W
500°C	4.6 $\mu\text{m/hr}$	3.26 $\mu\text{m/hr}$
700°C	3.01 $\mu\text{m/hr}$	3.18 $\mu\text{m/hr}$

---

White spots correspond to gold conductor fired. It seems that aluminum nitride was nucleated on the gold surface and grew randomly.

Deposition rates for various conditions are in Table 4-2. Deposition rate decreases with bias for both substrate temperatures. The deposition rate at low temperature without bias was maximum. The decreasing deposition rate with bias is also observed by other groups and they explained it as resputtering of adatoms on the substrate by ion bombardment [129,130]. One of the merits of applying bias is improving surface smoothness. However, it couldn't be observed due to very rough surface of 951 Tape.

### 4.3. TEM study

The microstructures of the aluminum nitride thin film deposited on the 951 tape were further observed by transmission electron microscope (TEM). The sample used for the thermal conductivity measurement was used for the TEM observation.

The cross section TEM images are shown in *Figures 4-13~4-15*. *Figure 4-13 (a)* image shows an image taken at the interface of the AlN film and the 951 tape. *Figure 4-13 (b) and (c)* represents TEM photographs of inside and surface of the films, respectively. It clearly shows the columnar structure of the films. As seen in SEM cross-

section photographs, the 951 tape substrate also had very rough surface as evident in the TEM. It seemed that there was no reaction between the AlN and tape 951 as shown in *Figure 4-14*.

The TEM plane view is shown in *Figure 4-15*. The sample was observed at the position close to the film surface. The grains seemed to have irregular shapes and a non-uniform distribution of grain size with some pores as shown in *Figure 4-15 (a)* and *(b)*. The grain boundaries look clean. *Figure 4-15 (c)* shows the voids at the triple point. The sample was relatively dense. The SADP (selected area diffraction pattern) is shown in *Figure 4-15 (d)*. The diffraction is a ring pattern, indicating polycrystalline phase. The ring was not continuous.

One thing observed is that the grain size of the aluminum nitride varies with film thickness. At the beginning, small grains with a uniform distribution formed at the 951 tape. The grains were observed to grow as deposition time increases and thus film thickness increases. The average grain size of the aluminum nitride was obtained by direct observation from the TEM images.

The plot of average grain size versus film thickness is shown in *Figure 4-16*. The average grain size increases parabolically with film thickness. The average grain size of the AlN near the interface is about 11 nm with a small standard deviation.

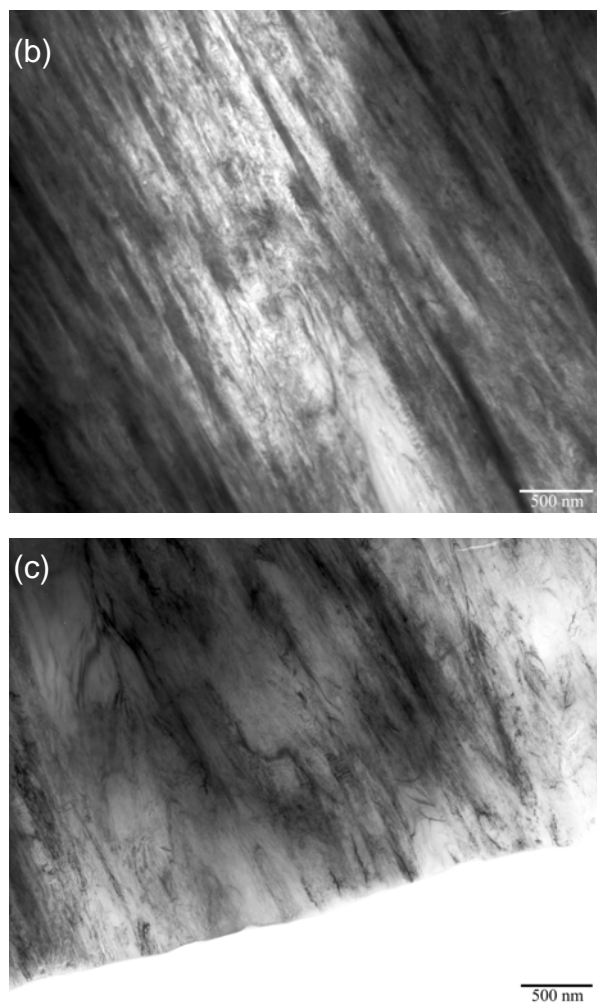


Figure 4-13. Cross section view (a) interface, (b) middle and (c) top of the film on Tape 951.